Electrochemical sensing for food quality and safety

By

Jiang Yang

A dissertation submitted in partial fulfillment of the requirements of the degree of

Doctor of Philosophy

(Biological Systems Engineering)

at the

UNIVERSITY OF WISCONSIN-MADISON

2013

Date of final oral examination: 08/23/2013

The dissertation is approved by the following members of the Final Oral Committee:

Sundaram Gunasekaran, Professor, Biological Systems Engineering

Shaoqin "Sarah" Gong, Associate Professor, Biomedical Engineering/Material Science Program

Xudong Wang, Assistant Professor, Material Science and Engineering

Jae-Hyuk Yu, Professor, Bacteriology

Joel Pedersen, Professor, Soil Science/Environmental Chemistry

Abstract

An electrochemical sensor is a self-contained integrated device capable of generating specific quantitative or semi-quantitative analytical signals based on a biological or chemical recognition element/receptor in combination with an electrochemical transduction element. Electrochemical analytical sensors are used a wide range of industries such as pharmaceutical, healthcare, food, agriculture, environment and water. Food and drink industries are in need for reliable detection technologies to assure product quality, monitor deleterious ingredients and contaminants and process control. Electrochemical sensors afford such promising applications in food processing and quality control owing to their simplicity, rapidity, affordability and miniaturization for on-site detection. Carbon, as an array of atoms in certain structural forms, exists as diamond, graphite, graphene, fullerenes, carbon nanotubes and amorphous carbon (soft, hard, diamond-like or graphitic carbon) with a number of appealing properties for different purposes. This group of materials is being used in the construction of biosensors as transducers, immobilization matrices, stabilizers, and mediators. In this thesis, different carbon or carbon hybrid based electrochemical biosensors are developed for detection of food ingredients and additives such as sugars.

Sugars are not only extensively involved in the production of thousands of food products from cured meat through preserves and frozen fruits to confections, but also directly related to human health such as obesity, glycemic index, metabolism and diseases. The most known health problem is diabetes which is associated with elevated glucose (Glc) level in blood and sometimes in urine and it is yet completely cured as a chronic disease.

Several enzyme-free electrochemical sensors were developed for detection of Glc based on different carbon hybrid nanocomposite materials. Vertically well-aligned multi-walled carbonnanotubes (MWCNTs) were firstly synthesized by chemical vapor deposition (CVD) on a tantalum (Ta) foil substrate using a thin layer of magnetron-sputtered cobalt (Co) as catalyst. The as-synthesized MWCNTs were then modified with copper nanoparticles or cobalt oxide/hydroxide nanoparticles. The modified nanocomposites exhibit much higher electrocatalytic activity towards Glc than before modification, with a high sensitivity, fast response time, wide linear range, low detection limit (at signal/noise ratio=3) and long-term stability for weeks. In another work, a facile one-step approach is used to directly deposit

chitosan-reduced graphene oxide-nickel nanoparticle (CS-ERGO-NiNPs) composites onto a screen-printed carbon electrode (SPE) with outstanding analytical performances. A microfluidic electrochemical device with polydimethylsiloxane(PDMS) chambers and acrylonitrile butadiene styrene (ABS) plastic holders was fabricated to feature the as-synthesized SPE sensor.

Enzymatic electrochemical biosensors were also developed. The first sensor was based on electrochemically-reduced graphene oxide (ERGO) modified with heterogeneous bimetallic gold-palladium (AuPd) nanoparticles, and the as-synthesized material showed extraordinary sensitivity and stability towards oxygen reduction. A biosensor was then constructed by immobilizing glucose oxidase (GOx) as a model enzyme on the nanocomposites for glucose detection through oxygen consumption during the enzymatic reaction and thus this type of sensor is basically suitable for any oxidase-based biosensing. The second enzymatic sensor was fabricated based on platinum nanoparticles (PtNPs)-modified SPE and enzyme-immobilized cellulose paper and the detection was achieved by detection of the hydrogen peroxide (H_2O_2) generated in the enzymatic reaction which is different from the first sensor. The enzyme-modified paper showed better mechanical properties and the paper fluidic device has many advantages in sensing such as reagent storage, sample delivery, concentration and low cost.

Moreover, a disposable indium tin oxide-coated glass (ITO) working electrode was modified by gold nanoparticles (AuNPs)-ERGO for quick detection of lean meat powder compounds in meat samples at low cost for clinical diagnostic and therapeutic purposes as well as to prevent possible illegal use in animal feed. The neurotransmitter dopamine (4-(2-aminoethyl)benzene-1,2-diol) (DA) can be detected using the one-time-use electrode by either amperometry or differential pulse voltammetry (DPV). The electrochemical catalysis of DA was proven to be a surface process and correlates well with the conventional UV-vis spectrophotometric approach but with more than thrice the dynamic range. The sensor also exhibited good stability and capability to detect DA in beef samples, and thus is a promising candidate for simple and inexpensive sub-nanomolar detection of DA, especially in the presence of UV-absorbing compounds.

Lastly, a novel and facile approach was developed to synthesize thin films of magnetite (Fe3O4) with epitaxial needle-like columnar grains on titanium nitride (TiN) buffered substrate using DC magnetron reactive sputtering. The electrocatalytic activity of the epitaxial peroxidase-mimetic Fe_3O_4 thin-film sensor against H_2O_2 reduction was rapid with a response time less than

5 s. The sensor also exhibited an acceptable stability, a satisfactory sensitivity, good selectivity to the substrate, a dynamic working range and a low detection limit. The sensor performance correlated well (R^2= 0.996) with results obtained using a commercial HPLC-UV device. The sensor performance was robust and accurate in measuring H_2O_2 in some complex food matrices. The advantages of relative simplicity and ease of mass production make the epitaxial Fe_3O_4 thin film promising candidate for use in sensing applications.

Acknowledgements

All the work shown here cannot be accomplished without the kind and generous support, guidance, discussion and collaboration from a lot of people. I would like to thank my major supervisor Prof. Sundaram Gunasekaran for his indispensable guidance and extraordinary expertise on my research all through these six years. He also gives me a lot of freedom for brainstorming of innovations and spares no efforts helping me indentify all kinds of accessible resources I need for research. It is very lucky of me to work under his supervision and I'm thankful to such a thoughtful and inspirational advisor. Without his support, I cannot make things possible.

I am also grateful to Prof. Woo-jin Chang and Prof. Rudi Strickler from UW-Milwaukee for sharing their professional knowledge with me in water science, fluidics and mechanical engineering on my research as well as the help for joint grant proposals. Also special thanks to Prof. Weide Zhang at South China University of Technology and Prof. HuangxianJu and Prof. Jianpin Lei at Nanjing University for accepting me as a visiting scholar to work in their labs and I received exceptionally good training and has learned a lot for my research there from them and their students/postdocs. I also want to thank my Ph.D. committee members (listed in the cover page) for providing a lot of help and supervisor for me and answering my questions. Special thanks are also given to Prof. Kyoung-Shin Choi and Dr. Rob McClain in Chemistry at UW-Madison for their outstanding expertise and knowledge to solve my research problems. Thanks are also due to my thesis committee members, Drs. Jaehyuk Yu, Xudong Wang, Joel Pedersen, and Shaoqin Gong for their time and comments and suggestions.

In my department, many thanks to Prof. Troy Runge and Prof. Xueyue Pan for allowing me to use the facilities in their labs and giving me helpful knowledge in bioenergy as experts in the field. I also want to thank Prof. Christopher Choi for helping me on some theory work in one of my manuscript. I want to thank Mr. Bohne Harold and Mr. Bradley A. Brooks for all the help from them all through these years on instrumentations. A big thank you is presented to Ms. Debby Sumwalt for her kind help, patience and encouragement in nearly everything during my stay in Madison.

I also want to thank all my current or past group members for their help, discussions, collaboration and friendship, including Dr. Sritham Eakasit, Dr. Hailin Lin, Dr. SeockWon Lim,

Wantida Homthawornchoo, Dr. Liang Shi, Yi-Cheng Wang, Lin Lu, Zong Liu, Youngsang You and Dr. Rajesh Seenivasan.

My family also plays an essential role in my life and study. My mother and father gave me huge supports and encouragements for my life and since they are medical doctors, they also provide me a lot of help in research. They even got away from their busy schedules to give me a visit here. I will not be who I am and cannot make any achievements without them. My father is such a professional and successful medical doctor with great knowledge and he has been my role model whom I am always learning from. I also want to thank my fiancée, Wenzhao Zhang, for her love and support every day.

Table of Contents

List of Figures

List of Tables

List of Schemes

Chapter 1: Introduction

1.1 Issues in food industries

Food safety and security are significant national and global issues with serious public health and international trade implications. According to a report from Centers for Disease Control and Prevention (CDC), approximately 76 million illnesses, 325,000 hospitalizations, and 5,000 deaths in the United States only each year are related to food-borne illnesses (Mead, Slutsker et al. 1999). In the meantime, the conformity of industrial products regarding maintenance and quality has a profound economical and social impact. Controlling food quality, nutrition and freshness and preventing certain hazardous additives, preservatives, antioxidants and contaminations are of high interest on both manufacturing and customer ends. Thus, reliable and rapid non-destructive methods are urgently needed to prevent any possible spread of dangerous contaminants into our food chain and guarantee product quality. In this regard, simple-to-use, reliable, portable, sensitive, cost-effective and rapid detection techniques are preferable for analytical, nutritional and clinical purposes. Though many biosensors and detection techniques are available to meet the stringent requirements of sensitivity and specificity, they sorely fail in terms of simplicity and short response time needed. Besides, a number of these detection techniques are based on laborious procedures, sample preparations, extremely expensive and lab-use-only devices such as chromatography, electrophoresis, titration, and mass spectrometry. Furthermore, many of the current methods do not work well in identifying target analytes in complex food matrices. As such, food and drink industries need affordable, *in-situ*, simple, sensitive and rapid approaches suitable for complex food matrices to assure product quality and process control. For instance, sugars are not only extensively involved in the production of thousands of food products from cured meat through preserves and frozen fruits to confections as a sweetener and calory-provider, but also directly related to human health such as obesity, glycemic index, metabolisms and diseases such as diabetes. Scarcities of sugar in war time have been proved how important sugar is to a country's food supply chains (Robert H et al. 1955). In food production and processing areas, sugars are also one of the major nutrition ingredients in food to provide human and animals with energy and it is one of the most efficient and economical foodstuff in calories produced per land area.

1.2 Electrochemical biosensors

Sensors are analytical devices that convert a physical, chemical or biological change from its sensing element, into a measurable and processable signal. Schematic parts of biosensors are shown in **Fig. 1.1**, which typically comprise (1) bioreceptors that specifically bind to analytes, (2) electrical interface for recognition events to happen, (3) the transducer element that picks up the signal generated, (4) the amplifier using appropriate reference that converts the transducer signal into electronic signal and amplifies it, (5) processer (e.g., computer) that converts the electronic signal into physically meaningful parameters , (6) displayer that conveys the results to a human operator. The samples to be analyzed can range from human samples to food samples. Specifically, electrochemical biosensors are molecular sensing devices, which intimately couple a biological recognition element (e.g., enzymes, antibodies) to an electrode transducer (Wang 2006). The transducer converts the biological recognition event into a useful electrical signal.

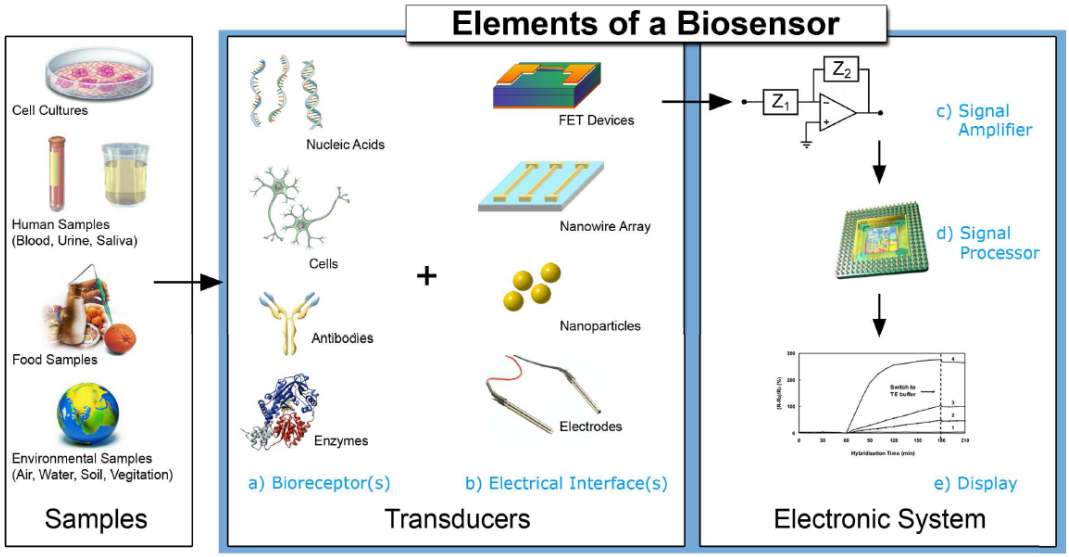

Fig. 1.1: Elements and components of a typical biosensor. Figure adapted from (Grieshaber et al. 2008b).

Electrochemical biosensors can be basically categorized as biocatalytic sensors and affinity sensors (Ronkainen et al. 2010), depending on the recognition process. Biocatalytic sensors incorporate enzymes, whole cells, tissues or electrocatalytic materials (e.g., nanoparticles) that can specifically catalyze reactions with target analytes and generate electro-active species. Affinity sensors such as immunosensors and DNA sensors, on the other hand, are constructed on binding-affinity molecules (antibodies, nucleic acids, membrane receptors and so

on) and their interactions with the target analyte. The bio-recognition units in affinity electrochemical sensing are mostly enzymes, antibodies, nucleic acids, cells, micro-organisms.

In electrochemical immunosensors, antibodies (labeled or unlabeled), antibody fragments or antigens can be all used in fabrication as the receptor to monitor binding events based on the highly specific molecular recognition of immunoreactions. The concentration of antigen(s) of interest is determined mainly in two ways (Liu et al. 2008): 1. Amperometric – by measuring the changes in current responses and 2. Impedance – by monitoring the electronic or interfacial property changes such as impedance and capacitance that are caused by the interaction of analyte and electrode. Due to the reactions to be detected only in close proximity to the electrode/electrolyte interface, the electrodes themselves play the significant role in the performance of the biosensors. Different kinds of electrodes, different types of electrode materials, electrode surface modifications and/or dimensions significantly impact in the detection capability of electrochemical biosensors.

Electrochemical sensing usually involves a reference electrode, a counter or auxiliary electrode and a working or sensing electrode. Reference electrodes (RE) are generally made from Ag/AgCl or saturated calomel electrode (SCE) and are kept at a distance from the reaction site to maintain a known and stable potential. Counter electrodes (CE) are used to establish the connection of electrodes to the electrolytic solution so that a current can be applied to the working electrode. The working electrode (WE) works as the transduction element in the biochemical reaction and thus conducting material like gold, platinum, different kinds of carbon materials, and silicon compounds are often used. All the electrodes are highly conductive and chemically and thermally stable. **Fig. 1.2** below shows the configuration of a typical three-electrode system. In a typical amperometric sensor, with the potential applied between WE and RE, when target toxins are present in the sample solution, a redox reaction occurs either directly or indirectly between WE surface (usually modified and promoted by novel materials) and electrolytes, generating a current. The generated current, the amount of which is related to the amount of antigens present under correct conditions, will flow through the working and counter electrodes, to be detected by the signal processor. In an impedance sensor, however, the change in impedance which is caused by the formation of antigen-antibody immunocomplexes, can block the electron transfers between WE surface and electrolytes (e.g., $Fe(CN)^{-3/-4}$), which lowers the impedance.

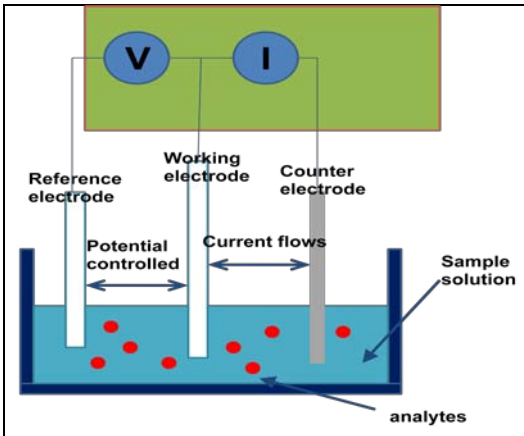

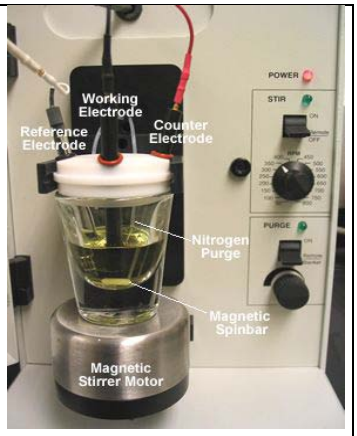

Fig. 1.2: A typical three-electrode system.

Electrochemical sensors have the advantages of high sensitivity, good selectivity, rapidity, ease of use, easy miniaturization (e.g., microelectrodes), low detection limit, need for small sample volume, operating in turbid biofluids with optically absorbing and fluorescing compounds. They can be designed as compact portable units for on-line and in-field uses (Brett 2001) (Grieshaber et al. 2008a) or implantations for *in vivo* uses (Heller 1999). They can be applied to gain real-time information in real matrices (cell cultures, body fluids, food samples, pharmaceutical samples, environmental samples etc.) at temperatures from -30 °C up to 1600 ºC without sampling, depending on the electrolyte used. For a conventional one that works with liquid electrolyte, it can work at up to 140 °C while solid-electrolyte-assisted sensor can withstand up to 500 °C (Guth et al. 2009). Moreover, compared to most other analytical techniques, equipments for electrochemical analysis are simple in their setup and at a low price because of the low-cost production of microelectronic circuits and their easy electronic read-out and processing. It is also possible to develop reusable electrodes for multiple tests, by storing at -4°C in buffers for about two weeks, and by easily regenerating with sorbitol or acidic buffers (Liu et al. 2008). Screen-printed electrodes that combine working, reference and counter electrodes in one set have already been commercially available as reusable and portable electrodes. It is also possible to develop electrochemical sensors for multi-analyte detection spontaneously (Wilson 2005; Wilson and Nie 2006). In addition, as illustrated, electrochemical sensors are not affected by sample constituents such as chromophores, fluorophores and other particles that could disturb spectrophotometric detection. Modern electroanalytical techniques

can achieve very low detection limits of 10^{-7} to 10^{-9} M (<1 ng/mL) (Palchetti and Mascini 2008). Atto- and zeptomole electrochemical immunosensors have been built (Ronkainen et al. 2010). Most electrochemical biosensors have extremely fast responses within seconds and good stability. Electrochemical biosensors also to some degree minimize or eliminate the need of tedious sample pre-treatments, only with liquid samples directly tested or diluted accordingly and with solid samples solubilized or suspended in solutions. Furthermore, it is easy to operate for non-specialists.

1.3 Carbon and carbon nanocomposite materials

Carbon is one of the most abundant elements on earth and is vital in biological and ecosystems. There have been increasing numbers of studies based on carbon-derived materials in application of electrochemical sensors. With some typical structures shown as in **Fig. 1.3**, these carbon-based materials include but not limit to porous carbon (Poh and Pumera 2012; Thangaraj and Kumar 2012), glassy carbon (Ozkan et al. 1998; Thangaraj and Kumar 2012), carbon black (Arduini et al. 2010), boron-doped diamond(Toghill et al. 2010b), fullerene (Jain et al. 2010), graphite (Royo et al. 2013), carbon nanotubes (Jacobs et al. 2010) and graphenes (Pumera et al. 2010). Carbon, as an array of atoms in certain structural forms, is in existence as diamond, graphite, graphene, fullerenes, carbon nanotubes (CNTs) and amorphous carbon (soft, hard, diamond-like or graphitic carbon)(Candelaria et al. 2012) with a number of appealing properties for different purposes. Diamond or diamond-like carbon has sp^3 hybridization with small size, close packing of atoms and shorter and stronger covalent bonding, giving them superior mechanical, optical and thermal properties. Graphitic carbon, however, has sp^2 hybridization, resulting in excellent electrical conductivities. Most popular carbon materials nowadays such as carbon nanotubes, graphene, and fullerenes are all derived from graphite (Candelaria et al. 2012). CNTs have a peculiar seamless structure from the sp^2 carbon units, with hexagonal honeycomb lattices. They have closed topology and tubular structure typically in nano-scaled diameter and micron-scaled length.

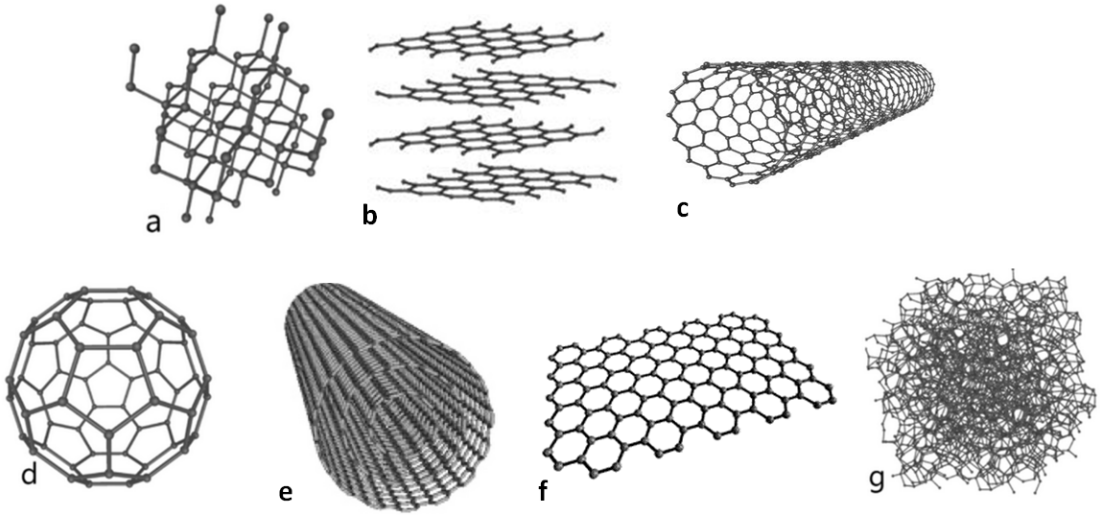

Fig. 1.3: Structures of some common carbon materials (a) diamond, (b) graphite (or few-layered graphene sheets), (c) single-walled carbon nanotube, (d) C60 fullerene, (e) multi-walled carbon nanotube, (f) graphene, (g) amorphous carbon (http://en.wikipedia.org/wiki/Carbon).

Carbon nanotubes (CNTs) are one of the most interesting nanomaterial for sensor applications, due to their unique properties: high electrical conductivity, chemical stability, large surface area, high surface/volume ratio, high mechanical strength, and chemically-modifiable surfaces (Merkoci et al. 2005). These interesting properties are related to their quasi 1D shape and sp^2 and π bonding C atoms. Unlike the π electrons in graphite which can freely move within the hexagonal graphene layer and form electron bands, the electron states in CNTs are restricted by the finite tubular structures and electron transfers happen without scattering. CNTs, different from graphite and carbon fibers, are composed of sp^2 carbon units with seamless structure of hexagonal honey comb lattices. There are two types of CNTs, multi-walled CNTs (MWCNTs) and single-walled CNTs (SWCNTs). MWCNTs are constituted of concentric and closed graphite tubules each of which is made of a rolled graphite sheet respectively with interspacing distances in between. In contrast, SWCNTs are made of a single rolled graphite sheet seamlessly with a tendency to aggregate in parallel to each other if not properly functionalized. CNTs have been electrically used as semiconductors and widely applied in electrochemical sensors to decrease overpotential and improve sensitivity by enhancing electroreactivity and promoting electron transfers. Therefore, CNT-based sensors generally have not only high sensitivities, but also lower detection limits and faster electron-transfer kinetics (Jacobs et al. 2010). Besides, CNT-modified electrodes show better biocompatibility for coating biomolecules and alleviate surface fouling effects (Qureshi et al. 2009). The use of vertically well-aligned CNT array (VACNTs)

electrodes provides extra advantages over random tangles of CNTs electrodes (**Fig. 1.4a**). The 3-D network of CNT arrays can also provide larger surface area and more electroactive sites for spatial diffusion and interaction with target analytes. Each individual CNT can act as a nano-electrode that facilitates the electron transfers without any mediators (Claussen et al. 2009). Further modification of VACNTs with nanoparticles (NPs) can not only increase the effective surface area and electrocatalytic activities but also provide continuous conducting pathways for the transportation of electrons (**Fig. 1.4b**) which is beneficial for application of electrochemical sensors (Zhang et al. 2010b) and have synergistic effect on sensing performances.

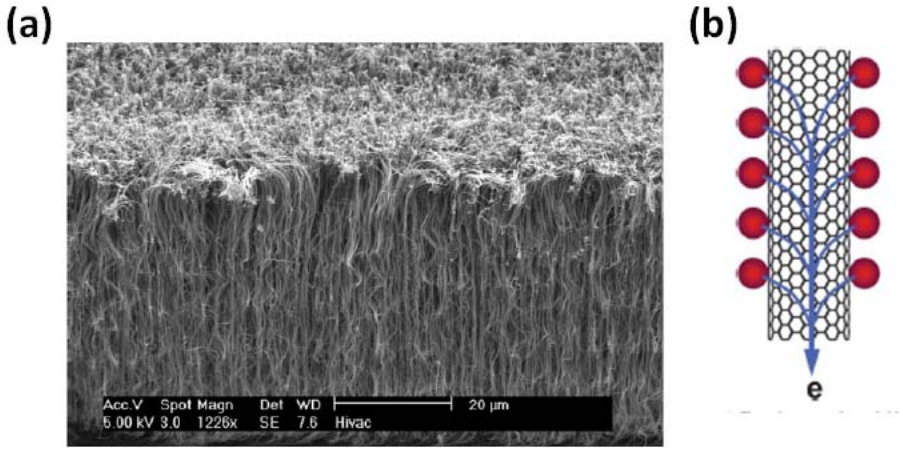

Fig. 1.4: (a) A typical SEM image showing VACNTs morphology. (b) Transportation of electrons within a nanoparticle-modified MWCNT (Zhang et al. 2010b).

Graphene, which has been extensively researched in recent years is a single-atom-thick planar sheet of hexagonally-arrayed sp^2-bonded carbon atoms packed in a 2-D honeycomb crystal lattice (Geim and Novoselov 2007). Despite its relatively short history, many interesting properties of graphene have been revealed such as high surface-to-volume ratio, large surface area, high electrocatalytic activity, fast electron transfers, low cost, robust mechanical properties, flexibility and outstanding conductivity (Stankovich et al. 2006), making it a promising material for applications in electronics/optoelectronics (Muszynski et al. 2008), sensors (Kang et al. 2009; Lu et al. 2011), composites (Stankovich et al. 2006), batteries (Chou et al. 2010) and supercapacitors (Stoller et al. 2008). Its large accessible surface area is favorable for further modifications and biomolecule immobilizations (Choi et al. 2010). Graphene-based sensors were also reported to have higher sensitivities due to the low electronic noise from thermal effects, fast electron transfer kinetics and large surface area for analyte spatial

interactions (Kang et al. 2009). Also owing to its simple chemical synthesis from inexpensive graphite, it serves as both a superior carbon support for growth of NPs and an electrical contact, providing electrode microenvironments as high-performance biosensors and promoting the performance of electrocatalysts. However, as the existence of residual defects in graphene can exert a significant influence on its electronic properties and future applications, efficient reduction of oxygenated species in graphene is on demand to prevent possible unwanted reactions and electrostatic adsorptions. Meanwhile, undesirable excessive reducing agents used in the synthesis of most chemically reduced graphenes would both increase the cost in mass production and could possibly remain and contaminate the synthesized materials. Meanwhile, oxygen-containing functional groups (-OH, C-O-C in the basal plane and –COOH, C=O on the edges) in graphene, though helpful in stabilization in water with high surface free energy, cannot be completely eliminated by chemical reduction and could continue to disrupt the electronic properties (Hernandez et al. 2008). Therefore, it is of great interest to look for a simple and environment-friendly approach for synthesis of graphene sheets for sensing.

1.4 Project description

After a comprehensive review of the current problems in food industries as described in section 1.1, the major challenges are to overcome drawbacks of current detection techniques in terms of cost, simplicity, rapidity and portability and to use a new group of materials to achieve better detection performances for interesting targets in food industries such as sugars, pH, lean meat powder, food allergen and food additives. To solve these issues, my dissertation work focused on the synthesis of materials for sensing either with or without enzymes in a direct or indirect way in complex matrices, specifically as listed below:

(1) Investigating non-enzymatic sensing for Glc using MWCNTs hybrid materials (Chapter 2)

(2) Enzyme-free Glc sensing of with a portable microfluidic device using graphene hybrid materials (Chapter 3)

(3) Enzymatic biosensing based on O_2 reduction with graphene hybrid materials (Chapter 4)

(4) Enzymatic biosensing using paper fluidic devices (Chapter 5)

(5) Electrochemical sensing of lean meat powder ingredients in meat samples with a disposable working electrode (Chapter 6)

(6) Electrochemical detection of H_2O_2 using thin film-based electrodes (Chapter 7)

Chapter 2: Enzyme-free sensing of Glc by MWCNTs hybrid materials*

2.1 Introduction

The pursuit of a rapid, simple, inexpensive and reliable Glc sensing is on-going for various applications including clinical application of blood Glc sensing (Milardovic et al. 1997), ecological application of industrial water-waste treatment (Goto et al. 2004) and food application of dietary and obesity control (Grossman 1986). For example, 300 million diabetic patients worldwide have to regularly measure their blood Glc level (King et al. 1998). Since the first introduction of glucose enzyme electrodes in 1962 by Clark and Lyons (Clark L. C. 1962; Clark L. 1962), many investigators developed sensors based on GOx which oxidizes glucose into gluconic acid in the presence of oxygen by direct electron transfers (Clark L. C. 1962; Deng et al. 2008; Garjonyte and Malinauskas 1999; Kong et al. 2009; Lim et al. 2005; Umar et al. 2009; Zhao and Ju 2006). A number of other Glc sensors based on GOx have been developed based on optical colorimetric detection (Wang et al. 2009), fluorescence detection (McCartney et al. 2001), and electrochemical chemiluminescence detection (Delaney et al. 2011). However, due to the intrinsic properties of enzymes, the catalytic activity of GOx is vulnerable to environmental conditions such as temperature, pH, humidity, ionic detergents and toxic chemicals (Wilson and Turner 1992). Furthermore, GOx sensors pose other problems such as high cost, need for oxygen, instability, critical operational conditions, and need for complicated immobilization procedures usually associated with adsorption, cross-linking and entrapment in an electropolymerized and biocompatible matrix (Yang et al. 2006a; Yang et al. 2006b). Therefore, simpler direct enzyme-free Glc sensing is highly desirable (Park et al. 2006). Much work has been done to develop enzyme-free Glc sensors using metals such as Cu (Kang et al. 2007), Pt (Joo et al. 2007; Yuan et al. 2005) and Au (Jena and Raj 2006; Kurniawan et al. 2006; Zhou et al. 2009); metal alloys such as Au-Cu (Tominaga et al. 2008b), Au-Ag (Tominaga et al. 2008a) and Pt-Pb (Wang et al. 2008b); and metal oxides such as CuO (Batchelor-McAuley et al. 2008a; Zhuang et al. 2008), MnO2 (Chen et al. 2008), and CoOx (Buratti et al. 2008). Most of these sensors undergo surface etching during electrochemical processes or surface poisoning by intermediate species and chloride ions (Ye et al. 2004b), and thus suffer from low sensitivity, narrow linear range, high cost of rare metal precursors, and poor specificity to Glc. Therefore, there is still a need for an inexpensive, highly sensitive, stable, and specific enzyme-free electrocatalysts for Glc.

*This work has been published: (Yang et al. 2011e; Yang et al. 2010b)

Copper is one of the widely investigated metal catalysts and its electrodeposition has been studied on various carbon scaffolds (Ghodbane et al. 2007). It is generally agreed that the unique structural, physical and chemical properties of nanoscaled materials are closely related to both the size and the shape (Zhang et al. 2008b). Thus, controlling the nanomaterial morphology has become an effective way to acquire certain unique properties. With the shape-controlled synthesis of nanoscale materials is concerned, various techniques including water-in-oil microemulsion (Chen et al. 2007), sol-gel technique (Yu et al. 2005), electrochemical technique (Huang et al. 2006), autoclave (Zhu et al. 2004) and microwave (Tao et al. 2008), have been used to obtain cubes (Chen et al. 2007), flowers (Yu et al. 2008), wires (Zhuang et al. 2008), platelets (Wang et al. 2008a), spindles (Zhang et al. 2008b), rods (Ren et al. 2009) and prisms (Pal et al. 2009). For example, Zhang et al. synthesized CuO nanostructures of wires, platelets and spindles and applied them for Glc sensing by a simple wet-chemical method (Zhang et al. 2008b) and Kang et al. electrochemically deposited Cu nanoclusters onto a MWCNTs-modified glassy carbon (GC) electrode (Kang et al. 2007). Since the properties of materials strongly depend on their shapes and dimensions, it is of great value to find a simple and effective way to synthesize nanostructures.

Herein, we present a novel nanocomposite of Cu nanocubes and MWCNTs. MWCNTs were grown on a Ta substrate by a catalytic vapor deposition technique (Zhang et al. 2002) and Cu nanocubes were electrochemically deposited onto MWCNTs by the potentiostat technique. The MWCNTs array was presumed to play an important role in the formation of Cu nanocubes due to their large surface area, availability of many active sites, high surface energy, and fast electron transfer ability. The resulting Cu-modified MWCNTs electrode shows considerably higher electrocatalytic activity for Glc than either unmodified MWCNTs or Cu-modified GC electrodes. This new nanocomposite material combines both the advantages of Cu nanocubes and MWCNTs (Katz and Willner 2004), and a synergistic effect. Thus the Cu-MWCNTs nanocomposite electrode shows high sensitivity, good specificity, fast response, low detection limit, excellent stability, and wide linear range for the detection of Glc, making it a promising candidate for the development of enzyme-free amperometric Glc sensors.

Cobalt ion-based materials have received much attention because of their stability in alkaline conditions, electrocatalytic activity, and interchange ability between various valence states. Various methods have been proposed to prepare $CoOx \cdot nH_2O$, including sputtering

(Schumacher et al. 1990), sol-gel (Jayatissa et al. 2007), hydrothermal (Liu et al. 2009a), and electrodeposition from different precursor solutions containing complex agents (Casella 2002; Casella and Gatta 2002). Of these, electrodeposition method is less elaborate, more controllable, simpler, and cheaper. The morphology and composition of $CoOx{\cdot}nH_2O$ strictly depend on solution composition, temperature, applied potential, deposition time, and electrode substrate (Casella and Gatta 2002). Although the electrochemical behaviors and electrocatalytic activities of $CoOx{\cdot}nH_2O$ has been widely studied, there has not been a systemic report on non-enzymatic Glc sensor based on it. Here, $CoOx{\cdot}nH_2O$ nanostructures were homogeneously coated onto the nanotube arrays using a proton-consuming H_2O_2 reduction mechanism in a $CoCl_2$ precursor solution under a low cathodic potential of -0.10 V. The resulting nanocomposite was characterized by scanning electron microscopy (SEM), transmission electron microscopy (TEM), energy dispersive X-ray spectroscopy (EDS), and electrochemical impedance spectroscopy (EIS). The electrocatalytic activity of the nanocomposite, estimated by both voltammetric and amperometric methods, show a high sensitivity against Glc.

2.2 Experimental

2.2.1 Materials and chemicals

D(+)-glucose, L-ascorbic acid (AA), uric acid (UA), dopamine (DA), D-fructose, mannose, and lactose were purchased from Alfa Aesar. All other reagents were of analytical grade and were used as received. High quality deionized (DI) water (resistivity >18.4 MΩ $\cdot cm^{-1}$) was used in all experiments.

2.2.2 Instrumentation

X-ray diffraction (XRD) profiles of Cu-modified MWCNTs were obtained from an x-ray diffractometer (XD-3A, Shimadzu) with high-intensity Cu Kα radiation (λ=1.5406 nm), at a scanning rate of 4° min^{-1} and 2θ ranging from 20° to 100°. The morphologies and nanostructures of the vertically-aligned MWCNTs and Cu nanotubes were determined using high-comparison and high-resolution transmission electron microscopy (HCTEM and HRTEM) on a Hitachi H7650 (Tokyo, Japan). Scanning electron microscopy (SEM) was performed on a Hitachi S-3700N (Tokyo, Japan), which was equipped with an energy dispersive X-ray spectrometer (EDS) to analyze surface elemental compositions.

All electrochemical measurements were performed on a CHI 660C electrochemical analyzer (Shanghai Chenhua, China) using the conventional three-electrode configuration including a Ag/AgCl (3 M KCl) reference electrode, Pt wire counter electrode and a working electrode (unmodified or Cu-modified MWCNTs). All potentials were referenced to Ag/AgCl (3 M KCl) electrode.

2.2.3 Synthesis of vertically aligned MWCNTs

The synthesis of vertically well-aligned MWCNTs has been described in detail on different substrates of quartz and silicon by chemical vapor deposition (De Zhang et al. 2002; Zhang et al. 2002). Same procedures were followed using 3-mm x 3-mm Ta foil as substrate. Ta is chemically inert, mechanically hard, highly conductive, and relatively inexpensive, with a high melting point enabling it to endure a high temperature required for growing MWCNTs. Briefly, a thin layer (8 to 50 nm) of Co, coated by magnetron sputtering under a vacuum better than 10^{-6} Torr onto the ultrasonically cleaned Ta plates, was used as catalyst. The thickness of the Co layer, controlled by the sputtering power and growth time, determines the dimensions of MWCNTs (De Zhang et al. 2002). Under a steady flow of N_2 at a rate of 500 sccm, Ta plates were put in a pre-heated tube reactor and ethylenediamine (EDA) precursor was introduced by bubbling N_2 through ethylenediamine liquid. The feeding gas contains a final concentration of ethylenediamine of about 8% and the growth of carbon nanotubes was conducted at 800-900°C for 5-30min before being cooled down to room temperature under ambient N_2. A black layer of MWCNTs was formed only within the area of the Ta plates defined by the patterned cobalt catalyst. A schematic diagram of controlled MWCNTs array CVD growth is shown as in **Fig. 2.1** and a typical controlled synthesis is shown as **Fig. 2.2**.

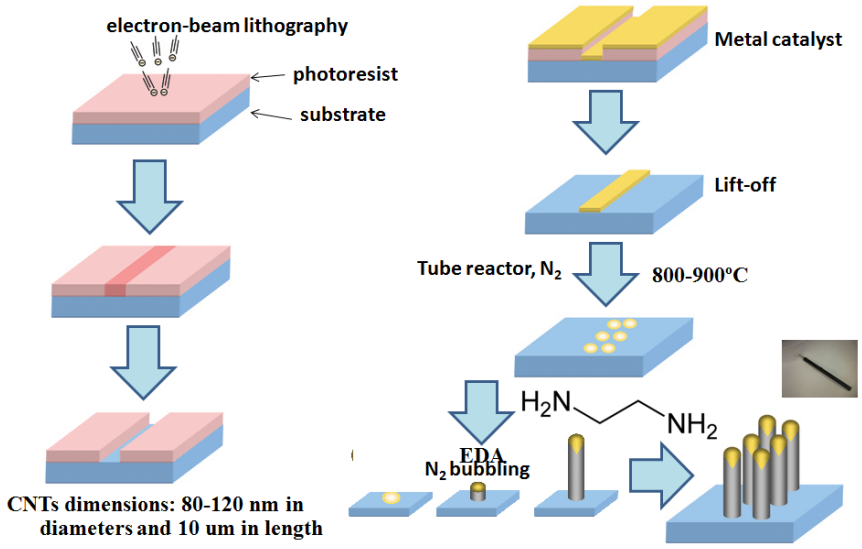

Fig. 2.1: A schematic diagram of controlled MWCNTs array CVD growth using EDA precursors and cobalt catalyst on Ta substrate.

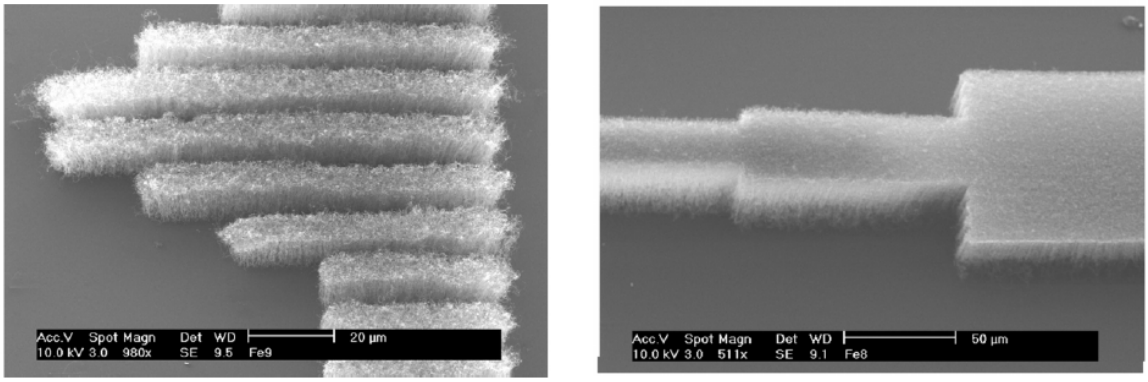

Fig. 2.2: A typical controlled growth of vertically-aligned MWCNTs arrays(Zhang et al. 2002).

2.2.4.1 Synthesis of Cu nanoparticles onto MWCNTs

Vertically well-aligned MWCNTs arrays were synthesized employing the catalytic chemical vapor deposition technique on Ta foils (3 mm x 3 mm in area) (De Zhang et al. 2002; Zhang et al. 2002). The resulting MWCNTs on the Ta substrate were used as MWCNTs array electrode by connecting it to the surface of a GC electrode with a conductive silver paint (Structure Probe Inc., USA). Nail enamel (Maybelline, USA) was used to insulate edges of the electrode for further electrodeposition of Cu nanocubes. The copper nanocubes were electrochemically coated onto the MWCNTs array by potentiostatic deposition. A precursor solution of 10 mM $CuCl_2$ and 100 mM KCl was used as the copper source. A constant potential of -0.40 V was applied to the MWCNTs electrode for 120 s, which was previously determined to be the optimized time. All

experiments were done at room temperature (25±1 °C) and solutions were pre-purged with N_2 for at least 15 min to remove O_2, while a continuous flow of N_2 was maintained during experiments. A GC electrode was also used for electrochemical deposition of Cu under the same conditions to investigate and compare its catalytic activity with that of Cu-MWCNTs.

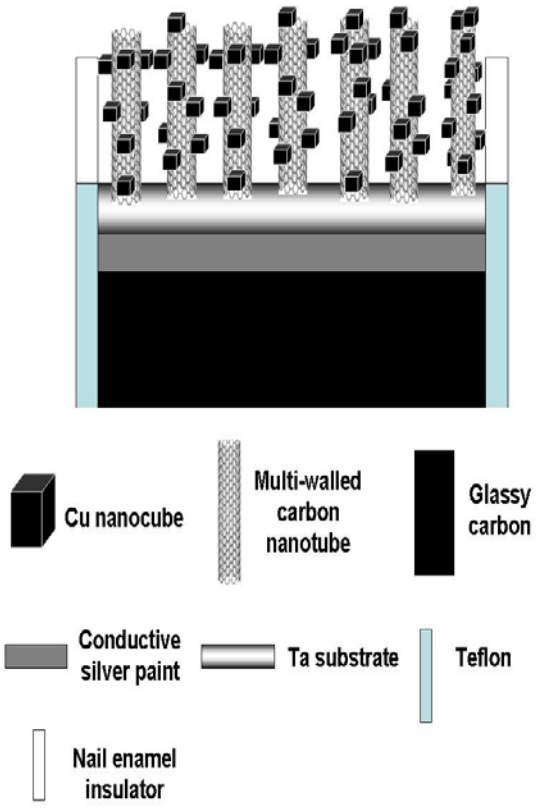

Fig. 2.3: Configuration of the Cu-nanocube modified MWCNTs array electrode (and $CoOx{\cdot}nH_2O$-MWCNTs electrode is in a similar configuration)

2.2.4.2 Synthesis of $CoOx{\cdot}nH_2O$ structures onto MWCNTs by an H_2O_2-assisted reduction

$CoOx{\cdot}nH_2O$ structures were synthesized on MWCNTs using an H_2O_2-assisted approach. The general approach of deposition of metal oxide/hydroxide nanostructures by H_2O_2 reduction had been reported (Yan et al. 2008). In brief, a constant potential of -0.10 V was applied to the as-prepared MWCNTs electrode for 1 h in a precursor solution. This solution was composed of 100 mM KCl, 10 mM $CoCl_2$ and 10 mM H_2O_2, which had been pre-purged with N_2 for 15 min. After cathodic polarization for 1 h in the precursor solution, $CoOx{\cdot}nH_2O$-modified MWCNTs were rinsed with DI water and air-dried.

2.3 Results and discussion

2.3.1 Characterizations

2.3.1.1 Cu-MWCNTs electrode

A typical XRD profile of as-prepared Cu-MWCNTs is shown in **Fig. 2.4A**. The peaks labeled with stars indicate reflections from Ta substrate (JCPDS 04-788) and those with pound signs at 2θ of around 43° and 95° were very close to the profiles of metallic Cu (JCPDS 04-0836). No additional peaks of Cu or of other impurities or oxidation of Cu_2O or CuO were seen. The obvious peak observed at 2θ=22.4° was attributed to graphite carbon C(002) (JCPDS 75-1261). Elemental compositions of Cu-MWCNTs were analyzed by EDS (**Fig. 2.4B**). Ta, O and Co elements were observed for unmodified MWCNTs arrays. The peak of Ta was from the substrate and the small amount of Co originated from the catalyst used during MWCNTs synthesis (Chen et al., 2008). In comparison, Cu was only observed in the spectrum of Cu-MWCNTs, suggesting Cu was successfully electrodeposited onto the MWCNTs. **Fig.2.4C** shows the TEM images of MWCNTs and Cu-MWCNTs nanocomposite. Before modification (**Fig.2.4C inset**), the nanotubes were smooth, with the tubular diameter of 110.8±5.5 nm (six measurements), consistent with the range of 80 to 120 nm reported in the literature (Ye et al. 2003). After electrodeposition, the tip and sidewalls of MWCNTs were embellished with solid Cu nanocubes, giving them a high aspect ratio and large surface area. The Cu deposits are clearly in a cubic-like morphology with fairly uniform edge dimensions from 20 to 70 nm. There are larger and more nanocubes present at the MWCNTs tip than at other locations, owing to the high static attraction at the tip during electrodeposition. The morphology and structure of MWCNTs and Cu-MWCNTs were further investigated with SEM. The nanotubes were found to be vertically well-aligned with part of the nanotubes peeled off for easy observation (**Fig.2.4D**). The surface of the unmodified MWCNTs is rather clean and smooth (**Fig.2.4D inset**), whereas that of Cu-MWCNTs becomes rough with Cu particles of cubic-like morphology attached to sidewalls and tips (**Fig.2.4E**). The majority of Cu particles have a uniform cubic structure. **Fig.2.4E Inset** once again confirms the attachment of Cu particles to MWCNT and the cubical nanostructure of the deposited metallic Cu.

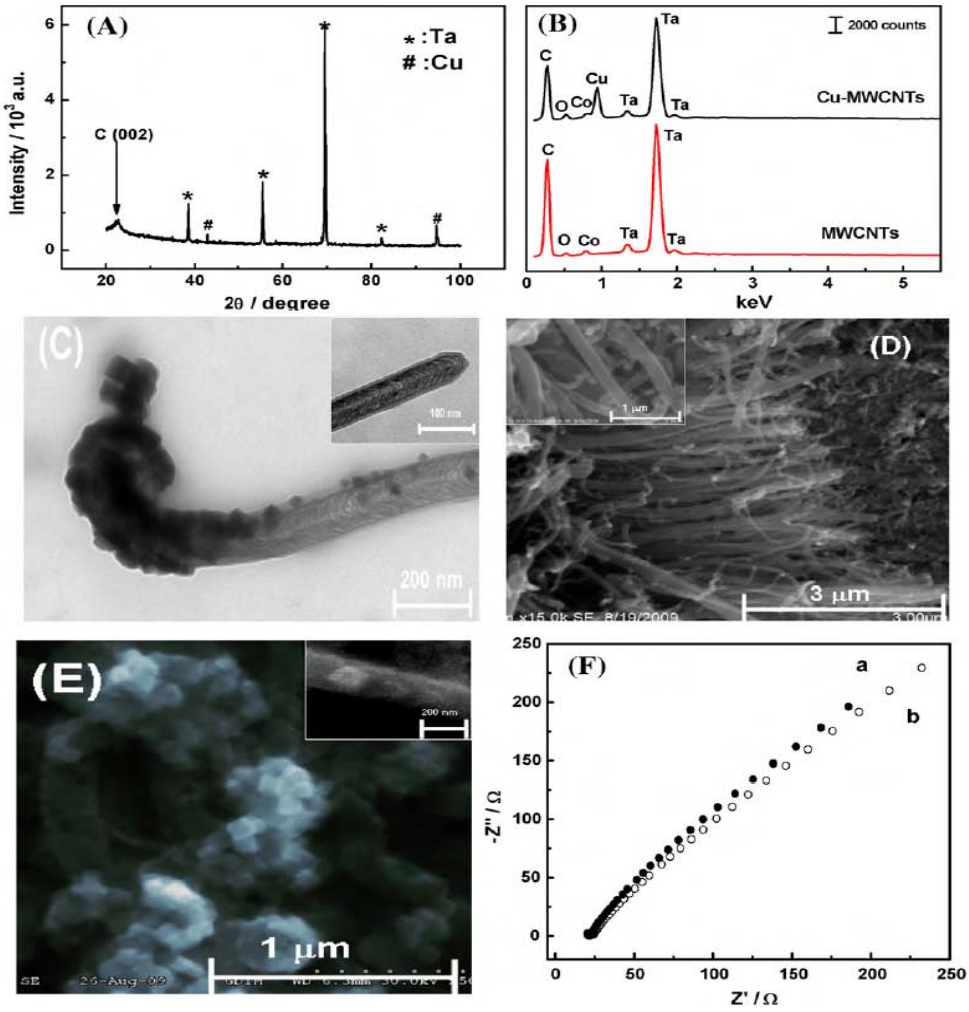

Fig. 2.4: (A) XRD pattern of Cu-MWCNTs on a Ta substrate. #: reflections from Cu; *: reflections of Ta. (B) EDS spectra of Cu-MWCNTs and MWCNTs. (C) TEM images of Cu-MWCNTs and MWCNTs (inset). (D) SEM images of MWCNTs array at low magnification and its unmodified smooth at higher magnification (inset). (E) SEM images of Cu-MWCNTs at low magnification and a Cu nanocube on the sidewall of MWCNTs at higher magnification (inset) (F) Electrochemical impedance spectroscopy (EIS) of Cu-MWCNTs (a) and MWCNTs (b) in 0.1M KCl electrolyte solution containing equimolar (0.01 M/0.01M) $[Fe(CN)_6]^{4-/3-}$. Applied ac frequency range: 0.1 Hz to 100 kHz.

Though the detailed mechanism of electrochemically forming the Cu nanocubes is not clear yet, anion species present in the solution and the MWCNTs arrays are believed to play an important role. Anions are generally known to absorb onto a crystal surface and can affect the growth rates between facets of nanoparticles (Yamada, 2009). It has been reported the additive effect of a salt can achieve cubic selectivity of up to 84% (Yamada et al., 2005). In our system, chloride ions present in the copper plating solution can form aqueous Cu(I)-chloride ion complexes and induce strong chloride ion-copper surface adsorption interactions to affect the kinetics of copper electrodeposition (Chassaing and Wiart, 1984). In the nucleation process

under a low cathodic overpotential, Cu surface is covered by chloride-containing anion species (Magnusen, 2002) and can therefore hinder the electrodeposition. The anisotropy of copper electrodeposits can be ascribed to the copper-chloride ion complexes interacting with different copper surface lattice sites (Yamada, 2009) and can become rate- and morphology-determining (Wu and Barkey, 2000). Furthermore, the interaction of Cl^- and Cu nuclei surfaces might also be involved, which could reduce the growth rates and generate a highly anisotropic growth for Cu nanocubes, similar to the 'poisoning' mechanisms for the anisotropic growth of other materials (Almeida and Alcacer, 1983). In the absence of organic additives, the cathodic electrodeposition of Cu nanocubes can be described as below:

$Cu_2^+ + 2Cl^- + e^- \rightleftharpoons CuCl_2^-$

$CuCl_2^- + e^- \rightleftharpoons Cu + 2Cl^-$

The MWCNTs array also contributes to the formation of the Cu nanocubes because its 3-D structure provides large surface area and many electroactive sites for spatial diffusion, nucleation and growth of Cu nanocubes. This hypothesis is supported by our experimental result that electrodeposition of Cu onto GC surface under the same conditions (but not onto MWCNTs arrays) cannot form cubic morphology.

EIS was used to study the Cu-MWCNTs nanocomposite and to learn the electron transfer behavior between electrolytes and electrode surfaces (**Fig. 2.4F**). The Nyquist complex plane plot of the modified and unmodified MWCNTs electrodes in a 100 mM KCl solution with equimolar $[Fe(CN)^6]^{4-/3-}$ at an applied AC frequency range between 0.1 Hz and 100 kHz. The MWCNTs nearly show a straight line indicating Warburg resistance and the diffusion-limiting step in the electrochemical process (Ren and Pickup 1997b). In contrast, another similar straight line was seen for Cu-MWCNTs nanocomposite electrode suggesting the electrodeposition of Cu nanocubes did not hinder the electron transfer ability of MWCNTs array. In the high frequency region, it can be easily inferred that the internal resistance is smaller after modification of Cu nanocubes than before modification, indicating the role of Cu nanocubes in the electron transfer process is the electron mediator and can therefore increase the heterogeneous electron transfer capability (Ye et al. 2005).

The voltammetric response of the MWCNTs was studied in 5.0 mM $K_3[Fe(CN)_6]$ solution containing 1.0 M KCl as supporting electrolyte to estimate the electrochemical properties and

effective surface area of the synthesized MWCNTs (**Fig. 2.5**). The two obvious characteristic symmetric peaks observed were attributed to the redox reaction of $Fe(CN)_6^{3-}$. The potential peak difference ΔE_p is around 59 mV for MWCNTs electrode at sweep rates from 20 to 500 $mV \cdot s^{-1}$ (Figure S1 Inset), which corresponds well to the theoretical value of 59 mV at 25 °C for one-electron transfer pure-Nernstian behavior. This result revealed good conductivity and an ideal reversibility (Nugent et al. 2001) of redox reactions for the as-synthesized MWCNTs. Under semi-infinite linear diffusion conditions and 25 °C for a reversible process, the effective surface area, A (cm^2) can be calculated in terms of peak current, *I*p (μA) and scan rate, *v* ($mV \cdot s^{-1}$) according to the Randles-Sevcik equation:

$$Ip = 8.51 \times 10^{-3} n^{3/2} A D^{1/2} v^{1/2} C$$

Where, *n* is number of electrons (=1), *C* is concentration (mM), *D* is diffusion coefficient (0.76×10^{-5} $cm^2 \cdot s^{-1}$). The calculated effective area of MWCNTs is 0.064 cm^2. Noticeably, the effective area of the MWCNTs array barely changed after modification of Cu nanocubes (data not shown). Considering the calculated effective surface area and the dimensions of the carbon nanotubes (~10 μm long, ~100 nm diameter), the number of nanotubes on a 3 mm x 3 mm Ta substrate is estimated to be in the order of 10^6 or higher.

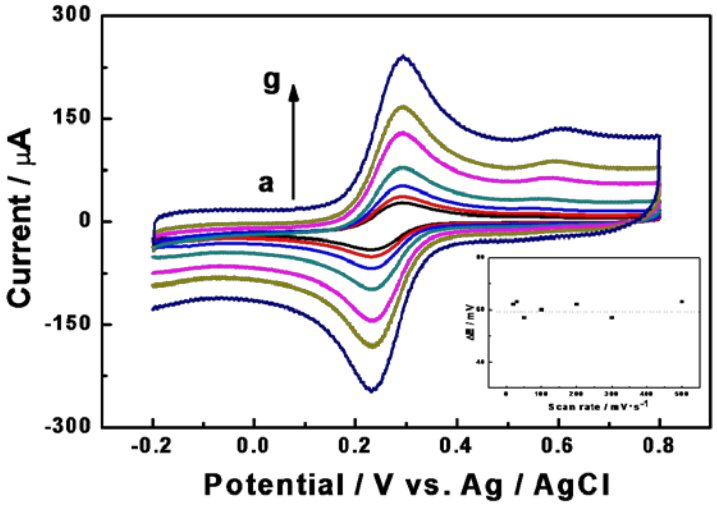

Fig. 2.5: Cyclic voltammograms of MWCNTs electrode in 5 mM $K_3[Fe(CN)_6]$ solution containing 1 M KCl as supporting electrolyte at different scan rates (*v*, $mV \cdot s^{-1}$) (a) 20, (b) 30, (c) 50, (d) 100, (e) 200, (f) 300, and (g) 500 respectively. The inset shows the relationship between the anodic and cathodic peak potential difference (ΔE_p) and *v*.

2.3.1.2 $CoOx \cdot nH_2O$-MWCNTs electrode

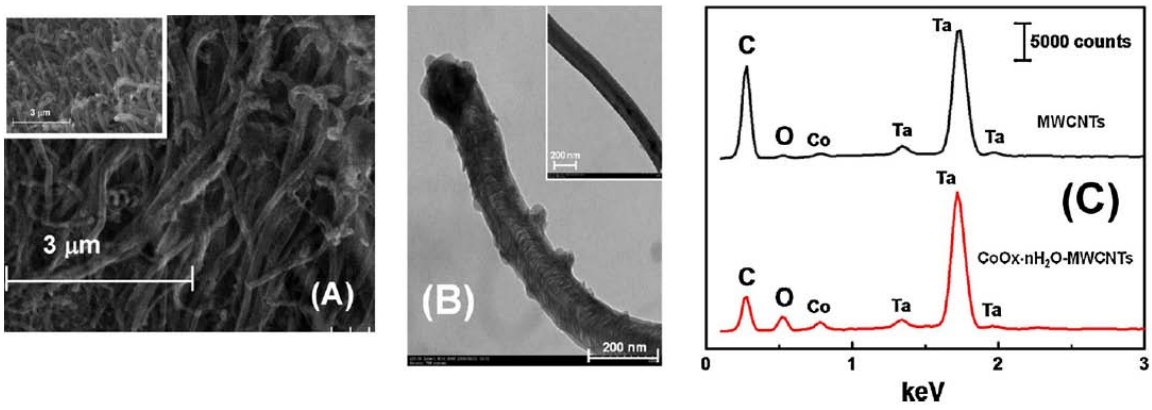

Fig. 2.6: (A) SEM and (B) TEM images of MWCNTs modified with $CoOx{\cdot}nH_2O$ nanostructures and and unmodified MWCNTs (Inset). (C) EDS analysis of MWCNTs and $CoOx{\cdot}nH_2O$-MWCNTs

The morphologies of well-aligned MWCNTs before and after modification with $CoOx{\cdot}nH_2O$ nanostructures examined by SEM show a well-aligned, 3-D vertical array structure (**Fig. 2.6A**) with the nanotubes all about the same height (**Fig. 2.6 inset**). Similar carbon nanofiber networks were achieved by Arumugam et al. (Arumugam et al. 2009). The sidewalls and tips of MWCNTs are fairly smooth and clean, compared to the rougher and thicker surfaces of $CoOx{\cdot}nH_2O$-modified MWCNTs. After electrodeposition in the Co precursor solution with H_2O_2, a thin layer of granular $CoOx{\cdot}nH_2O$ can be observed homogeneously coated on the surface of MWCNTs, indicating the formation of the $CoOx{\cdot}nH_2O$-MWCNTs nanocomposite. The TEM images (**Fig. 2.6B**) show that the $CoOx{\cdot}nH_2O$ nanostructures at the tip are larger and more numerous than those at the sidewalls, which is due to partial shielding from the tips of neighboring MWCNTs (Ye et al. 2005). The $CoOx{\cdot}nH_2O$ nanostructures at the sidewalls appear more spherical, with diameters of 20 to 45 nm. The diameter of the unmodified MWCNT is 110.8±5.5 nm (**Fig. 2.6B inset**), comparable to the literature values of 80 to 120 nm (De Zhang et al. 2002).

EDS data (**Fig. 2.6C**) show the presence of Ta, C, O, and Co elements in the unmodified MWCNTs; Ta is from the substrate, C is from MWCNTs, and Co from the catalyst used during the synthesis of MWCNTs. Identical elements are also present in the $CoOx{\cdot}nH_2O$-MWCNTs nanocomposite, though in different quantities. CoOx·nH2O nanostructures have a larger proportion of O and Co atoms, as observed from the more significant EDS peaks after modification of MWCNTs than before, suggesting the successful modification of MWCNTs with $CoOx{\cdot}nH_2O$. The $CoOx{\cdot}nH_2O$ deposit includes different rather complex and simultaneously present species (i.e., $Co(OH)_2$, CoO, Co_3O_4, Co_2O_3, $CoHO_2$, CoO_2 and various crystallographic

forms of CoOOH) on the electrode surface that are stable in alkaline conditions (Casella 2002). However, the detailed composition and quantities of these species are strictly related to the composition of precursor solution, polarization time, and the deposition potential applied (Casella and Gatta 2002). The formation of $CoOx{\cdot}nH_2O$ nanostructures involves a proton-consuming process of cathodic electrochemical reduction of H_2O_2 into H_2O and a resulting increase in local pH values at the electrode-electrolyte interface (Yan et al. 2008). This will finally lead to the alkalization of Co precursors ($CoCl_2$) at the interface, as shown below:

$$H2O2 + 2H+ + 2e- \rightleftharpoons 2H2O$$

$$Co(II) + OH- \rightleftharpoons \text{cobalt oxides/hydroxides species}$$

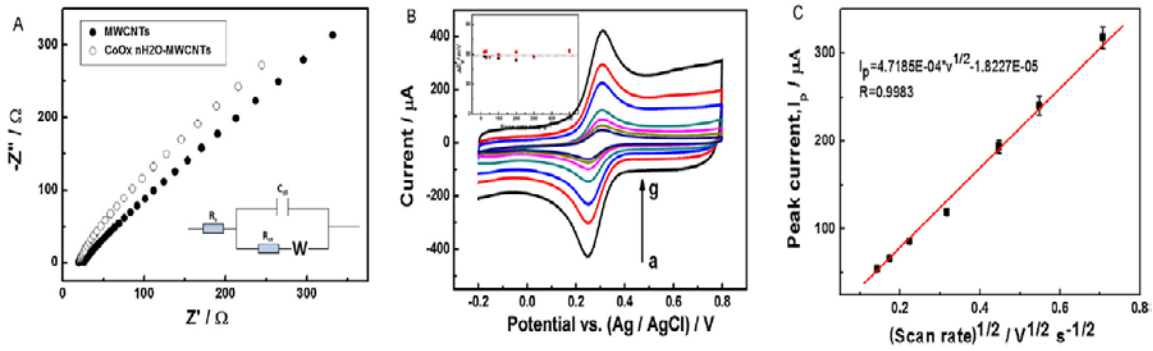

Fig. 2.7: (A) EIS of MWCNTs (●) and $CoOx{\cdot}nH_2O$-MWCNTs nanocomposite electrodes (○) in 100 mM KCl electrolyte solution containing equimolar $[Fe(CN)_6]^{4-/3-}$. Frequency range: 0.1 Hz-100 kHz. Inset shows the equivalent circuit, $R_s(C_{dl}[R_{ct}W])$, used to fit the impedance data. (B) Cyclic voltammograms of $CoOx{\cdot}nH_2O$-MWCNTs nanocomposite electrode in 5 mM $K_3[Fe(CN)_6]$ containing 1 M KCl. Scan rates from a to g represent 20, 30 50, 100, 200, 300 and 500 $mV{\cdot}s^{-1}$ respectively. Inset shows the relationship between the peak potential difference and scan rates for both unmodified MWCNTs (●) and $CoOx{\cdot}nH_2O$-modified MWCNTs electrodes (■) and the dotted line indicates the value of 59 mV. (C) Peak currents as a function of square root of potential scan rate. Error bars denote the standard deviation of triplicate measurements.

Nyquist plot from EIS for MWCNTs and $CoOx{\cdot}nH_2O$-MWCNTs electrodes (**Fig. 2.7A**) reveals characteristic features of the electron transfer between the electrolyte and the electrode surface. The unmodified MWCNTs electrode displays almost straight line as a characteristic for Warburg resistance, indicating a diffusion process (Ren and Pickup 1997a). Similarly, another straight line observed for the $CoOx{\cdot}nH_2O$-MWCNTs nanocomposite assures that the rapid electron transfer capability of MWCNTs still remains after modification with $CoOx{\cdot}nH_2O$. Furthermore, in the high frequency region, the internal resistance of $CoOx{\cdot}nH_2O$-MWCNTs electrode is about 6Ω lower than what it was before modification (Ye et al. 2005), indicating that

the modification of MWCNTs with semiconductor $CoOx{\cdot}nH_2O$ increases the conductivity and electron transfer. In the equivalent circuit model for $CoOx{\cdot}nH_2O$-MWCNTs electrode (**Fig. 2.7A inset**), Rs indicates the solution resistance, Cdl is the couble layer capacitance and Rct is the charge transport resistance between the electrolyte and electrode. The model fit well with the impedance data of $CoOx{\cdot}nH_2O$-MWCNTs nanocomposites with a very small Rct (<1Ω) indicating the good electrical contact between electrolyte and the electrode surface and the facilitated interfacial electron transfers (Choi et al. 2010).

The electrochemical properties and effective surface area of the $CoOx{\cdot}nH_2O$-MWCNTs electrode, evaluated by voltammetric responses in 5 mM $K_3[Fe(CN)_6]$ with 1 M KCl supporting electrolyte, are presented in **Fig. 2.7B**. In the scan rate range of 20 to 500 mV·s-1, the potential separation of the anodic and cathodic peaks (ΔEp) for MWCNTs before and after modification are around 59 mV (**Fig. 2.7B inset**, dotted line), implying that the rapid electron-transfer kinetics and conductivity of MWCNTs are retained after modification with $CoOx{\cdot}nH_2O$. Notably, this result is in agreement with the theoretical value of 59 mV at 25 °C for one-electron transfer pure-Nernstian behavior between $[Fe(CN)_6]^{4-/3-}$ redox couples, showing ideal reversibility. Furthermore, the peak currents show a linear dependence (R=0.998) on the square root of the scan rate ($v^{1/2}$) at the $CoOx{\cdot}nH_2O$-MWCNTs electrode (**Fig. 2.7C**), which suggests that the redox reaction is a diffusion-controlled process and is nearly reversible (instead of quasi-reversible or irreversible), with a linear Randles' slope of 4.72×10^{-4} $A{\cdot}V^{-1/2}{\cdot}s^{1/2}$. For a reversible process under semi-infinite linear diffusion conditions at 25 °C, the effective surface areas (A, cm^2) of MWCNTs and $CoOx{\cdot}nH_2O$-MWCNTs electrodes were estimated to be 0.078±0.004 and 0.11±0.008 cm^2, according to redox peak currents (Ip, μA) from **Fig. 2.7B** and the Randles-Sevcik equation: $Ip = 2.69\times10^5 * n^{3/2} A D^{1/2} v^{1/2} C$. Where, n is number of electrons (=1), C is concentration (mol/cm^3), D is diffusion coefficient (0.76×10^{-5} $cm^2{\cdot}s^{-1}$), and v is scan rate ($V{\cdot}s^{-1}$). Therefore, after modification with $CoOx{\cdot}nH_2O$ nanostructures, the electroactive surface area of MWCNTs increased by about 41%, which provides additional electroactive sites and more effective contacts with analyte molecules. Based on the diameter, length, and effective surface area of MWCNTs, the number of nanotubes on a 3 mm x 3 mm Ta substrate is estimated to be in the order of 10^6, similar to what is reported in the published data (Ye et al. 2004a).

2.3.2 Optimization of the sensors

2.3.2.1 Cu-MWCNTs electrode

The dependence of the peak current and potential of the catalytic oxidation of 1.0 mM Glc on NaOH concentrations at the Cu-MWCNTs electrode was investigated by CV, as shown in **Fig.2.8A**. The oxidation peak current increased with pH (i.e., NaOH concentration). The potential first shifted sharply towards negative value with increased NaOH concentration, but when the concentration was over 0.1 M, the potential increased almost linearly. This illustrates that high pH can improve the Glc oxidation, which is consistent with the fact that the catalytic reaction of Glc involves OH^- group. Nonetheless, if high potentials or high pH values are applied, it could probably oxidize many reactive interferents that usually co-exist with Glc in some samples and might produce many unwanted intermediate species that could interact with electrode surface or materials in the samples, blocking the ongoing catalytic oxidation of Glc. These extreme conditions could also erode or damage the electrodes. As a result, 0.1 M NaOH (pH=13.0) was selected as the optimal concentration because of its satisfactory peak current and low oxidation potential.

The optimal detection potential was determined through dropwise addition of 0.1 mM Glc in 0.1 M NaOH at 100 $mV \cdot s^{-1}$, with the range of +0.1 V to +0.6 V detection potentials applied (**Fig. 2.8B**). The current responses to Glc were under +0.3 V. The signal increased significantly at detection potential +0.5 V and reaching a maximum value at +0.55 V, which was even higher than the response at +0.6 V. Thus, based on both the highest current response and the fact that high potential may oxidize many unwanted species and generate intermediate interferents, +0.55 V was selected as the optimal detection potential.

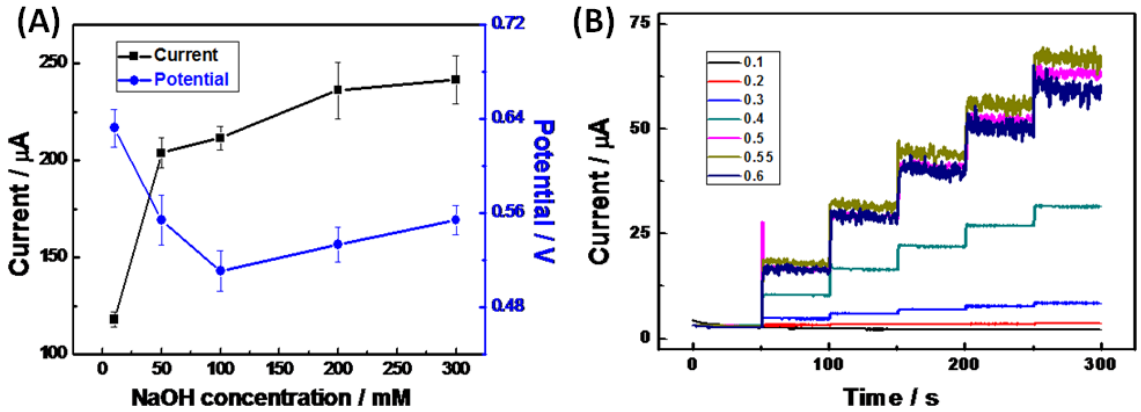

Fig. 2.8: (A) Effect of NaOH concentration on peak current (■) and peak potential (●) for 1.0 mM Glc at the Cu-MWCNTs electrode (scan rate: 100 $mV \cdot s^{-1}$). Error bars indicate standard deviations for triplicate measurements. **(B)** Current-time response of Cu-MWCNTs electrode at different potentials from +0.1 V to +0.6 V upon successive addition of 0.1 mM Glc in 0.1 M NaOH.

2.3.2.2 CoOx·nH2O-MWCNTs electrode

As illustrated above, OH- is in need for the electrochemical oxidation of Glc and redox conversions of $CoOx \cdot nH_2O$ species into reactive high-valence species towards Glc. Therefore, it is necessary to investigate the effects of NaOH concentration (pH), to optimize the Glc detection at the $CoOx \cdot nH_2O$-MWCNTs electrode. **Fig. 2.9A** displays the influence of NaOH concentration on the oxidation peak current and potential in CVs. In determining the best NaOH concentration of the carrier solution to obtain the highest current response and the lowest potential, multiple circumstances must be considered. With the NaOH concentration increasing from 10 mM to 2000 mM, the peak current increased continuously and the peak potential decreased correspondingly, showing higher catalytic activity against Glc with increasing pH in alkaline solutions. Noticeably, the current response did not increase significantly with NaOH concentration past 200 mM over the peak potential range of 100 to 500 mM. Also with regards to the many oxidizable compounds at high potentials and high pH values possibly leading to unexpected interference and hindrance of Glc determination, 0.2 M NaOH was chosen as the optimal carrier solution to achieve an acceptable and stable response at relatively low potential.

The optimal operating potential for sensing Glc with the $CoOx \cdot nH_2O$-MWCNTs electrode was determined by amperometric responses towards dropwise addition of 0.1 mM Glc in 0.2 M NaOH, as presented in Figure 3C. The current responses to 0.1 mM Glc under detection potentials from +0.30 to +0.60 V in +0.05 V increments are 0.449±0.048, 0.578±0.053, 0.773±0.052, 1.521±0.038, 2.132±0.312, 3.016±0.419, 2.890±0.476 μA, respectively. The signals increased steadily in the range of +0.30 to +0.45 V and nearly doubled at +0.50 V; it reached a maximum at +0.55 V. This finding is in good agreement with the Glc oxidation peak at +0.55 V from CV (**Fig. 2.9B**, c) and the voltammetric behavior of CoOOH/CoO2 redox transition at +0.55 V in 0.2 M NaOH (**Fig. 2.9B**, d), indicating Co(III) and Co(IV) species play the most important role in Glc oxidation. Consequently, +0.55 V was selected as the optimal operating potential.

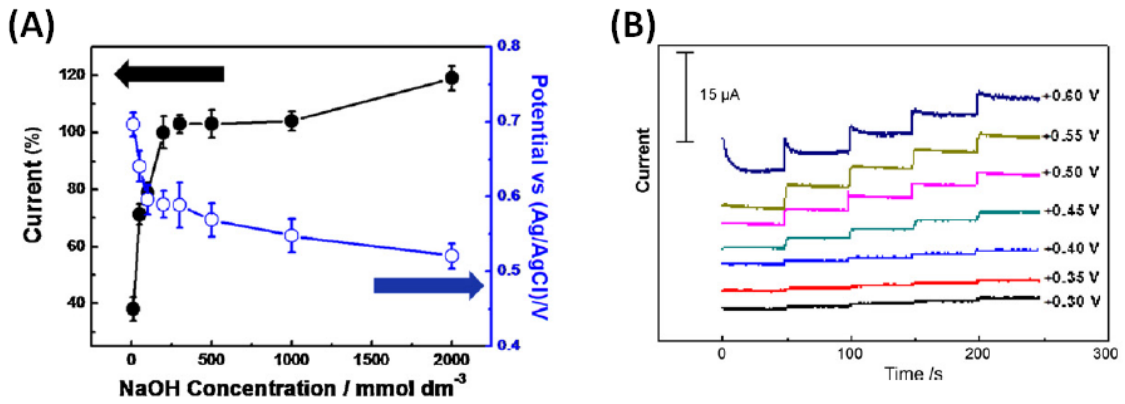

Fig. 2.9: (A) Effect of pH on peak current (●) and peak potential (○) to 2.5 mM Glc for the $CoOx{\cdot}nH_2O$-MWCNTs electrode in different NaOH concentrations of 10, 50, 100, 200, 300, 500, 1000 and 2000 mM. Error bars denote the standard deviation of triplicate measurements. (B) Current-time responses with a dropwise addition of 0.1 mM Glc at different detection potentials at +0.30 V, +0.35 V, +0.40 V, +0.45 V, +0.50 V, +0.55 V and +0.60 V.

2.3.3 Analytical performance of the sensors

2.3.3.1 Cu-MWCNTs electrode

The electrocatalytic performance of the umodifiied MWCNTs and Cu-modified MWCNTs electrodes was investigated by CV in 0.1 M NaOH with 1.0 mM Glc at 100 $mV{\cdot}s^{-1}$. **Fig. 2.10A** shows the typical voltammetric responses for the electrodes. No oxidation peaks were observed in the absence of Glc for both electrodes. When Glc was present, a negligibly small current response was obtained for the unmodified MWCNTs. This small response is probably due to the carbon nanotubes or the contributions from tiny amount of Co catalyst remaining after the synthesis of MWCNTs (Ye et al. 2004b). It has been frequently reported that the electrochemical catalytic activities of MWCNTs were mainly caused by the impurities of metal or metal oxide in the synthesized MWCNTs (Banks et al. 2006; Batchelor-McAuley et al. 2008c). As for the Cu-MWCNTs electrodes, their current responses increased rapidly and exhibited obvious anodic oxidation peaks starting from +0.35 V to +0.65 V in response to the addition of Glc. This suggests that Cu is responsible for the Glc oxidation, with its catalytic activity against Glc and large surface area of the nanocubes. Therefore, as our data show, the current response of Cu-MWCNTs electrode is much higher than that of the MWCNTs electrode. In addition, there was almost a 100 mV negative potential difference between the peaks of Cu-MWCNTs (~0.48 V) and MWCNTs (~0.58 V) electrode signals, which mean Cu-MWCNTs electrode is well suited for oxidation of Glc. This negative potential shift as well as the higher current response for Cu-

MWCNTs electrode not only establishes its superiority over the unmodified MWCNTs electrode but also confirms the important role the Cu nanocubes plays in the electrocatalytic performance towards Glc oxidation due to the electroactive sites provided by the Cu nanostructure. In addition, no obvious cathodic peaks were observed, i.e., the oxidation of Glc by Cu is irreversible. A standard addition of 0.2 mM Glc in 0.1 M NaOH was also studied by linear sweep voltammetry (LSV) at the Cu-MWCNTs electrode at 100 $mV \cdot s^{-1}$ after each addition (**Fig. 2.10B**). A gradual increase in the current was measured with the increased Glc concentration, pointing to the potential for developing Cu-MWCNTs electrode as a generic non-enzymatic sensor. Cyclic voltammograms of Cu-MWCNTs electrode in 0.1 M NaOH with 1.0 mM Glc were recorded at different scan rates (**Fig. 2.10C**). The anodic peak current (Ip) due to oxidation of Glc increased with increased scan rates but the anodic peak potential shifted to positive values with increased scan rates. The Ip vs. scan rate, v (from 20 to 500 $mV \cdot s^{-1}$) plot (Figure 2C Inset) was highly linear (R2=0.993): Ip=88.25+0.769*v). The result verifies that the electrochemical kinetics is controlled by surface adsorption of Glc molecules.

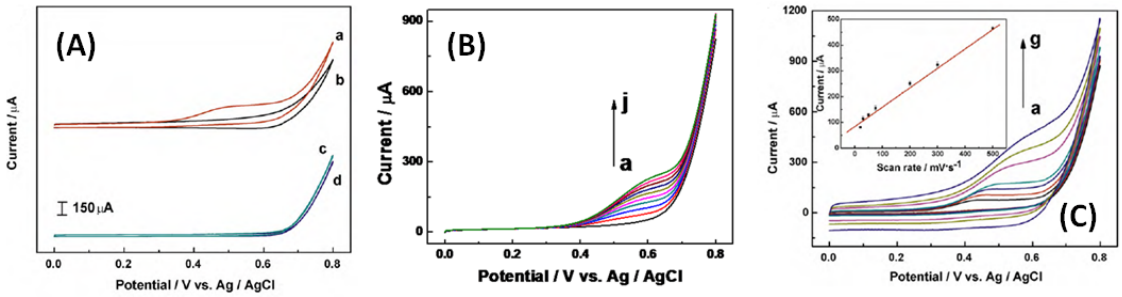

Fig. 2.10: (A) Cyclic voltammograms of Cu-MWCNTs electrode (a and b) and unmodified MWCNTs electrode (c and d) in the absence (b and d) and presence (a and c) of 1.0 mM Glc in 0.1 M NaOH. (B) Linear sweep voltammograms (LSV) of Cu-MWCNTs electrode for 0.2, 0.4, 0.6, 0.8, 1.0, 1.2, 1.4, 1.6, 1.8 and 2.0 mM Glc (a to j respectively) in 0.1 M NaOH at 100 mV • s^{-1}. (C) Cyclic voltammograms of Cu-MWCNTs electrode at different scan rate from 20 mV • s^{-1} to 500 mV • s^{-1} (a to g) in 0.1M NaOH with 1.0 mM Glc. Inset shows the dependence of the oxidation peak current of Glc on scan rate.

The amperometric responses of MWCNTs and Cu-MWCNTs electrodes for a successive addition of 0.2 mM Glc per 50 s in 0.1 M NaOH at optimal potential of +0.55 V are shown in **Fig. 2.11A**. As expected, the MWCNTs electrode shows extremely low current response, and the Cu-MWCNTs electrode produced significantly higher signals and generated steady-state current rapidly within 1 s (**Fig. 2.11A inset**). This extraordinarily fast response is in agreement with fast diffusion of Glc molecules in the 3-D network of MWCNTs arrays-Cu nanocubes and fast electron transfers. The response is much faster than those reported for Cu nanocluster/MWCNTs/GC

(<5s) (Kang et al., 2007), SWCNTs/Cu/Nf (10s) (Male, et al., 2004), MWCNTs electrode (<10s) (Ye et al., 2003). As shown in **Fig. 2.11B**, the current response, *i* (μA) vs. Glc concentration *C,* (mM) was linear (R^2=0.996) up to *C*=7.5 mM: *i*=26.60+70.16**C*. According to this, the sensitivity of Cu-MWCNTs nanocomposite electrode is 1096 $\mu A \cdot mM^{-1} \cdot cm^{-2}$, and the detection limit is 1.0 μM with a signal-to-noise ratio of 3. The key performance characteristics of different Cu-, Cu_2O or CuO-based non-enzymatic Glc sensors are compared in **Table 2.1**. Among these, our Cu-MWCNTs sensor boasts the best sensitivity and widest linear range. The fast and sensitive catalytic performance is due to the promoted electron transfer, large aspect ratio, highly active surface area, and superb catalytic activity afforded by the nanocomposite structure of Cu nanocubes and MWCNTs arrays.

The electrocatalytic oxidation process of Glc at Cu-based electrodes is generally regarded to undergo several steps involving strong oxidizing intermediates like $CuOOH^{\cdot}$ or $Cu(OH)_4^-$. At cathodic potentials and basic conditions, Cu is firstly oxidized into CuOH and Cu_2O intermediates which are further oxidized into CuO. CuO can be electrochemically oxidized into strong oxidizing Cu(III) species such as $CuOOH^{\cdot}$ or $Cu(OH)_4^-$. Glc will be catalytically oxidized with the active oxidizing species, with a C-C bond cleavage for Glc in alkaline solutions and the generation of lower-molecular-weight products (Luo and Baldwin 1995; Wei et al. 2009). Possible mechanisms are as below:

$$Cu + OH^- - e \rightleftharpoons CuOH$$

$$2CuOH + OH^- \rightleftharpoons Cu_2O + 2H_2O$$

$$Cu_2O + 2OH^- - 2e \rightleftharpoons 2CuO + H_2O$$

$$CuO + OH^- - e- \rightleftharpoons CuOOH^{\cdot} \quad \text{or} \quad CuO+H2O+2OH^- -e- \rightleftharpoons Cu(OH)_4-$$

For Glc, the reaction can be summarized as below:

$$Cu(III)+R1\text{-}CHOH\text{-}R2 \rightleftharpoons R1\text{-}CHO\text{-}R2 + Cu(II)$$

Table 2.1: Comparison of key features of our proposed Cu-nanocube modified MWCNTs array Glc sensor with other published amperometric non-enzymatic Glc sensors from a copper source.

Electrode type (Reference)	Sensitivity ($\mu A \cdot mM^{-1}$or $\mu A \cdot mM^{-1} \cdot cm^{-2}$)	Linear range (up to, mM)	Detection limit (μM)	Operational potential (V)
CuO nanowires (Zhuang et al. 2008)	490.0	2.0	0.05	+0.33
Cu nanocluster/MWCNTs (Kang et al. 2007)	253.0	3.5	0.21	+0.65
CuO nanospheres (Reitz et al. 2008)	404.5	2.6	N/A	+0.60
Cu/self-assembled MWCNTs (Li et al. 2009b)	602.0	1.8	10	+0.55
CuO nanorod bundles (Batchelor-McAuley et al. 2008a)	450.0	1.0	1.2	+0.60
Porous CuO (Cherevko S. 2010)	2.9	2.5	0.14	+0.65
CuO nanofibers (Wang W. 2009)	431.3	2.5	0.8	+0.40
Cu nanocubes-MWCNTs array (this paper)	1096.3	7.5	1.0	+0.55

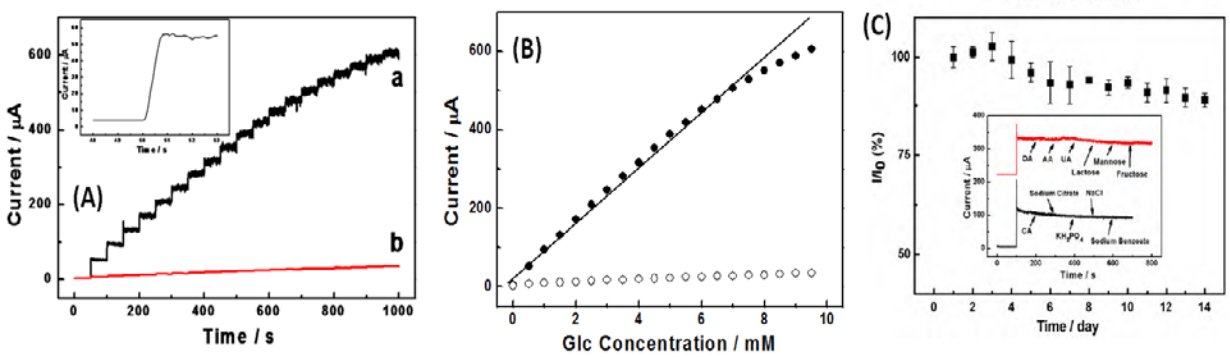

Fig. 2.11: (A) Amperometric responses at +0.55 V with a dropwise addition of 0.2 mM glucose every 50s for Cu-MWCNTs electrode (a) and unmodified MWCNTs array electrode (b). Inset exhibits the response time of Cu-MWCNTs to Glc added. (B) The dependence of the current response vs. glucose concentration for Cu-MWCNTs electrode (a) and unmodified MWCNTs array electrode (b). (C) Stability test of the sensor stored at ambient conditions over 2 weeks in 0.1M NaOH with addition of 0.1mM glucose at +0.55 V. The current respponse for Day 1 is assigned as I_0. The error bars indicate the standard deviation of five different measurements. The inset shows the interference test of the sensor in 0.1 M NaOH at +0.55 V with 1.0 mM Glc and other interferents in a certain ratio as indicated in **Table 2.2**.

The stability of the sensor was evaluated by measuring the current response towards Glc of a freshly made Cu-MWCNTs electrode on day 1 (I_0) and after storage, in a desiccator at room temperature, for few days (I) over two weeks (**Fig. 2.11C**). Five parallel measurements were taken, as indicated by the error bars. The variation in the current responses was under 4% during the first four days, reaching a maximum of less than 12% after two weeks. The reproducibility was examined for five identically-made electrodes with a relative standard deviation (RSD) of 4.3% while 10 measurements for the same electrodes were taken upon the addition of 0.1 mM Glc in 0.1 M NaOH with the RSD of 6.4%, demonstrating excellent reproducibility. Meanwhile, it has been reported that non-enzymatic sensors based on metals (Reitz et al. 2008) or alloys (Sun et al. 2001) could easily lose their electroactivity in the presence of chloride ions, due to the formation of cuprous chloride and/or cuprous chloride complexes (Yuan et al. 2009). However, we did not observe that with our Cu-MWNCTs electrode while sensing of Glc in 0.1 M NaOH solution with 0.1 M KCl; the current response remained almost steady, confirming excellent stability of our sensor against chloride poisoning.

A number of oxidizable interfering species could co-exist with Glc in many samples. Therefore, it is necessary to investigate if such interferents could generate current responses comparable to that corresponding to Glc. The normal physiological level of Glc in human blood is 3 to 8 mM compared to about 0.1 mM of interfering species (with Glc:interferents ratio of more than 30:1) (Zhuang et al. 2008), while the Glc:interferents ratio is even higher in food samples.

The measured effects of different interferents along with Glc in a carrier solution of 0.1 M NaOH at +0.55 V of operating potential are shown in Figure 3C Inset. The interferents tested, at Glc:interferents ratio of either 5:1 or 20:1, include dopamine (DA), ascorbic acid (AA), uric acid (UA), lactose, mannose, fructose, citric acid, sodium citrate, potassium dihydrogen phosphate, sodium chloride and sodium benzoate. The current responses of all the interferents except citric acid were less than 5% (Table S1). The citric acid, a weak organic acid, which is usually a preservative in soft drinks and other foods, had a slightly higher influence of 7.4%, but it was still very small. These results indicate that Cu-MWCNTs electrode is highly specific to Glc even in the presence of several interfering species normally found in food and biological samples.

Interferents	Molar ratio (D-(+)-glucose:interferent)	Current ratio with respect to Glc (%) [a]
Dopamine	20:1	0.93
Ascorbic acid	20:1	1.11
Uric acid	20:1	3.99
Lactose	20:1	5.08
Mannose	20:1	2.41
Fructose	20:1	0.37
Citric acid	5:1	7.39
Sodium citrate	5:1	3.65
Potassium dihydrogen	5:1	2.44

phosphate		
Sodium chloride	5:1	1.20
Sodium benzoate	5:1	1.22

Table 2.2: Effect of interferents on Glc determination using the Cu-MWCNTs electrode

We tested the performance of the Cu-MWCNTs electrode by measuring Glc content in human serum blood samples. The blood samples were obtained in a hospital for fasting blood sugar test from five patients (four non-diabetic and one diabetic), and all experiments were done within 30 min of drawing the blood. 20 μL blood sample was added to a 20 mL 100 mM NaOH test solution and the optimal detection potential of +0.55 V was applied to record the current responses (**Table 2.3**). These results corresponded well with the blood test results conducted by the hospital. The blood Glc concentrations of non-diabetic patients were between 4.44 and 5.16 mM, which are in the normal range of 3 to 8 mM. As expected, the diabetic patient had a high blood Glc level of 12.73 mM. For all the tests, 0.1 mM standard Glc was added to calculate the recovery rate and our sensor exhibited a good recovery (>90%). These results validate the potential for Cu-MWCNTs electrode to be used as sensors for routine blood Glc sensing.

Table 2.3: Determination of Glc concentrations in human blood serum samples

Sample	Glc concentration measured by hospital instrument	Glc concentration measured with our sensor	RSD[b] (%)	Added Glc (mM)	Recovery rate (%)
1	4.56	4.44	5.83	0.1	97
2	5.24	5.16	3.52	0.1	99

3	5.02	4.92	2.95	0.1	96
4	5.00	4.91	4.55	0.1	92
5 [a]	12.80	12.73	6.53	0.1	94

[a] This individual is a known diabetic

[b]Relative Standard Deviation

2.3.3.2 CoOx·nH2O-MWCNTs electrode

The electrocatalytic activities of MWCNTs and CoOx·nH_2O-MWCNTs electrodes towards oxidation of Glc in alkaline conditions, studied by CVs in 0.2 M NaOH solution, are shown in **Fig. 2.12A**. In the blank NaOH solution without Glc, there are no distinguishable peaks for the MWCNTs electrode (**Fig. 2.12A inset**, b), whereas there are two sets of peaks observed for the CoOx·nH2O-MWCNTs electrode (**Fig. 2.12A**, d) demonstrating the presence of CoOx·nH2O species on the electrode surface. The first anodic peak lies at about +0.3 V, while the corresponding cathodic peak, though not prominent, is at about +0.2 V. In contrast, the second anodic and cathodic peaks are around +0.55 V. These results are similar to those of Gasella and Gatta (Casella and Gatta 2002). However, compared to their results obtained employing a moderatly alkaline solution of 10 mM NaOH, the peaks we obtained are not as sharp since we used a highly alkaline solution (0.2 M NaOH). These two sets of redox peaks can be ascribed to the following redox reactions happening in alkaline solutions between Co_3O_4/CoOOH and CoOOH/CoO_2 species, respectively (Casella and Gatta 2002; Castro et al. 1998):

$$Co_3O_4 + OH^- + H_2O \rightleftharpoons 3CoOOH + e^-$$

$$CoOOH + OH^- \rightleftharpoons CoO_2 + H_2O + e^-$$

Actually, there should be another small redox couple, indicating the electrochemical conversion between hydrous Co(II) and Co_3O_4:

$$3Co(OH)_2 + 2OH^- \rightleftharpoons Co_3O_4 + 4H_2O + 2e^-$$

Nevertheless, this pair of redox peaks often overlaps with that of Co_3O_4/CoOOH and are only present with negative potential limits lower than -0.2 V (Casella and Gatta 2002), hence sometimes go unreported. Due to the low potential limit we applied, this redox couple is not seen in our results. When 5.0 mM Glc was added, the MWCNTs electrode did not show any obvious oxidation peaks but only a negligible response against Glc (**Fig. 2.12A inset**, a), which may be due to the remnants of Co catalyst used in the synthesis of the MWCNTs (De Zhang et al. 2002). The Ni, Co, and more commonly, Fe metal catalysts used for growing CNTs have been reported responsible for the electrocatalysis observed at CNTs-modified electrodes (Banks et al. 2006). With the addition of 2.5 mM Glc, the current response towards Glc at the CoOx·nH_2O-MWCNTs electrode rose rapidly from +0.30 V, with an oxidation peak at about +0.55 V (**Fig. 2.12A**, c). This oxidation of Glc lies in the potential region in accordance with the redox peak pairs of Co_3O_4/CoOOH and CoOOH/CoO_2, suggesting the formation of active high-valence species (i.e., Co(III) and Co(IV)) such as CoOOH and CoO_2, which act both as an electron mediator and a catalyst in the electrocatalytic process (Casella and Gatta 2002). This direct catalysis of Glc possibly involves the generation of reactive free radicals and/or intermediate species as well as participation of OH-, since under neutral or acidic conditions no obvious current responses were visible at the CoOx·nH_2O-MWCNTs electrode with added Glc. Glc can reduce the high valence cobalt species formed under anodic polarization (Buratti et al. 2008). The current response of 2.5 mM Glc at the CoOx·nH2O-MWCNTs electrode is much larger than that obtained for 5.0 mM Glc at MWCNTs, indicating that the catalytic reaction is induced by the modification of MWCNTs with CoOx·nH2O nanostructures. The electrocatalytic activity of CoOx·nH_2O species is claimed to be determined by the specific chemical and physical status of the CoOx·nH_2O nanostructures electrochemically deposited on the electrode (Buratti et al. 2008).

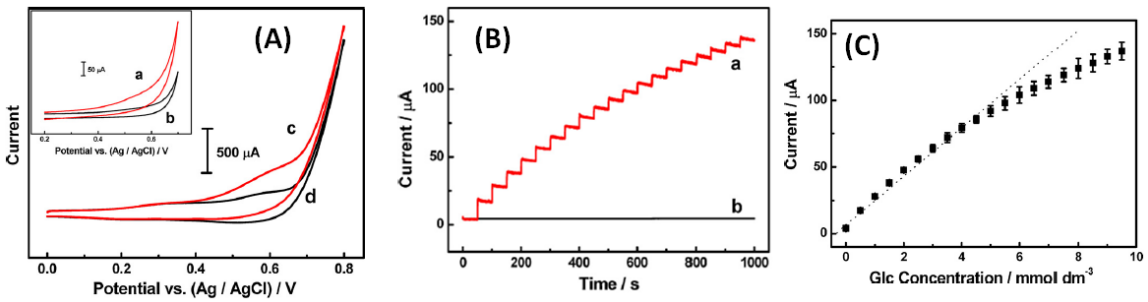

Fig. 2.12: (A) CVs of unmodified MWCNTs electrode in the presence (a) and absence of 5 mM Glc (b), and CoOx·nH_2O-MWCNTs electrode in the presence (c) and absence (d) of 2.5 mM Glc in 0.20 M NaOH. Scan rate: 100 mV·s^{-1}. (B) Current-time response with dropwise addition of 0.5 mM Glc at (a) the CoOx·nH_2O-

MWCNTs electrode and (b) the unmodified MWCNTs electrode. (C) The linear dependence of current (*i*, μA) on Glc concentration (*C*, mM) at CoOx·nH_2O-MWCNTs electrode is represented by the dotted line (R=0.9953): (*i*=8.92+17.91*C*). Error bars denote the standard deviation of triplicate measurements. Applied potential: +0.55V.

The amperometric sensing of Glc at the unmodified MWCNTs and CoOx·nH_2O-MWCNTs electrodes was evaluated in the optimal carrier solution of 0.2 M NaOH under the optimal detection potential of +0.55 V, with successive addition of 0.5 mM Glc (**Fig. 2.12B**). Consistent with the results from CV (**Fig. 2.12A and inset**), after modification of CoOx nanostructures, the CoOx·nH_2O-MWCNTs exhibited a significantly larger current response towards Glc than the unmodified MWCNTs electrode. The response at CoOx·nH_2O-MWCNTs electrode initially appears stable and well-defined, but it decreased gradually with continuous addition of Glc. The decrease in sensitivity of current response is due to the increasing Glc concentration and time, because the production of reaction intermediates in the electrocatalytic process tends to be adsorbed on the active catalytic sites of CoOx·nH_2O on MWCNTs, finally reaching a threshold hinders their activities, which leads to the reduction of current responses. The current response (i, μA) of CoOx·nH_2O-MWCNTs shows a linear dependence (R=0.995) on concentration (C, mM) up to 4.5 mM Glc, with a sensitivity of 162.8 $\mu A \cdot mM^{-1} \cdot cm^{-2}$ (**Fig. 2.12C**), as modeled by a linear regression equation: i=8.92+17.91*C. The detection limit of the sensor is 2.0 μM at a signal/noise ratio of 3. The sensitivity of our sensor (17.9 μA·mM-1) is fairly high – about 4 times better than that of CoOx·nH_2O-modified GC electrode (4.0 μA·mM-1) reported by Casella and Gatta(Casella and Gatta 2002); and the detection limit is very low – about 35 times lower than that of a a cobalt oxide/MWCNTs based sensor reported by Buratti and coworkers (Buratti et al. 2008). Though there are no pure non-enzymatic Co-based Glc sensors reported, the sensitivity of our sensor is 15 times better than what Chen et al. (Chen et al. 2010) reported recently for their Pd-MWCNTs Glc sensor. Thus, our non-enzymatic CoOx·nH_2O-MWCNTs electrode is a promising candidate for analytical Glc sensing applications.

Interfering electrochemical signals from easily-oxidizable compounds (i.e., AA, UA, DA, sugars and etc.) have become a major challenge for non-enzymatic Glc sensors. These compounds that co-exist with Glc in samples for analysis such as human blood serum and beverages, can be simultaneously oxidized with Glc, affecting current signals. Although the concentration of Glc, 3 to 8 mM, is at least more than 30 times higher than that of AA (0.1 mM) and UA (0.02 mM) in an analytical physiological sample, it has been reported that these species,

as well as others, can produce comparable current signals to Glc due to their faster electron transfers (Chen et al. 2010; Park et al. 2003), and some carbohydrates may also affect the current responses (Batchelor-McAuley et al. 2008b). We tested the influence of a number of potentially co-existing interferents (in a higher ratio than in physiological fluids to overcome any possible interference from these samples) on the Glc determination by successively adding them one after another in 100 s intervals for amperometric responses. The current-time response showed an almost straight line with unchanged current signal from Glc and negligible signals from all the inteferents added, indicating the interferent-free, robust and stable current generated by Glc. Our results show Glc can generate remarkably higher current responses than all inteferents (**Table 2.4**). Only citric acid, UA, and AA produced somewhat large interfering signals, yet they are only 1.55 to 3.57 % of the response from Glc. The anti-interference ability of our sensor against UA and AA are much better than an unmodified MWCNTs electrode reported by Ye et al. (Ye et al. 2004b) The good specificity of our sensor suggests that it can perform well enough for interference-free Glc detection in complex matrices such as body fluids.

Table 2.4: Influence of common interferents on glucose determination for the $CoOx{\cdot}nH_2O$ -MWCNTs electrode

Interferent	D(+)-glucose:interferent molar ratio	Current ratio* (%)
Dopamine	20:1	0.65
Ascorbic acid	20:1	3.57
Uric acid	20:1	3.29
Lactose	20:1	0.25
Mannose	20:1	0.21
Fructose	20:1	0.62
Citric acid	5:1	1.55
Sodium citrate	5:1	0.91
Potassium dihydrogen phosphate	5:1	0.71
Sodium chloride	5:1	0.14
Sodium benzoate	5:1	0.13

*Applied potential: +0.55 V

Another challenge for non-enzymatic sensors based on metals, metal oxides or metal alloys is that they are prone to poisoning by chloride ions and thus lose their catalytic activity (Li et al. 2007). However, in our experiments with addition of 0.15 M NaCl to 0.2 M NaOH, to mimick physiological conditions, there was no obvious current decrease due to chloride poisoning. The stability of the sensor was evaluated by repetitive CVs (more than 1000 cycles) in 0.2 mM NaOH containing 1 mM Glc (**Fig. 2.13A**). The peak potential and current remain quite stable with only a loss of 10.4% in current response at +0.55 V where the oxidation peak of Glc appears. The long-term stability of the sensor was examined by testing its sensitivity every other day in one month (**Fig. 2.13AB**). The sensor still retained 91.73% of its original sensitivity in current response after being stored in atmosphere at room temperature for as long as one month. Its high stability is probably attributed to the stability of CoOx·nH2O in alkaline solutions (Casella 2002), and the more electrocatalytic sites on CoOx·nH2O-MWCNTs nanocomposites free from being blocked by Cl- or intermediates generated during Glc oxidation.

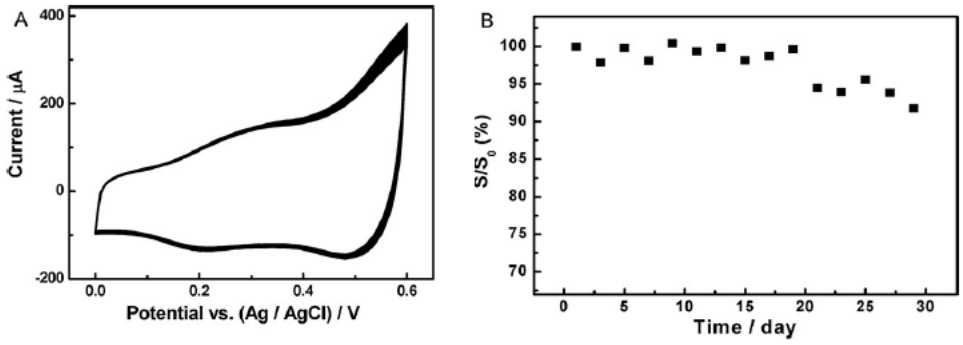

Fig. 2.13: (A) 1000 cycles of repetitive CVs for CoOx·nH_2O-MWCNTs electrode in 0.2 M NaOH with 1 mM Glc. (B) Long-term stability of the CoOx·nH_2O-MWCNTs electrode toward 0.1 mM Glc over one month period.

The reproducibility of our sensor was examined by using the same electrode to measure 0.1 mM Glc 10 times (n=10) and using five different electrodes (n=5) made under identical conditions to measure 0.1 mM Glc. The relative standard deviations (RSD) are 3.3 % and 6.7 % respectively, confirming the good reproducibility of the sensor. The response time of the sensor towards Glc to achieve steady-state current is within 4 s which is faster than some other sensors (<10 s).(Male et al. 2004; Ye et al. 2004b) In Male's work (Male et al. 2004), though Nafion may prevent chloride ion poisoning and inteferences to a large degree, it could also hinder Glc molecules from diffusing and being adsorbed onto the electroactive sites of the sensor, with a slower response. The rapid response of our sensor is probably due to promoted electron

transfers, more electroactive sites on the $CoOx{\cdot}nH_2O$-MWCNTs nanocomposites and better diffusion of Glc within the 3-D network.

2.4 Conclusion

This chapter presented controlled synthesis of vertically aligned MWCNTs arrays by CVD and further showed two different synthetic routes to modify the as-synthesized MWCNTs with Cu or $CoOx{\cdot}nH_2O$ nanoparticles by electrochemical deposition. Both Cu-MWCNTs and CoOx·nH2O-MWCNTs amperometric sensors can selectively and sensitively detect Glc in a certain dynamic working range under the many interfering species with satisfactory sensitivities, low detection limits, fast responses and acceptable long-term stability and selectivity for Glc. The relatively low fabrication cost, the time-saving and easy preparation and good reproducibility of the sensing materials endow the sensors with the potential to be developed for routine Glc analysis such as human blood samples.

Chapter 3: Enzyme-free sensing of Glc with a portable microfluidic device using graphene hybrid materials*

3.1 Introduction

The risks of renal, retinal, and neural complications are directly associated with Glc levels in body fluids of diabetic patients (Rohlfing et al. 2002). Thus, sensing for Glc in body fluids has been actively pursued, especially based on different electrochemical mechanisms, with (Luo et al. 2010; Luo et al. 2004; Yang et al. 2011b; Yang et al. 2011f) or without(Lu et al. 2009; Mu et al. 2011; Nie et al. 2011; Toghill et al. 2010a) using the enzyme glucose oxidase (GO_x). Typically, GO_x catalyzes oxidation of Glc into gluconolactone in the presence of dissolved O_2, with O_2 being reduced to hydrogen peroxide (H_2O_2). Therefore, electrochemical detection of Glc is accomplished by monitoring either O_2 consumption (Yang et al. 2011b) or H_2O_2 production (Luo et al. 2004). With the availability of nanoscale materials, another approach has been developed based on direct electrochemistry of GO_x (Liu et al. 2011). Although GO_x is relatively more stable than other enzymes, use of GO_x-based sensors is limited by relatively high cost, inherent instability, complicated immobilization procedures, and certain critical operational and storage conditions (e.g., temperature, pH, humidity, ionic strength). Therefore GO_x-based Glc sensing is mostly used for real-time monitoring in fermentation processes or *in vivo* human tests, where sterilization is needed (Mu et al. 2011). In contrast, sensors for enzyme-free Glc detection are based on metal (Toghill et al. 2010a), metal alloys(Wang et al. 2008b), metal oxides(Mu et al. 2011) as inorganic electrocatalysts using carbon materials (e.g., carbon nanotubes (CNTs) and graphene) (Nie et al. 2011) as scaffolds. The enzyme-free sensors, despite the need for them to be operated in alkaline conditions, perform better than the enzyme-based sensors and exhibit improved sensitivity, stability, response time, and detection limit; they are also less expensive (Mu et al. 2011). Many researchers have reported superior sensing performance of enzyme-free Ni-based (i.e., Ni, NiO, $Ni(OH)_2$) sensors due to the formation of strong oxidizing NiO(OH) in alkaline conditions (Ai et al. 2008; Lu et al. 2009; Mu et al. 2011);Ni is also abundantly available, making it an inexpensive electrocatalyst for Glc sensing.

Chitosan (CS) is a linear aminopolysaccharide derived from partial deacetylation of chitin. It is a nontoxic cationic biopolymer, and exhibits good biocompatibility, biodegradability, adhesiveness, and film-forming ability (Yang et al. 2010c); it can also serve as antifouling protective coating (Bulwan M. 2011). CS has been extensively used in integrative biomaterials

*This work has been published: (Yang et al. 2013)

and immobilization matrices to assist in the fabrication of sensors and lab-on-a-chip devices. CS films can be easily prepared by drop-casting(Han et al. 2010), spin-coating(Jawaheer et al. 2003), electrodeposition (Wu et al. 2005), and nano-imprinting(Park et al. 2007). Among these approaches, electrodeposition, which takes advantage of the pH-dependent solubility of the material (Wu et al. 2005), is the most controllable. CS is well-known to electrodeposit in response to high localized pH values (>5.0) at cathode surface and has been widely used to mediate co-depositions of nanoparticles (NPs), enzymes, and carbon materials. Zeng et al. fabricated an enzymatic Glc sensor by co-electrodepositing CS-IL-GO_x-AuNPs via a two-step approach(Zeng et al. 2009a). Yang et al. constructed a nitrite sensor by one-step electrodeposition of CS-CNTs-CuNPs under constant cathodic potential (Yang et al. 2010c). Wan et al. described an impedimetric immunosensor for label-free bacteria detection by controllable electrodeposition of CS and RGO (Wan et al. 2011); however, this approach requires complicated fabrication procedures, because RGO is first reduced by hydrazine before deposition.

Graphene obtained from GO is readily and inexpensively available(Segal 2009). Electrochemical reduction of GO is simple, rapid, green, and effective (Yang et al. 2011b), and it prevents the use of any toxic or corrosive reducing reagents or stabilizers that might damage its electronic properties. The nearly insulating GO becomes highly conducting RGO when the undesired oxygen species are eliminated by electrochemical reduction at pH 5.0 (Yang et al. 2011b). It has been reported that GO, along with AuNPs, can be directly electrodeposited onto electrode surface and electrochemically reduced *in situ* owing to the different solubilities of GO and RGO (Liu et al. 2011). Since all of GO, CS, and metal NPs (e.g., NiNPs) can be electrodeposited at pH 5 under cathodic potentials and they can form nanocomposite precursors by electrostatic and hydrophobic interactions (**Scheme 3.1**), the nanocomposites can be efficiently synthesized on the electrode surface. There are three roles of GO in this study: it helps to form the self-assembled precursor nancomposite as a scaffold; its reduced form RGO endows hydrophobicity for deposition from the aqueous solution; RGO also provides much fast electron transfer capability for redox reactions.

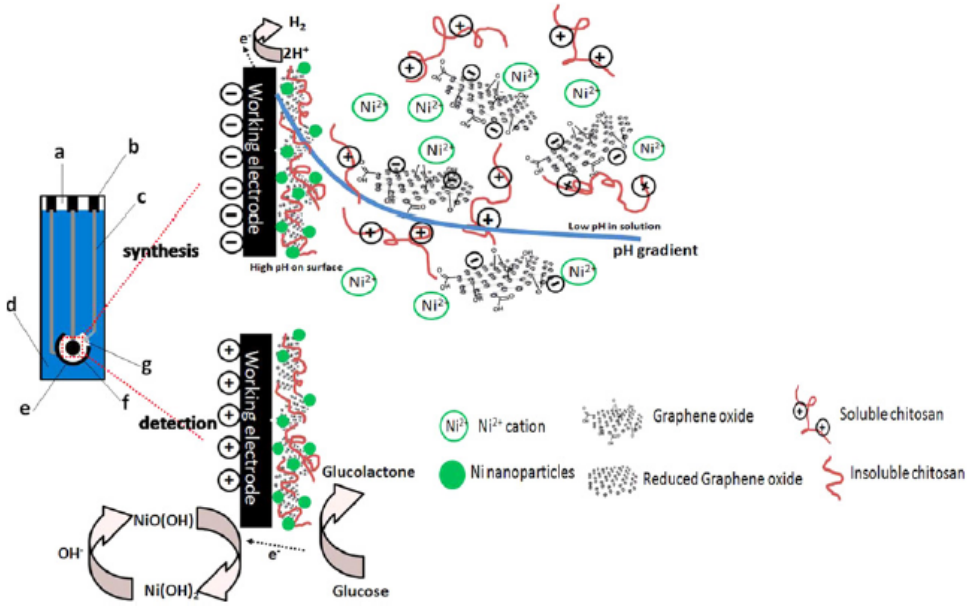

Scheme 3.1: Schematic diagram of the electrodeposition processes of CS-RGO-NiNPs on SPE surface and its Glc detection mechanism. (a) polypropylene, (b) carbon electrical contacts, (c) conductive paths, (d) Insulting dielectric, (e) carbon counter electrode, (f) carbon working electrode, (g) Ag/AgCl pellet reference electrode. Synthesis (upper part of the figure): the synthesis reaction begins with the formation of nanocomposite precursors by electrostatic and hydrophobic interactions between negatively charged GO and positively charged Ni^{2+} and CS chains. With cathodic potential applied, protons in the acid solution around the electrode surface are consumed, causing relatively high localized pH. As a result, CS chains in the nanocomposite precursors near the electrode become insoluble and deposited from bulk solution together with GO and Ni^{2+}. On the electrode surface, GO and Ni^{2+} are *in situ* reduced into RGO and NiNPs and deposited simultaneously with the deposition of CS. Detection (lower part of the figure): the detection reaction under applied anodic constant potentials starts with oxidation of Ni(0) into Ni(II) species such as $Ni(OH)_2$ and NiO. These Ni(II) species are then further oxidized into strongly oxidizing Ni(III) species as NiO(OH) which electrochemically catalyzes the oxidation of glucose into gluconolactone liberating two hydrogen atoms. Meanwhile, NiO(OH) itself is reduced back into Ni(II) species.

The motivation for this study is to fabricate an inexpensive and enzyme-free miniaturized lab-on-chip device for routine Glc measurement by end users. Therefore, in our design we sought to combine the high sensitivity, rapidity, simplicity, and low detection limit advantages of electrochemical sensing; small sample volume, easy manual sample injection, and miniaturization advantages of microfluidics; and low cost and replaceability advantages of screen-printed electrodes (SPEs). Few reports on similar investigations include that of Joo et al., who reported an enzyme-free electrochemical Glc sensing using nanoporous Pt in a microfluidic system driven by electroosmotic flow(Joo et al. 2007) and that of Vlandas et al., who fabricated a single-wall carbon nanotube sensor in microfluidic channels for enzyme-free sensing of sugar (Vlandas et al. 2010).

We have developed a portable electrochemical microfluidic system housing commercial SPEs for real-time measurement of Glc. The SPEs were modified by a simple CS-mediated one-step co-electrodeposition of self-assembled CS, GO and NiNPs nanocomposite precursors at pH 5, while GO (Yang et al. 2011b) was electrochemically reduced *in situ* upon deposition without pre- or post-reductions necessary. The electrodeposition and reduction reactions of both GO and Ni precursor occurred simultaneously (Liu et al. 2011) with CS deposition. The resulting CS-RGO-NiNPs nanocomposite facilitated electron transfers and endowed high electrocatalytic activity for non-enzymatic Glc sensing. The as-fabricated sensor exhibited high sensitivity, good stability and selectivity towards Glc, with a wide linear range covering Glc levels in physiological fluids of normal individuals. Therefore, it has the potential to be further developed into a pocket-size, enzyme-free, point-of-care analytical device for routine Glc monitoring.

3.2 Experimental

3.2.1 Chemicals and reagents

Graphite powder and D(+)-glucose anhydrous were purchased from Sinopharm Chemical Reagent Co.. Dopamine hydrochloride (DA), uric acid (UA) and L-ascorbic acid (AA) were purchased from Acros Organics and nickel (II) sulfate hexahydrate ($NiSO_4 \cdot 6H_2O$) were obtained from Alfa Aesar. High molecular weight CS (from crab shells) was purchased from Sigma-Aldrich Chemicals. All other reagents were of analytical grade and used as received without further purification. Doubly distilled Milli-Q water (ddH_2O) (>18.2 MΩ) was used for all experiments and high purity N_2 was used for deaeration where needed. SPEs were purchased from Zensor featuring graphitic carbon working (with geometric area of ~7.07 mm^2) and counter electrodes and Ag/AgCl pellet reference electrode (**Scheme 3.1**). 0.1 M NaOH was used as the supporting electrolyte for Glc detection throughout, unless otherwise stated. =

3.2.2 Instrumentation

Scanning electron microscopy (SEM) and energy dispersive X-ray spectroscopy (EDS) were conducted using EDS-integrated LEO 1530 Gemini FESEM (Carl Zeiss, USA) for characterizing surface morphology and elemental composition of the sample. Particle size distribution was determined using Image-ProPlus software. Attenuated total reflectance-Fourier transform infrared spectroscopy (ATR-FTIR) was conducted with PerkinElmer Spectrum 100 (PerkinElmer, MA, USA). Cyclic voltammetry (CV), chronoamperometry and electrochemical impedance

spectroscopy (EIS) were performed on a CHI 660D Electrochemical Analyzer (CH Instruments, TX, USA) at ambient temperature (25±1°C) using three-electrode configuration. EIS was carried out in a solution containing 0.01/0.01 M $[Fe(CN)_6]^{4-/3-}$ and 1.0 M KCl electrolyte in the frequency range of 0.1-10^5Hz. HPLC analysis was performed using Dionex ICS-3000 HPLC system (Dionex Corporation, MA, USA) equipped with Carbopac™ PA1 guard column at 20°C and an electrochemical detector using Au, Ti, and pH-Ag/AgCl as working, counter, and reference electrodes, respectively. Eluent was supplied at a rate of 0.7 $mL\cdot min^{-1}$ as follows: water for 25 min, the water plus 0.1 M NaOH at 3:7 (v/v) for 10 min, followed by water for 10 min. To achieve stable baseline and better sensitivity, 0.5 M NaOH was used at 0.3 $mL\cdot min^{-1}$ as post-column eluent. Starting at around 5.6-5.8 min Glc was eluted, with the retention peak centered at around 6.0-6.5min varying by standards and samples. Glc concentrations from HPLC-amperometry were calculated by integrating the area under designated peaks and standard calibration curves. Error bars indicate triplicate measurements unless otherwise noted.

3.2.3 Fabrication of CS-RGO-NiNPs modified working electrodes

Well-exfoliated GO was synthesized using a modified Hummer's method (Yang et al. 2011b; Yang et al. 2012a). Concentrated H_2SO_4 and $KMnO_4$ were used to gain pre-oxidized graphite and the product was then re-oxidized to GO by H_2O_2. After sonication, delamination of GO sheets were achieved and stable exfoliated GO aqueous dispersion can be obtained due to negative electrostatic repulsion from ionization of carboxyl and phenolic hydroxyl groups on GO sheets(Liu et al. 2011). CS solution was prepared by adding CS platelets to water and gradually adjusting the pH to ~3.0 with HCl (Luo et al. 2004; Wu et al. 2005). The solution was vortexed for 10 min and sonicated for 30 min, before it was filtered to remove any insoluble contents with pH adjusted to 5.0 using NaOH. GO and $NiSO_4$ were added to have final concentrations of 1 $mg\cdot mL^{-1}$ GO, 3 mM $NiSO_4$and 0.4% CS with final pH value maintained at 5.0. After being mixed under stirring for 1 h at room temperature, the solution was further sonicated to be homogenous and stable and was then deaerated by purging N_2 for 15 min. For electrodeposition, SPE was immersed in the above suspension horizontally and multiple cathodic CV cycling was conducted in the potential range of 0.0 V to -1.5 V at a scan rate of 50 $mV\cdot s^{-1}$ for 40 cycles. After deposition, the CS-RGO-NiNPsmodified SPE was gently rinsed with water and dried at room temperature. RGO- and CS-RGO modified SPEs were also prepared similarly using corresponding deposition solutions for comparison. Before any Glc measurement, CS-RGO-NiNPs modified SPEs

were tested in 0.1 M NaOH by 40 consecutive CV cycles from 0.0 V to +0.8 V at 0.1 Vs $^{-1}$ to reach the steady state until almost no obvious change in peak current (**Fig. 3.1**). This pretreatment has been widely used to facilitate the formation of Ni oxyhydroxide for stable Ni-based enzyme-free Glc sensing (Lu et al. 2009; Nie et al. 2011). The deposition solution was freshly prepared for every 2 to 3 electrodes, and prior to each deposition pH 5.0 was maintained. Electrodes were stored in a Petri dish at room temperature when not in use.

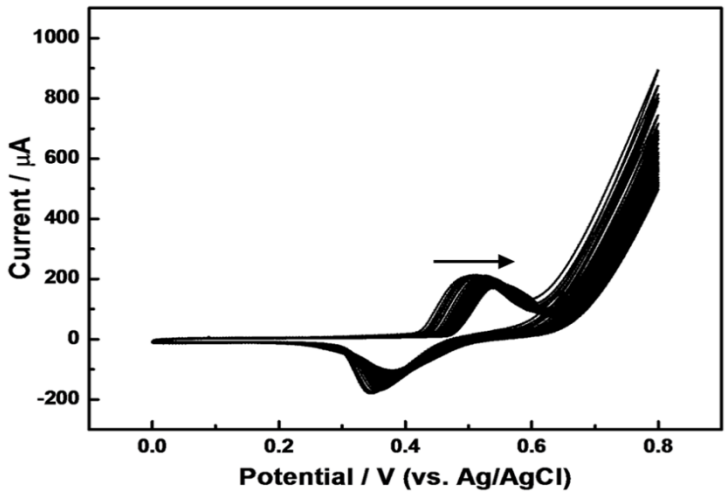

Fig. 3.1: Repetitive CVs of CS-RGO-NiNPs modified SPEs in 0.1 M NaOH. Scan range: 0.0 to +0.8 V. Scan rate: 0.1 V·s^{-1}. The arrow indicates progression of cycles.

3.2.4 Fabrication of the portable microfluidic device with replaceable SPEs

The mold for PDMS chamber and device holder was prepared using acrylonitrile butadiene styrene (ABS) plastic. The 10:1 mixture of Sylgard 184 (Dow Corning Co.) was poured on top of the mold and peeled off after curing for three days at room temperature. Two small holes were drilled in the PDMS chamber to accept inlet and outlet tubes (760 µm OD, 250 µm ID, Cole-Parmer Co.). The detailed device setup is shown in **Scheme 3.2**. The PDMS chamber was placed on top of the sensor and fixed by the ABS holder. The microfluidic chamber embedded in PDMS chamber was carefully aligned with the active area on the modified SPE sensor. One of the two holders has square or circular shape through the hole so that the inlet and outlet tubes can be connected to the PDMS chamber. The whole device stack was firmly held by Quick Grip® Micro Bar Clamp and Spreader (American Tool Inc.) to prevent any possible leaking from the chamber. The inlet tube for sample injection was connected to a 10-mL microsyringe, which is available locally. The tube can also be connected to a pump or a micropipettor, if needed. Samples could be simply injected manually at a comparatively slow and steady rate or by an adjustable syringe

pump. Based on the dimensions of the PDMS chamber (7 mm diameter, 0.2 mm height), the calculated sample volume required for detection using this device is 7.7µL. After measurements, the used SPE can be easily removed from the analytical device and replaced with freshly prepared SPEs as necessary.

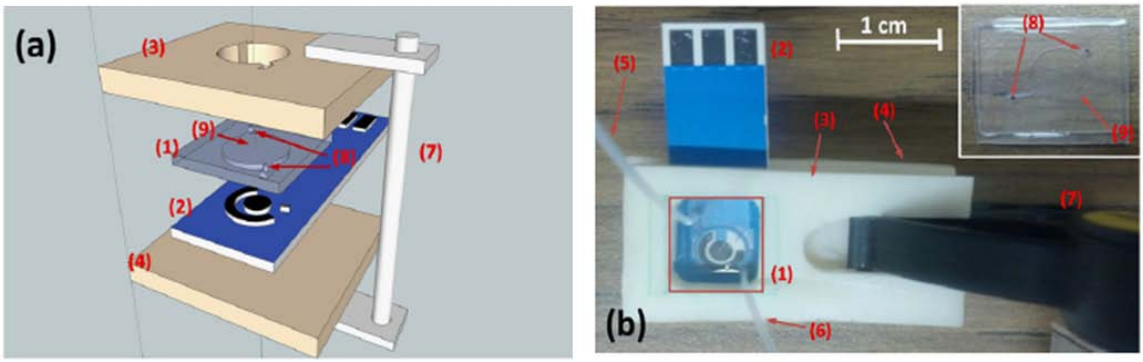

Scheme 3.2: (a) Scheme of the device stack setup. **(b)** Photograph of the as-fabricated microfluidic electrochemical device for sensing Glc. (1) PDMS chamber (inset in (**b**) shows an enlarged view) (2) CS-RGO-NiNPs modified SPE (3) top piece of plastic device holder (4) bottom piece of plastic device holder (5) outlet tubing (6) inlet tubing connected to a sample injector (syringe or pump) (7) Micro bar clamp/spreader (8) holes for connecting inlet and outlet tubes (9) circular chamber fit to the sensing area.

3.3 Results and discussion

3.3.1 *Characterizations of CS-RGO-NiNPs*

SEM image of unmodified and CS-RGO-NiNPs modified SPEs are shown in **Fig. 3.2a and f** respectively. The pristine carbon SPE showed a typical graphite structure with high dispersed carbon particles in blurred and irregular shapes and there are no obvious wrinkled structures or NPs observed (**Fig. 3.2f**). As for CS-RGO-NiNPs, a rough webbed surface with flake-like graphite sheet particles can be observed with many exposed edge-plane sites/defects, which usually serve as origins of electron transfers at the electrode (Kadara et al. 2009b). Fairly dense network of NiNPs had been homogenously deposited onto the pristine graphite sheets. The NPs are mostly spherical and fairly uniform in size (31.7±4.7 nm) (**Fig. 3.2b**), and tended to be clustered and interconnected throughout the electrode surface. CS chains play a vital part in the growth and assembly of clusters of NPs, which are entrapped in CS network or coated with CS(Potara et al. 2012). Typical wrinkled graphene structure is clearly seen on graphite stack substrate under higher magnification, indicating the presence of flexible and thin graphene sheets (**Fig. 3.3a inset**).

A possible deposition process of CS-RGO-NiNPs nanocomposites is as follows. In the deposition solution, positively charged CS and Ni^{2+}cations interact by chelating (Adewuyi et al. 2011), while negatively charged GO sheets can form composites with both CS and Ni^{2+} via electrostatic interactions in the solution. Hydrophobic moieties in CS such as acetyl groups and glucosidic rings might interact with the hydrophobic part of GO basal planes via partially hydrophobic interactions. As a result, self-assembled conjugates of CS-GO-Ni^{2+} are formed. With applied cathodic potentials leading to electrode polarization, the proton in the acidic solution around the electrode surface is consumed and local pH is increased, forming a localized pH gradient (Wu et al. 2005). CS chains in the nanocomposite precursors near electrode surface become insoluble due to higher pH, whereas, CS chains in the bulk solution (pH 5.0) remain soluble (**Scheme 3.1**). Therefore, as CS chains are deposited onto the electrode surface, GO sheets and NiNPs are co-deposited into CS matrices at the same time. Moreover, GO sheets (Liu et al. 2011) and NiNPs (Toghill et al. 2010a) might also be deposited at cathodic potentials under these conditions. With continued cathodic potential sweeping, GO sheets are electrochemically reduced *in situ* efficiently and Ni cations are simultaneously reduced, with NPs nucleated and entrapped in CS as clusters. The reduction product RGO becomes more hydrophobic than GO because oxygen species are eliminated, and thus gets deposited onto the electrode surface. The nanocomposites then form and progressively link together, and RGO with its high conductivity affords effective preferential nucleation sites for NiNPs enhancing the electrodeposition. NiNPs are formed owing to the highly supersaturated solution of anionic species (SO_4^{2-}, GO, Cl^-), well-controlled production on time scale (i.e., potential sweeping range and cycles) and possibly the existence of hydrogen evolution under low pH which leads to the formation of NPs without faceted morphology (Nasirpouri et al. 2011). The assumptions are further supported by the voltammetric behaviors during the synthesis in stable dispersions (**Fig. 3.4**). A typical crossing of CV curve (loop) can be seen in the reverse scan, representing the characteristics of electrodeposition processes of Ni and carbon materials(Martis et al. 2010). As the synthesis progresses, the cathodic current intensity decreases from the 1^{st} to the 13^{th} cycles and H^+ is reduced and thus CS is deposited leading to reduced conductivity and hence decreased current. During this process, NiNPs are yet completely nucleated and decrease in cathodic current might be also attributed to the *in situ* electrochemical reduction of GO, as we reported previously(Yang et al. 2012a). However, the current surprisingly increases from the 14^{th} cycle on,

which is probably associated with the successful synthesis of RGO and NiNPs since the nanocomposite as a whole has high conductivity.

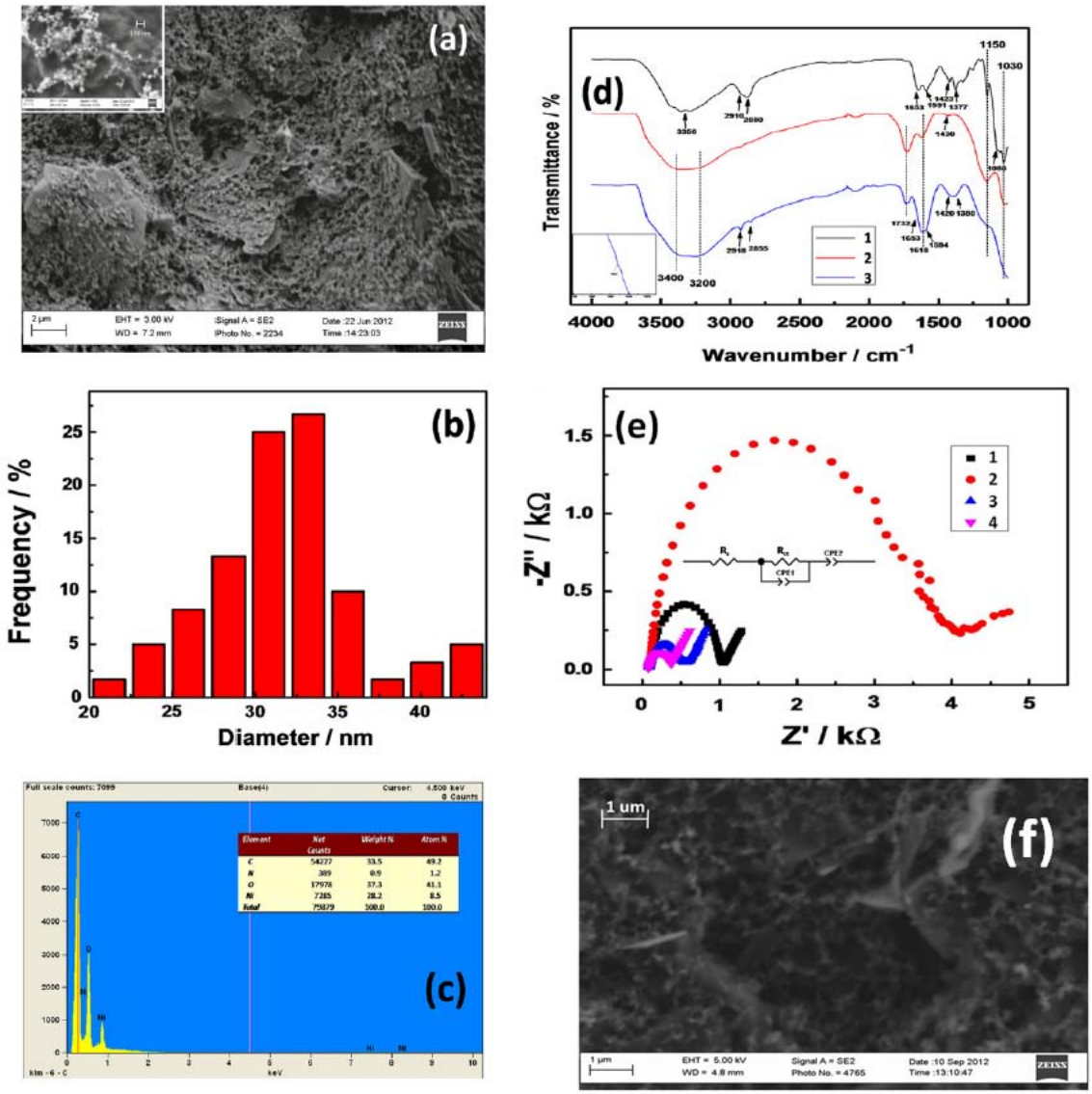

Fig. 3.2: (a) SEM images of CS-RGO-NiNPs electrode. Inset shows higher magnification. **(b)** Particle size distribution of NiNPs. **(c)** EDS spectra of CS-RGO-NiNPs. Inset shows corresponding quantitative analyses. **(d)** ATR-FTIR spectra of pristine CS (1), GO (2) and electrodeposited CS-RGO (3). Inset shows magnification of weak band of (3) at 1653 cm^{-1}. (e) EIS of bare (1), CS (2), CS-RGO (3) and CS-RGO-NiNPs (4) modified SPEs. Inset shows the equivalent circuit for CS-RGO-NiNPs modified SPEs. R_s: solutions resistance; R_{ct}: charge transfer resistance; CPE: constant phase element. (f) SEM image of unmodified carbon SPEs.

Elemental composition of CS-RGO-NiNPs was analyzed by simultaneous EDS (**Fig. 3.2c**). Strong signature peaks of C, O, and Ni were observed, along with a weak peak indicating N. Carbon came from both the substrate and electrochemically deposited and reduced GO sheets.

Oxygen species originate from the substrate, deposited CS, electrochemically unreduced oxygen species on RGO (Yang et al. 2012a), and possibly oxide or hydroxide Ni species during deposition (Toghill et al. 2010a). The presence of 1.2 and 8.5 atomic percentages of N and Ni, respectively manifested the successful electrochemical deposition of CS and NiNPs.

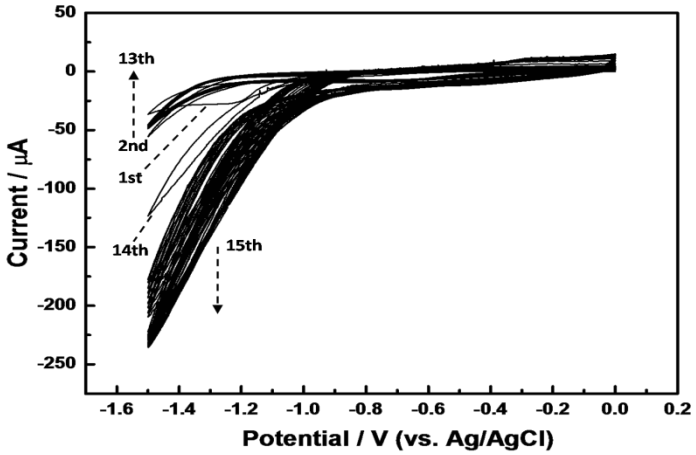

Fig. 3.3: Repetitive CV profiles during the synthesis from a CS-GO-Ni^{2+} nanocomposite precursor solution. Scan range: 0.0 to -1.5 V. Scan rate: 50 mV^{-1}. The number of cycles is marked and arrows indicate progression of cycles.

ATR-FTIR transmittance spectra of pristine CS, GO, and CS-RGO are shown in **Fig. 3.2d.** As seen in CS (curve 1),the characteristic peaks of the following CS functionalities are observed: a broad and intense band (3300-3450 cm^{-1}) centered around 3350 cm^{-1} fromN-H stretching vibrations in amide or amine groups and overlapped O-H stretching vibration in hydroxyl group (Wei and Qian 2008); both methyl characteristic bands at 2910 and 2880 cm^{-1} from strong and moderate C-H stretching vibration in acetylated CS; three characteristic amide bands at 1653 cm^{-1} from C=O stretching vibration (chitin residues), 1591 $cm^{-1}$from N-H deformation vibration in amine group, 1423 cm^{-1} from C-H deformation vibration; bands of saccharine structures at 1377 cm^{-1} from C-OH stretching vibration, 1150, 1080 and 1030 cm^{-1} from symmetric and asymmetric C-O stretching vibrations in ether or ester groups. These results are similar to those in literature (Han et al. 2010; Wan et al. 2011; Wei and Qian 2008). The spectrum of GO manifested a number of oxygen functionalities, as we have reported previously (Yang et al. 2012a): a broad and strong band at 3400 cm^{-1} from O-H stretching vibration in intercalated water, an overlapped broad band at 3200 cm^{-1} of O-H coupling stretching vibration in carboxyl group, a sharp peak at 1732 cm^{-1} from C=O stretching vibration in carbonyl group, C=C band at 1620 cm^{-1} from skeletal vibrations of unoxidized graphitic domains, a weak broad band at 1430 cm^{-1} from O-H

deformation vibration in carboxyl group, a strong band at 1150 cm^{-1} from C-O stretching in ether or ester groups and a shoulder band at 1030 cm^{-1} of C-O stretching vibration in epoxy or alkoxy groups. In the electrodeposited CS-RGO, the large broad band of N-H and partially overlapped O-H stretching from 3200-3450 cm^{-1} remains and unreduced oxygen species in GO might also contribute to this band(Chen et al. 2011). Dramatically weaker and shifted methyl peaks are still present at 2918 and 2855 cm^{-1} due to hydrolysis of acetyl groups during electrodeposition (Wan et al. 2011). A very weak band (see inset) at 1653 cm^{-1} and slightly shifted bands at 1594 cm^{-1}, 1420 and 1380 $cm^{-1}$are indicative of amide groups from CS. The band shifts might be attributed to chemical bonding between CS and RGO, such as hydrogen bonding or interactions of active groups such as carboxyl, hydroxyl and amine groups (Wan et al. 2011). Meanwhile, the intensities of C=O O stretching vibration at 1732 cm^{-1} and C-O stretching vibration at 1150 and 1030 cm^{-1} decreased drastically whereas the intensity of C=C skeletal vibration band at 1620 cm^{-1} in CS-RGO is much stronger than GO, demonstrating successful electrochemical reduction and RGO has high purity. These results suggest that CS and GO have been successfully synthesized on the electrode surface by co-deposition and GO has been electrochemically reduced *in situ*.

EIS is a useful tool to study the electron transfer characteristics in the electrode-electrolyte interface and to track electrode surface modifications as presented in Nyquist complex-plane plots of differently-modified electrodes in the presence of equimolar $[Fe(CN)_6]^{4-/3-}$ redox probes (**Fig. 3.2e**). In typical spectra, a semicircle in the higher frequency region corresponds to charge transfer-limiting process with its effective diameter of semicircles equal to Faradic charge transfer resistance (R_{ct}) responsible for electron transfer kinetics of redox reactions at the interface, while a straight line in the lower frequency represents the diffusion-limiting process in the electrochemical process. The equivalent circuit model (**Fig. 3.2e inset)** is comprised of the series of solution resistance (R_s), the parallel combination of R_{ct} and a constant phase element (CPE), and another CPE. The fitting result with experimental data is shown in **Fig. 3.4**. CPE is defined as CPE-T and CPE-P. When CPE-P is close to 0, CPE can be regarded as an ideal resistor; when CPE-P is close to 1, it represents an ideal capacitor; when CPE is close to 0.5, CPE is associated with the diffusion process and termed as Warburg impedance. CPE is used instead of a pure capacitor/resistor to compensate for non-ideal conditions at the interface, reflecting the inhomogeneity and defects on the surface (Maalouf et al. 2007). The fit values for each element is listed in **Table 3.1**. CPE1 in this study acts more like a capacitor whereas CPE2 can be considered for Warburg diffusion. In the meantime, compared to the unmodified electrode

(curve 1, R_{ct}=900Ω), the electrode modified by CS deposition yielded a much larger semicircle (curve 2, R_{ct}=3447Ω) implying large resistance to the redox probe in the electrolyte solution. This might be ascribed to the diffusion of redox probes and interfacial electron transfers towards electrode surface that are hindered by CS. CS-RGO modified electrode (curve 3) has a significantly smaller R_{ct} (416Ω) than the CS-modified electrode, due to greatly enhanced electron transfers within RGO interpenetrating network (Yang et al. 2011b). The unreduced GO behaves nearly as an insulator and prohibited electrochemical properties owing to the presence of excessive oxygen species (Chen et al. 2011), here it confirms successful *in situ* elimination of electrochemically unstable oxygen species during deposition, which facilitates electron transfers. This result is also well-supported by the gradually decreasing cathodic current in CV profiles during initial deposition (**Fig. 3.3**), similar to those previously reported (Liu et al. 2011; Yang et al. 2011b). R_{ct} of CS-RGO-NiNPs (273Ω) further decreased with modification of Ni metal NPs, suggesting NiNPs are beneficial for electron transfers by providing favorable conduction pathways or probably by synergistic effects in the nanocomposites. Therefore, CS-RGO-NiNPs can dramatically improve the electron transfer efficiency at the electrolyte-electrode surface.

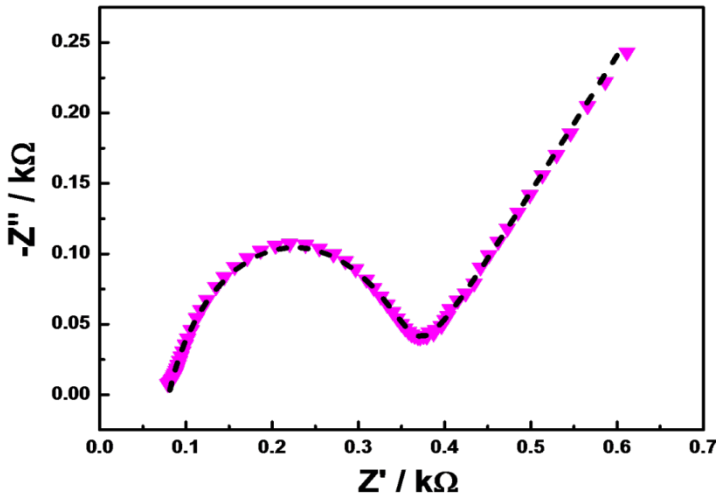

Fig. 3.4: EIS of CS-RGO-NiNPs modified SPEs (magnification of **Fig. 3.3e**). The dotted line indicates the result of equivalent circuit fitting (**Fig. 3.3e inset**).

Table 3.1: Fitting values of different equivalent circuit elements by Zplot/Zview for different SPEs (errors are shown in % as in their following parenthesis).

Electrodes	Rs (Ω)	Rct(Ω)	CPE1-T (μF)	CPE1-P	CPE2-T (mF)	CPE2-P
Bare	100.2 (0.44%)	899.9 (0.49%)	0.46 (2.71%)	0.94 (0.32%)	3.34 (2.07%)	0.45 (3.18%)
CS	94.5	3447.0	0.45	0.94	1.01	0.36

	(3.02%)	(1.17%)	(5.32%)	(0.76%)	(6.05%)	(5.35%)
CS-RGO	78.9 (0.69%)	416.0 (1.00%)	1.98 (4.83%)	0.82 (0.66%)	2.84 (1.43%)	0.37 (2.57%)
CS-RGO-NiNPs	80.2 (2.3E-13%)	273.2 (4.89E-13%)	8.36 (2.34E-12%)	0.80 (3.60E-13%)	3.56 (6.15E-13%)	0.49 (9.31E-13%)

3.3.2 *Electrochemical properties and electrocatalytic activities towards Glc at CS-RGO-NiNPs*

The electrocatalytic activity of CS-RGO-NiNPs towards Glc was studied by CV in 0.1 M NaOH (**Fig. 3.5a**). In the absence of Glc, both bare (curve 3) and CS-RGO modified (curve 5) electrodes displayed a rather broad and unobvious anodic peak around +0.45 V (**Fig. 3.5a inset**) which might come from electrochemical behavior of quinone/hydroquinone groups typically present in carbon material. After the addition of 5 mM Glc, there was only a negligible increase in current at the bare electrode (curve 4) while at CS-RGO electrode, rather than an increase, a tiny decrease in current was surprisingly observed (curve 6), possibly caused by electrochemical reduction of the remaining unreduced GO. In contrast, a pair of well-defined redox peaks appeared at CS-RGO-NiNPs electrode in the absence of Glc, with the cathodic and anodic peaks at +0.35 V and +0.50 V respectively corresponding to Ni(III)/(II) redox couple as described in the literature (Lu et al. 2009; Nie et al. 2011). This typical nonsymmetrical face wave of Ni in 0.1 M NaOH is associated with the irreversible process of oxidation-reduction (Zhao et al. 2007a). Ni(0) is firstly oxidized into Ni(II) to form NiO and/or $Ni(OH)_2$ (Eq. 1) at potential less than -600 mV and Ni(II) species are further oxidized into Ni(III) as NiO(OH) (Eq. 2 and 3), as described below (Lu et al. 2009; Nie et al. 2011; Zhao et al. 2007a):

$$Ni + 2OH^- - 2e^- \rightarrow Ni(OH)_2 \rightleftharpoons NiO + H_2O \quad (1)$$

$$NiO + OH^- - e^- \rightarrow NiO(OH) \quad (2)$$

or

$$Ni(OH)_2 + OH^- - e^- \rightarrow NiO(OH) + H_2O \quad (3)$$

Upon adding 3 mM Glc, an increase in anodic peak current and a decrease in cathodic current appeared, suggesting CS-RGO-NiNPs can mediate Glc oxidation. Considering the poor electrocatalytic activities of CS-RGO and bare electrodes against Glc, NiNPs in the nanocomposites are responsible as an enzyme mimicking catalyst for Glc oxidation with a possible mechanism directed by Ni(III) with two hydrogen liberated (**Scheme 3.1**), as below (Eq. 4)[6, 7, 20]:

$$NiO(OH) + \text{glucose} \rightarrow Ni(OH)_2 + \text{glucolactone} \qquad (4)$$

In this reaction at anodic potentials, strongly oxidizing Ni(III) species oxidize glucose into glucolactone and themselves are reduced into Ni(II) species. Therefore, the concentration of Ni(III) decreases while that of Ni(II) increases, causing an increase in anodic peak current and a decrease in cathodic peak current[6]. The anodic peak potential shifted to a more positive +0.60 V, possibly attributed to the diffusion-limited process of Glc at the electrode surface (Nie et al. 2011). Since the peak potential to simultaneously produce Ni(III) species and to oxidize Glc at CS-RGO-NiNPs electrode is around +0.60 V (curve 2), this potential was selected as the detection potential. Also noticeably, the background current of CS-RGO-NiNPs electrode is much larger than those of bare and CS-RGO electrodes, indicating the electrode is more conductive and favorable for electron transfers, consistent with EIS data.

The voltammetric behaviors of CS-RGO-NiNPs electrode were investigated in 0.1 M NaOH at different scan rates (**Fig. 3.5b**). As the scan rate increased from 0.02 to 0.4 $V \cdot s^{-1}$, both anodic and cathodic peak currents increased in proportion to the square root of scan rates. Moreover, the anodic peak potential shifted more positively while the cathodic potential shifted more negatively with increasing scan rates, thus generating a larger peak-to-peak potential separation. These results are evidence of nucleation of NiO(OH) followed by an increase in active sites in both Ni(III) and Ni(II) species (Sun et al. 2012). A linear dependence of peak currents on the square root of scan rates (**Fig. 3.5b inset**) can be established for both anodic and cathodic peak currents (R=0.999), signifying the diffusion-controlled electrochemical kinetics.

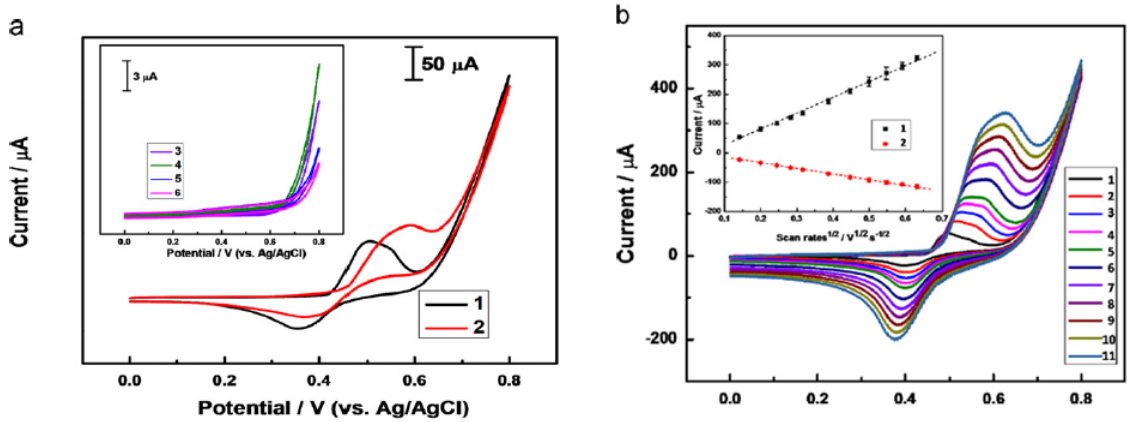

Fig. 3.5: (a) CVs of CS-RGO-NiNPs modified SPE in 0.1 M NaOH in the absence (1) and presence (2) of 3 mM Glc. Inset shows CVs of unmodified (3 and 4) and CS-RGO (5 and 6) modified SPEs in 0.1 M NaOH in the absence (3 and 5) or presence (4 and 6) of 5 mM Glc. Scanning from 0.0 to +0.8 V at 0.1 V·s -1. (b) CVs of CS-RGO-NiNPs in 0.1 M NaOH at different scan rates of 0.02, 0.04, 0.06, 0.08, 0.1, 0.15, 0.2, 0.25, 0.3,

0.35 and 0.4 V·s-1 (inner to outer). Inset shows anodic and cathodic peak currents as a function of square root of scan rates.

3.3.3 *Amperometric sensing of CS-RGO-NiNPs electrode towards Glc*

The amperometric responses at CS-RGO-NiNPs electrode in 0.1 M NaOH at an applied potential of +0.60 V were evaluated in **Fig. 3.6a** by dropwise successive addition of Glc in concentrations of 0.2mM (curve 2) and 1 mM (curve 1). Consistent with CVs (**Fig. 3.5a**), CS-RGO-NiNPs electrode yielded an overwhelmingly larger current response than CS-RGO electrode (curve 3). Apparent stair-like stepwise increases in current were achieved with each addition of Glc, and steady-state currents were obtained in seconds, confirming high sensitivity and fast response of CS-RGO-NiNPs towards Glc. The superior performance in Glc sensing might be owing to the high conductivity and electrocatalytic activity of CS-RGO-NiNPs that offer low resistance pathways for faster electron transfers. A linear relationship was found between the current response and Glc concentration (I(μA)=22.48*C (mM) +15.29, R=0.994) from 0.2 to 9.0 mM and the two calibration curves at different concentrations almost overlapped, indicating good reproducibility and stability (**Fig. 3.6b**). The sensitivity was calculated to be 318.4 μA $mM^{-1}\cdot cm^{-2}$,and dynamic linear working range of up to 9.0 mM of Glc. The detection limit was determined to be 4.1 μM at signal/noise=3. The sensing performance of the as-prepared CS-RGO-NiNPs SPEs is compared with other reported Ni-based enzymatic or enzymeless Glc sensors in **Table 3.2**. Our sensor boasts almost the highest sensitivity, widest linear range, and excellent detection limit. Since the normal Glc level for humans is typically 0.1 to 0.8 mM in urine and 3.5 to 5.3 mM in whole blood (Hones J. 2008), the wide linear range of CS-RGO-NiNPs is capable of measuring Glc at normal physiological levels either in urine or blood without diluting the samples. The Glc levels in diabetic patients are higher, and measurements may be made with appropriate dilutions.

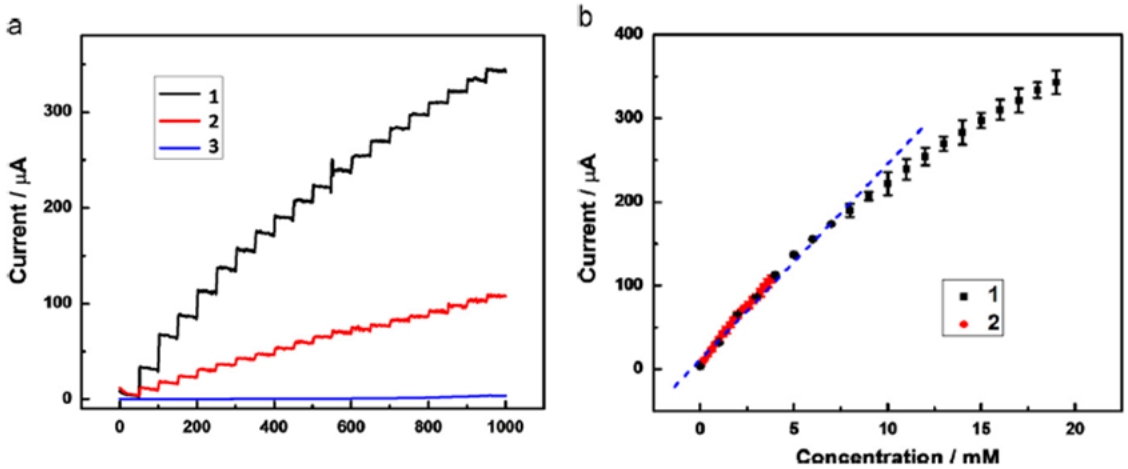

Fig. 3.6: (a) Amperometric responses of CS-RGO-NiNPs (1 and 2) and CS-RGO (3) SPEs in 0.1 M NaOH with stepwise addition of 1 (1 and 3) and 0.2 mM Glc (2) at 50 s intervals. (b) linearity of current response (a1 and a2) vs. Glc concentration at CS-RGO-NiNPs SPE.

Table 3.2: Comparison of analytical performances of different enzymatic or enzymeless Ni-based biosensors

Electrode	Detection potential (V)	Sensitivity (μA·mM-1·cm-2)	Linear range	Detection limit (μM)
Ni-NDC(You et al. 2003)	+0.40	40.0	0.5μM-5mM	2.0
NiNPs-CFP(Liu et al. 2009b)	+0.60	3.3 μA· mM-1	2.0μM-2.5mM	1.0
Ni-MWCNTs(Sun et al. 2012)	+0.60	67.2	3.2μM-17.5mM	0.9
Ni(Zhao et al. 2007a)	+0.55	1.1 μA· mM-1	0.1-2.5mM	40
Ni powder-Nafion(Salimi and Roushani 2005)	+0.45	40.0 μA· mM-1	0.5μM-5mM	0.1
NiOnanosphere-GOx-CS(Li et al. 2008a)	+0.35	3.4μA· mM-1	1.5-7mM	47
NiO-MWCNTs(Shamsipur et al. 2010)	+0.60	13.7 μA·mM-1	Up to 12mM	160
NiO NPs(Mu et al. 2011)	+0.70	66.0	1-110μM	0.2
GOx-CS-BCNiNPs(Yang et al. 2011f)	−0.20	0.25 μA·mM-1	0.025-1.2mM	8.3

Ni/Al LDH-CS(Ai et al. 2008)	+0.70	0.2 μA· mM-1	0.01-10mM	10
GOx-CS-NiFe2O4NPs(Luo et al. 2010)	+0.60	45.6	1-8mM	N/A
NiMPs-BDD(Toghill et al. 2010a)	+0.48	1.0	0.01-10mM	2.7
NiNWA (Lu et al. 2009)	+0.55	1043	0.5μM-7mM	0.1
NiNPs/SMWCNTs (Nie et al. 2011)	+0.40	1438	1μM-1mM	0.5
CS-RGO-NiNPs(this work)	+0.60	318.4 (or 22.5μA·mM-1)	Up to 9mM	4.1

Abbreviations: N/A, not available; Ni-NDC, NiNPs in disordered graphite-like carbon; CFP/CPE, carbon nanofiber paste/carbon paste electrode; MWCNTs, multi-walled carbonnanotubes; BCNiNPs, boron-doped carbon-coated NiNPs; Ni/Al LDH, Ni/Al double-layered hydroxide; NiMPs-BDD, Ni microparticle modified boron doped diamond; NiNWA, Ni nanowire arrays; NiNPs/SMWCNTs, NiNPs modified straight multiwalled carbon nanotubes.

3.3.4 *Application of CS-RGO-NiNPs electrode*

Electrocatalytic performance of CS-RGO-NiNPs SPEs against Glc was further studied both in a conventional electrochemical cell and in the PDMS chamber of the fabricated microfluidic device by CVs using the same electrode (**Fig. 3.7a**). The electrocatalytic performance against the same concentration of Glc in the PDMS chamber of the microfluidic device was comparable to that in a conventional cell, in spite of the much smaller sample volume used in the microfluidic device. This result implies little hindrance of Glc detection from the PDMS microfluidic chamber which may actually contribute a little additional cell resistance, as is seen with some extent of decrease in overall background current. The selectivity of CS-RGO-NiNPs SPEs was tested in the presence of easily-oxidized compounds which are commonly coexisting with Glc in physiological samples (**Fig. 3.7b inset**). Under normal physiological conditions, the interfering species such as UA, AA and DA are present at levels lower than 0.1 mM, in other words, with Glc:interferent ratios of more than 30:1 (Park et al. 2003). However, these interferents can still produce oxidation current comparable to that of glucose, based on their higher electron transfer rates, especially at high detection potentials. Here interferents were tested at a high ratio of 1:10 to Glc. As observed, UA nearly produced no interfering signals while slightly increases in currents

were observed for AA and DA, generating 9.9% and 6.7% current changes which are not remarkable compared to the Glc current signal and are within the acceptable range. Actually, these mild current increases from interferents were previously reported in studies based on NiNPs catalysts(Nie et al. 2011) and can possibly be reduced by coating an outer molecule-selective membrane or doping Ni with other catalysts, though it might lower the sensitivity. In the meantime, the recovery rate in the presence of interferents was calculated to be 92.0%. These results suggested the sensor can be used for sensitive and specific detection of Glc virtually unaffected by the presence of common interferents.

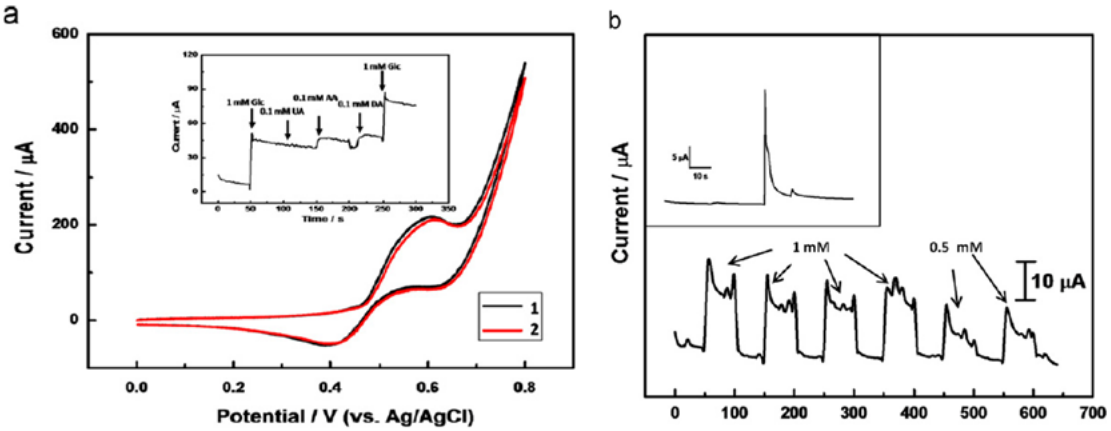

Fig. 3.7: (a) CVs of CS-RGO-NiNPs modified SPEs in 0.1 M NaOH containing 3 mM Glc (1) outside microfluidic chamber in a conventional electrochemical cell under unstirred conditions (2) within the PDMS microfluidic chamber. Scan rate: 0.1 Vs -1. Inset shows the result of sensing Glc in the presence of interferents UA, AA, and DA at an applied potential of +0.60 V. (b) Real-time amperometric detection of Glc at CS-RGO-NiNPs sensor in the microfluidic electrochemical device with successive microsyringe injections of buffer or Glc samples at 50 s intervals. Inset shows amperometric i-t curve of 0.1 mM Glc in the microfluidic device.

Consecutive real-time microfluidic analysis was conducted by manually injecting a buffer solution (0.1 M NaOH) with or without Glc in turn with a microsyringe (**Fig. 3.7b**). Samples containing either 1 mM or 0.5 mM Glc were tested, each followed by injection of the buffer. Each injection, either buffer or Glc sample, was carried out at 50 s intervals, due to the relatively long time for current to reach steady state (about 15 s). Immediately after the introduction of Glc samples at the inlet, an oxidation current was generated. Though the current decayed as always seen in electrochemical microfluidic devices due to diffusion (Lankelma et al. 2012a), a Glc-specific current could still be identified. The initial considerable increase in current was probably caused by instant high local Glc concentration at the electrode surface right after introduction and the current fluctuation should be ascribed to the liquid flow. The average of 1

mM Glc injections was calculated to be 0.99 mM from the calibration curve, with a relative standard deviation (RSD) of 8.7%, while 0.48 mM with RSD of 4.8% was obtained at Glc injections of 0.5 mM, demonstrating excellent accuracy in consecutive real-time Glc measurements of the electrochemical microfluidic device incorporated with disposable CS-RGO-NiNPs SPEs. Five measurements of 0.1 mM Glc by the same electrode were also tested, for which the RSD was 12.6%. In addition, five CS-RGO-NiNPs SPEs prepared under the same conditions were tested for current responses against 1 mM Glc with an RSD of 13.7%, indicating acceptable reproducibility. Stability of the sensor was investigated by measuring the sensitivity after being stored away from air in a Petri dish under room temperature for two weeks. It still retained 84.9% of its original sensitivity. Therefore, CS-RGO-NiNPs SPEs have good stability, reproducibility and portability for Glc detection, even though they were primarily fabricated single-use sensors.

Human urine samples were collected from healthy laboratory coworkers. Samples were diluted at a ratio of 1:2 (v/v) to 0.1 M NaOH and slightly adjusted to pH 13. They were stored at 4°C before use with no other pretreatments. Since Glc is not usually found in urine from healthy people and even if present, is in the range of 0.1 to 0.8mM, standard addition method was employed to spike samples with measurable amount of standard Glc of 0.5 mM and 1 mM. Noticeably in HPLC, a retention time shift of Glc was observed from 6.5 min in water to around 6.3 min in urine samples and 6.0 min in samples diluted with NaOH. In the microfluidic analytical device, an overwhelmingly large initial current appeared after sample injection and this current quickly decayed to a stable level for quantification within 15 s. As presented in **Table 3.3**, the results using electrochemical microfluidic device are close to those obtained using HPLC-amperometric detection and good recovery rates from 89 to 97% were acquired. Although no Glc could be virtually detected in subject 2 with both methods, a certain amount of Glc was surprisingly found in dense and dark yellow urine samples from healthy subject 1, approximately 0.59 mM at CS-RGO-NiNPs SPEs and 0.53 mM at HPLC. The comparatively concentrated condition of the urine sample and the Glc presence, which is still within the normal range may be caused by the dehydration or special diets of the subject when the sample was collected. These results illustrate good correspondence of the results from the analytical device to those from commercial HPLC-electrochemical instruments.

Table 3.3: Determination of Glc in human urine samples.

Sample #	Human subject #	Spiked (mM)	HPLC-amperometric detection(mM)	CS-RGO-NiNPs microfluidic sensor(mM)	RSD (%)	Recovery rate (%)
1	1	0.5	0.667	0.684	7.23%	89.32%
2	1	1.0	1.185	1.207	8.93%	94.18%
3	2	0.5	0.492	0.521	6.58%	97.11%
4	2	1.0	0.992	1.016	4.19%	91.66%

3.4. Conclusions

A simple, rapid, and convenient one-step approach has been proposed for synthesis of CS-RGO-NiNPs from the self-assembled nanocomposite precursor solution on SPEs, initiated simultaneously by pH-responsive electrodeposition of CS, electrochemical reduction (and deposition) of soluble GO into insoluble RGO as well as reduction of metal precursors into metal NPs. Deposited GO was electrochemically reduced *in situ* without any extra pre- or post-reduction steps. Uniformly distributed and interconnected NiNPs with relatively homogenous particle sizes could be observed in the CS and wrinkled ERGO scaffold. The resulting nanocomposites exhibited fast electron transfer kinetics and high electrocatalytic activity against Glc, with good sensitivity, selectivity and stability. A pocket-size, point-of-care electrochemical microfluidic sensing device was fabricated using PDMS photolithography and ABS plastic milling to incorporate the as-prepared disposable SPEs for real-time Glc monitoring in small sample volumes. Results of Glc measurements in human urine samples using the device correlated well with those obtained by HPLC-electrochemical instrument. The simple material synthesis, enzyme-free nature, portability, affordable cost and strong sensing performance of the reported device offers out-of-lab and beaker-free Glc sensing in healthcare.

Chapter 4: Enzymatic biosensing based on graphene hybrid materials*

4.1 Introduction

Heterogeneous bimetallic NPs have recently received much attention as electrocatalysts with enhanced activities (Zhang et al. 2007; Zhang et al. 2010a) and electrochemical reversibility for redox reactions (Katz et al. 2004), advantageous over bulk or pure metal materials. These bimetallic alloys could retain the functional properties of each component and possibly yield synergistic effects via cooperative interactions, resulting in interesting new features such as increased surface area, enhanced electrocatalytic activities, improved biocompatibility, promoted electron transfer and better invulnerability against intermediate species. Pt and Pd are the most frequently-used electrocatalysts for oxygen reduction reaction (ORR) with a similar mechanism of $4e^-$ reduction of oxygen to water, while Pd is among the most electrocatalytic pure metals in ORR other than Pt (Shao 2011). As Au is one of the only two transition metal more electronegative than Pt (Zhang et al. 2011b) and is relatively less reactive, the introduction of Au can have many appealing properties such as biocompatibility (Zhang et al. 2011a), stabilizing effect preventing metal dissolution during ORR (Zhang et al. 2007) and enhanced electrical conductivity (over pure Pd). AuNPs in the alloy also contribute as a biocompatible immobilization matrix necessary for biofunctionalization through ionic interactions and other interactions between AuNPs and mercapto or primary amine groups of biomolecules (Zhang et al. 2011a). Due to the high cost and limited resources of Pt in nature as well as the large miscibility gap between Pt and Au, Pd-Au alloy is an ideal alternative for ORR. It has been reported the addition of Au to Pd has a promotional effect on Pd's overall catalytic activity, selectivity and stability (Chen et al. 2005).

Graphene, which has been extensively researched in recent years as a rapidly rising star material, is a single-atom-thick planar sheet of hexagonally-arrayed sp^2-bonded carbon atoms packed in a 2-D honeycomb crystal lattice (Geim and Novoselov 2007). Despite its relatively short history, many interesting properties of graphene have been revealed such as high surface-to-volume ratio, large surface area, high electrocatalytic activity, fast electron transfers, low cost, robust mechanical properties, flexibility and outstanding conductivity (Stankovich et al. 2006), making it a promising material for applications in electronics/optoelectronics (Muszynski et al. 2008), sensors (Kang et al. 2009; Lu et al. 2011), composites (Stankovich et al. 2006), batteries

*This work has been published: (Yang et al. 2011b)

(Chou et al. 2010) and supercapacitors (Stoller et al. 2008). Its large accessible surface area is favorable for further modifications and biomolecule immobilizations (Choi et al. 2010). Graphene-based sensors were also reported to have higher sensitivities due to the low electronic noise from thermal effects, fast electron transfer kinetics and large surface area for analyte spatial interactions (Kang et al. 2009). Also owing to its simple chemical synthesis from inexpensive graphite, it serves as both a superior carbon support for growth of NPs and an electrical contact, providing electrode microenvironments as high-performance biosensors and promoting the performance of electrocatalysts. However, as the existence of residual defects in graphene can exert a significant influence on its electronic properties and future applications, efficient reduction of oxygenated species in graphene is on demand to prevent possible unwanted reactions and electrostatic adsorptions. Numerous studies have been focused on synthesis and applications of graphene inorganic nanocomposite materials very recently. Lu et al. reported the synthesis of Pd-functionalized graphene nanohybrids via a chemical reduction route as enzymeless Glc sensor (Lu et al. 2011). Another study successfully fabricated PtNPs-decorated graphene sheets using a microwave-assisted process for enzymatic sensing (Lu et al. 2008). Graphene modified by AuNPs with a chemical reduction strategy was also reported (Muszynski et al. 2008). Choi and coworkers prepared a conductive reduced graphene oxide/Nafion hydrid film via solution chemistry with synergistic effect in organophosphate detection (Choi et al. 2010). However, undesirable excessive reducing agents used in these methods would both increase the cost in mass production and could possibly remain and contaminate the synthesized materials. Meanwhile, oxygen-containing functional groups (-OH, C-O-C in the basal plane and –COOH, C=O on the edges) in graphene, though helpful in stabilization in water with high surface free energy, cannot be completely eliminated by chemical reduction and could continue to disrupt the electronic properties (Hernandez et al. 2008). Therefore, it is of great interest to look for a simple and environment-friendly approach for synthesis of graphene sheet-metal NP composites.

Electrodeposition is the most controllable and robust technique for synthesis of metal NPs, in which, the size, density, composition of alloys and even the shape of NPs could be well-controlled by electrodeposition potential, time, concentration and composition of metal precursor solutions (Claussen et al. 2009). We also previously electrodeposited copper metal NPs onto carbon nanotube arrays (Yang et al. 2010a). Electrochemical methods are also useful in reduction of graphene oxide (GO), strictly speaking an insulator, to eliminate oxygenated defect

sites to improve its electronic properties and evade possible chemical funtionalizations (Guo et al. 2009; Shao et al. 2010). The electrical conductivity of electrochemically-reduced graphene sheets is higher than that of graphene oxide or chemically-reduced graphene due to restoration of graphitic sp^2 bonds, while ERGO also have less defect sites and a higher reduction rate (Guo et al. 2009). Further modification of metal NPs can increase its electrical conductivity to a larger extent.

Herein, we reported a fast, controllable and green electrochemical approach free of reducing agents in synthesis of reduced graphene sheet-AuPdNPs (1:1) nanocomposites and its application as an oxidase-based biosensor based on O_2 reduction, starting from commercial graphite (**Scheme 4.1**). To our knowledge, this is the first report of electrochemical synthesis of ERGO-AuPdNPs nanocomposite for enzymatic mediator-free (reagentless) detection of Glc by sensing O_2 decrease. First, ERGO, which serves as electrically low-resistance contacted network in the biosensor, was synthesized from GO with a combination of oxidation and sonication procedures, followed by green electrochemical reduction of repetitive potential scans under room temperature to efficiently remove oxygen-containing species in GO. AuPd alloy NPs with relatively homogeneous size and shape were then electrochemically synthesized in one step under constant potential on the ERGO scaffold, resulting in enhanced electrocatalytic activity and stability towards O_2 reduction, promoted electron transfer and improved biocompatibility. To illustrate its significant medical application, GOx, as a model oxidase, was used to fabricate a sensitive enzymatic biosensor against the clinically important molecule Glc through the consumption of O_2 in the reaction. The whole fabrication process of the biosensor was step-by-step monitored by CV in ferricyanide and EIS. Our results showed high stability and sensitivity against O2 could be achieved by ERGO-AuPdNPs, a promising material for fuel cells and biosensors, while GOx-ERGO-AuPdNPs biosensor is distinguished as a potent candidate in clinical detection of Glc in human blood serum.

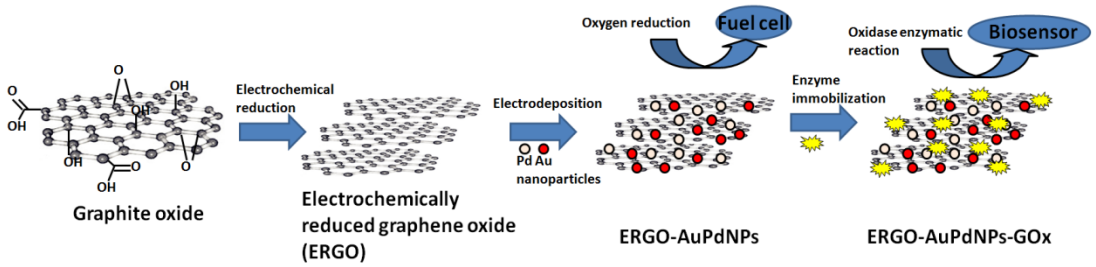

Scheme 4.1: Schematic diagram of electrochemical synthesis of ERGO-AuPdNPs nanocomposites and their potential applications

4.2. Materials and methods

4.2.1. Chemicals and reagents

Graphite powder and D(+)-glucose were purchased from Sinopharm Chemical Reagent and Glc solution was stored overnight at ambient conditions before use. Uric acid (UA) and L-ascorbic acid (AA) were received from Alfa Aesar. Gold (III) tetrachloride trihydrate ($HAuCl_4 \cdot 3H_2O$), palladium (II) chloride ($PdCl_2$), Nafion, GOx (EC 1.1.3.4, type X-S, lyophilized powder, 100-250 units mg^{-1}, from *Aspergillus niger*) were obtained from Sigma-Aldrich. All other reagents were of analytical grade and used as received. Posphate Double-distilled Milli-Q water (>18.2 MΩ) was used throughout the study and high purity N_2 was applied for deaeration.

4.2.2 Instruments

Scanning electron microscopy (SEM) and energy dispersive X-ray spectroscopy (EDS) were conducted by EDS-integrated Hitachi S-4800 (Hitachi, Japan) for surface morphology observations and surface elemental composition analysis. Samples for SEM (not EDS) were coated with Au films for increased conductivity using a vacuum spin coater. The particle size distribution was obtained using Image-Pro-Plus software. Atomic force microscopy (AFM) was operated in tapping mode using Agilent 5500 AFM system (Agilent Technologies, USA) with Picoscan software. Static water contact angles were measured with water drops under ambient conditions by ramé-hart-100 Contact Angle Goniometer (ramé-hart, USA). Cyclic voltammetry (CV) and differential pulse voltammetry (DPV) were performed on a CHI 430A electrochemical analyzer (CH Instruments, USA). All electrochemical measurements were conducted in phosphate buffer saline (0.05 M PBS pH 7.4) unless otherwise specified, on a conventional three-electrode system with a saturated calomel electrode (SCE) as the reference electrode, a platinum (Pt) wire electrode as the counter electrode and modified glass carbon electrodes as working electrodes. Electrochemical impedance spectroscopy (EIS) was carried out using the same three-electrode configuration above on a PGSTAT30/FRA2 system (Autolab, Eco-Chemie, the Netherlands) in a supporting electrolyte solution of 1.0 M KCl containing equimolar $[Fe(CN)_6]^{4-/3-}$ in a frequency range from 0.1 Hz to 100 kHz. The fit and simulation of equivalent circuit was analyzed with FRA software. Roche Modular Chemistry Analyzer (Roche, Swiss) was used for Glc analysis of human blood serum as a comparison with our biosensor.

4.2.3 Synthesis of ERGO

GO was synthesized using a modified Hummer's method (Hummers and Offeman 1958; Xu et al. 2008b). Typically, 3 g graphite powder, 2.5 g $K_2S_2O_8$ and 2.5 g P_2O_5 were added to 12 ml concentrated H_2SO_4 solution and reacted at 80 ºC for 4.5 h. After graphite oxidation, the mixture was diluted with 0.5 L water and kept at 80 ºC for another 12 h. The resulting solution was then filtered, washed with water and left overnight for drying at room temperature, before being re-dispersed in 120 ml concentrated H_2SO_4 with successive addition of 15 g $KMnO_4$ at temperature kept below 20 ºC under stirring. The mixture was left stirred at 40 ºC for 0.5 h and 90 ºC for 1.5 h, followed by dropwise addition of 250 ml water, incubation at 105 ºC for 25 min and stirring at room temperature for 2 h. 0.7 L water and 20 ml 30% (w/w) H_2O_2 were added to terminate the reaction. The resulting products were then filtered, washed with 3 M HCl solution, and repeatedly washed with water until the pH value of filtrate was neutral. It was further purified by dialysis for 1 week to remove residual salts, acids and metal species and was re-suspended by ultrasonication in water to obtain a homogeneous GO solution. 3 µl of 1 mg ml^{-1} GO solution was cast on a pretreated bare GCE surface and dried in ambient conditions. The electrochemical reduction of GO on GCE was conducted by repetitive CV scanning from 0 V to -1.5 V at 0.1 V/s in deaerated 0.05 M pH 5.0 PBS ($NaHPO_4$/NaH_2PO_4) for 100 cycles (Guo et al. 2009). ERGO-modified GCE was then rinsed with water and dried at room temperature.

4.2.4 Preparation of AuPdNPs-ERGO-GOx modified GCE

The modification of ERGO-GCE with AuPd metal alloy NPs (1:1) was achieved by electrodeposition technique under a constant potential of -0.2 V in a deaerated precursor solution consisting of 2.5 mM $HAuCl_4$, 2.5 mM $PdCl_2$, and 0.1 M KCl for an optimal time of 100 sec. For comparison, ERGO-GCE was also modified only by AuNPs or PdNPs respectively in their corresponding deposition solutions. The AuPdNPs-ERGO-GCE was then rinsed with 0.05 M pH 7.4 PBS, dried at room temperature, and immersed into 0.05 M pH 7.4 PBS containing 2.0 mg ml^{-1} GOx at 4 ºC for 24 h. The resulting AuPdNPs-ERGO-GOx modified GCE was rinsed several times with 0.05 M pH 7.4 PBS to wash off loosely absorbed enzymes and 5 µl 1% Nafion was cast on the electrode surface to maintain the electrode stability. The electrode was then stored in 0.05 M pH 7.4 PBS at 4 ºC ready to use and the Glc detection was done in an electrochemical cell with a flow of N_2 kept on the buffer surface. Indium tin oxide (ITO)-coated glass was modified with the same procedures and used instead of GCE for surface characterizations.

4.3. Results and discussion

4.3.1 Surface morphology

SEM image of ERGO displays a typical wrinkled sheet structure of graphene (**Fig. 4.1A**), and this geometric wrinkling not only minimizes the surface energy but also induces mechanical integrity with high Young's modulus, tensile strength and good film-forming ability, due to nanoscale sheet interlocking (Xu et al. 2008b). The substrate was observed to be uniformly covered with ERGO sheets stacked in parallel, providing a large rough surface as scaffold for further modifications. After modification, AuPd alloy NPs with fairly homogenous diameters of 43.5 ± 8.0 nm (as calculated from the histogram of size distribution) were found to be uniformly well-dispersed in the ERGO network, forming an interpenetrating network for favorable conduction pathways of electron transfers (**Fig. 4.1B**). Interestingly, AuPdNPs seemed more prone to deposit in large quantities at where ERGO sheets were wrinkled or curled into tubular-like structures, which might be attributed to higher static attractions during synthesis in a mechanism similar to what we found for MWCNTs previously (Yang et al. 2010a). Being efficiently immobilized in ERGO-AuPdNPs network, GOx formed a homogenous mushy film with island-like structures, offering an open network for substrate access (**Fig. 4.1C**).

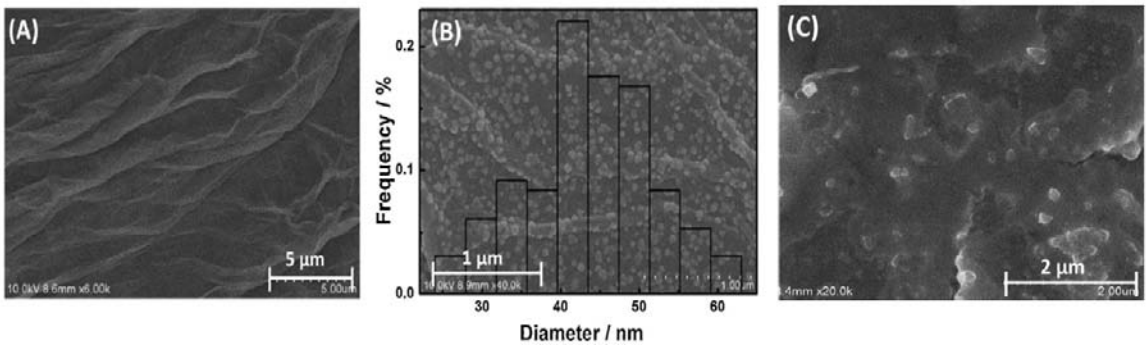

Fig. 4.1: SEM images of (A) ERGO. (B) AuPdNPs-ERGO. Overlay histogram the particle size distribution of AuPd alloy NPs on the ERGO network. (C) AuPdNPs-ERGO-GOx.

The morphology was further analyzed with AFM. The exfoliated unreduced GO clearly showed flat single layer of graphene nanosheets or multiple layers overlapped together in typical flake-like shapes, with fairly smooth surface, averaged height between 1-2 nm and lateral dimension of around 300 nm, indicating its atomic thickness composition (**Fig. 4.2A**). After the electrochemical reduction, averaged 10-20 nm wrinkled sheets were observed, which proved the successful electrochemical reduction of GO. Noticeably, some ERGO sheets were even wrinkled and curled into tubular-like structures, further increasing roughness and surface area

also shown by SEM (**Fig. 4.1B**). Electrochemical reduction was presumed to cause the observed restacking, corrugation and crumpling of GO sheets and therefore provided a good membrane-forming ability with larger surface coverage on substrate, suitable for large-scale production of reduced graphene sheets. When ERGO was further modified with AuPdNPs, the height profile obviously become rougher to a greater extent compared to ERGO, with more electroactive sites and larger surface area. The height analysis showed AuPdNPs had diameters between 20-50 nm, in consistence with the particle size distribution (**Fig. 4.1B**). As GOx was immobilized, a rather smooth film formed with clear island-like structures and little cracks, providing a good platform for biosensing.

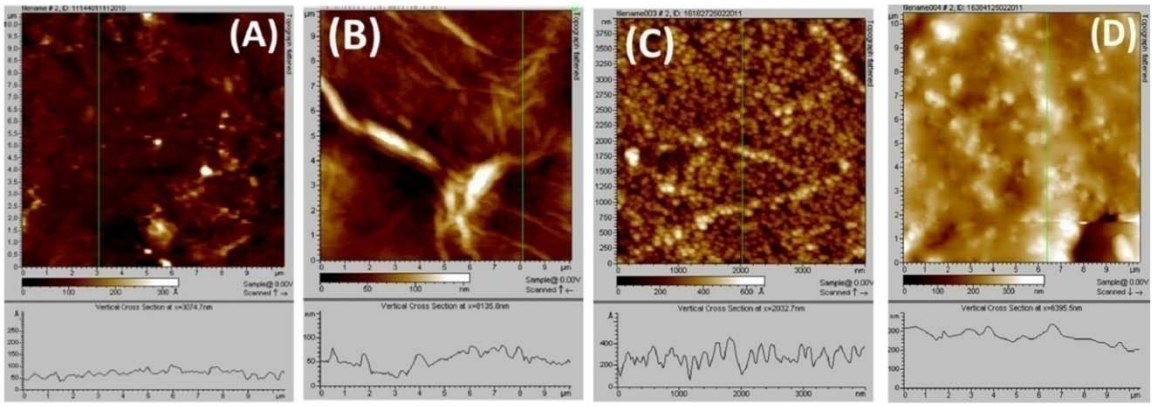

Fig. 4.2: AFM images with height profiles along the marked lines of (A) GO, (B) ERGO, (C) ERGO-AuPdNPs, (D) ERGO-AuPdNPs-GOx.

4.3.2 Characterizations of ERGO-AuPdNPs nanocomposites

Elemental compositions of ERGO-AuPdNPs were analyzed by EDS (**Fig. 4.3A**). Signature peaks for C, Au and Pd were observed for ERGO-AuPdNPs, while all other elements were from ITO substrates. The weight percentage of Au and Pd in the alloy NPs was found to be 64.9% and 35.13% respectively, resulting in an atomic ratio close to 1:1. This corresponds well to the molar ratio of metal precursors and indicates Au and Pd could both be successfully electrochemically synthesized under our conditions and contribute equally towards formation of bimetallic NPs during the synthesis.

The hydrophilicity, measured quantitatively by contact angles, is indicative for biocompatibility of materials (Deng et al. 2009a). Unreduced GO exhibited a smaller contact angle of 40.0° compared to 66.7° of ITO glass substrate (**Fig. 4.3B**), suggesting unreduced GO is

rather hydrophilic due to abundance of oxygen-containing functional groups. When GO was electrochemically reduced, the resulting ERGO became hydrophobic with an increased contact angle of 72.4° indicating the elimination of oxygenated species. After modification of AuPdNPs, the contact angle of ERGO-AuPdNPs decreased to 41.8°, retaining a hydrophilicity comparative to that of unreduced GO which is known as hydrophilic. The biocompatibility of ERGO-AuPdNPs nanocomposites could significantly facilitate enzyme immobilizations with reserved bioactivity.

EIS is a useful tool to monitor step-by-step modifications using $[Fe(CN)_6]^{4-/3-}$ redox couple as electrochemical probes. The semicircle portion in the high frequency regions in Nyquist complex plane plot is related to the charge transfer limiting process, while the charge transfer resistance (R_{ct}) can be calculated from the diameter. As GCE was modified with ERGO (curve b), the semicircle drastically decreased compared to that of bare GCE (curve a), with approximately half the R_{ct} of GCE. (**Fig. 4.3C**) This implies ERGO forms an interpenetrating network in favor of diffusion of redox probes and interfacial electron transfers, without surface charges caused by functional groups repelling the redox probes. Rct continued to decrease as ERGO was further modified with metal NPs, at 49.0, 108.9 and 39.6 Ω for Au, Pd and AuPd NPs respectively (curve c, d, e). This result shows AuPd alloy NPs is a better electron-transfer interface between electrode surface and electrolyte solution and also between electroactive sites of immobilized enzymes and electrode, compared to pure metal NPs, making ERGO-AuPdNPs an ideal platform as biosensors. With GOx successfully immobilized, R_{ct} of ERGO-AuPdNPs-GOx (curve f) dramatically increased to beyond 10^4 Ω, due to the blocking effects of GOx on electron transfers. The equivalent circuit model of ERGO-AuPdNPs is also shown in **Fig. 4.3C** and the simulated data fits (dotted line) well with experimental data of ERGO-AuPdNPs with errors < 4.0% for each element.

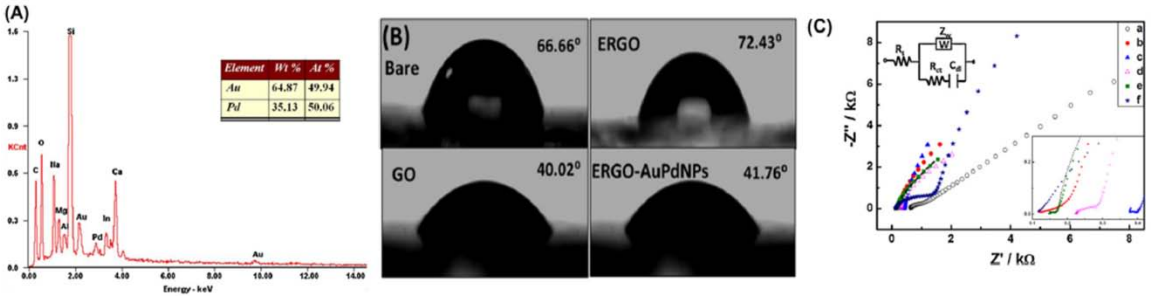

Fig. 4.3: (A) EDS spectra of AuPdNPs-ERGO. Inset shows the weight and atomic percentages of Au and Pd in the alloy. (B) Contact angles of bare, GO, ERGO and ERGO-AuPdNPs on substrates. (C) EIS spectra of (a) bare, (b) ERGO, (c) ERGO-AuNPs, (d) ERGO-PdNPs, (e) ERGO-AuPdNPs, (f) ERGO-AuPdNPs-GOx modified GCEs in 1.0 M KCl containing 5.0 mM $K_4[Fe(CN)_6]/K_3[Fe(CN)_6]$. Lower right inset shows magnification of the high frequency region. The dotted line indicates the simulation result of equivalent circuit $R_s([R_{ct}C_{dl}]Z_w)$ on the upper left to fit ERGO-AuPdNPs. R_s: solution resistance, R_{ct}: electron transfer resistance, C_{dl}: double layer capacitance, Z_w: Warburg impedance.

4.3.3 Electrochemical characterizations of ERGO-AuPdNPs

The repetitive cyclic voltammograms (100 cycles) for electrochemical reduction of GO modified GCE with a starting potential of -1.5 V are shown in **Fig. 4.4A**. An overwhelming cathodic reduction current starting from -0.7 V up to -1.5 V was found in the first cycle, with a current peak at around -1.3 V, which is ascribed to reduction of surface oxygen groups. This result is similar to a previous report, with a very close peak current (Guo et al. 2009). The reduction current began to drop exceptionally in the second cycle and continued to decrease with the CV scans progressed until it did not decrease obviously. After only a few potential sweeps, the reduction current disappeared in later cycles and the baseline current reached a stable plateau, manifesting the surface-oxygenated species were successfully reduced in a rapid way. Noticeable, since only cathodic current is observed, this electrochemical reduction is irreversible, happening only at potentials more negative than -0.7 V, with the reduction rate and degree controllable by scan rates and potential ranges. Furthermore, unreduced GO had a color of dark brown and after electrochemical reduction, the color turned into black, which could be more obviously seen on ITO.

Voltammetric responses in 1.0 M KCl containing 5.0 mM $K_3[Fe(CN)_6]$ were studied for intrinsic electrochemical properties and effective surface area estimation during modifications (**Fig. 4.4B**). ERGO modified GCE (curve b) has a slightly smaller peak potential separation and larger peak current of the signature well-defined peak pair (between +0.2 and +0.3 V) from reversible redox reactions of $Fe(CN)_6^{4-/3-}$ than bare GCE (curve a), demonstrating faster electron transfers and larger electroactive surface area for ERGO. After modification with metal NPs, peak potential separations (curve d 89 mV@Pd>curve c 69 mV@Au>curve e 65mV @AuPd) decreased while peak current (AuPd>Au≈Pd) increased. The surfa ce area of Au and Pd NPs is comparable while modification of AuPdNPs creates the largest surface area and provides a more effective conducting pathway with higher electron transfer rate coefficient. The marked increase in current of AuPdNPs-ERGO compared to ERGO also confirmed the contribution of

AuPdNPs in the increase of electroactive surface area. When GOx is immobilized (curve f), the peak current went down dramatically. The peak separation increased considerably to more than 300 mV, with electron transfers and diffusion of ferricyanide to electrode surface hindered by the biomolecule blocking layer. Notably, ERGO-AuPdNPs has a peak separation value very close to the ideal kinetics (59 mV) of one-electron Nernstain behavior, revealing excellent conductivity and ideal reversibility of the redox reaction. The effective surface area is calculated by Randles-Sevcik equation, assuming semi-infinite linear diffusion:

$$I_p = 2.69 \times 10^5 A D^{1/2} n^{3/2} v^{1/2} C$$

where n is number of electrons, C is concentration (mol/cm^3), v is the scan rate (V s^{-1}), D is diffusion coefficient (cm^2 s^{-1}). The effective surface area of ERGO, ERGO-AuPdNPs and ERGO-AuPdNPs-GOx is 0.067±0.002, 0.081±0.002 and 0.017±0.003 cm^2 respectively.

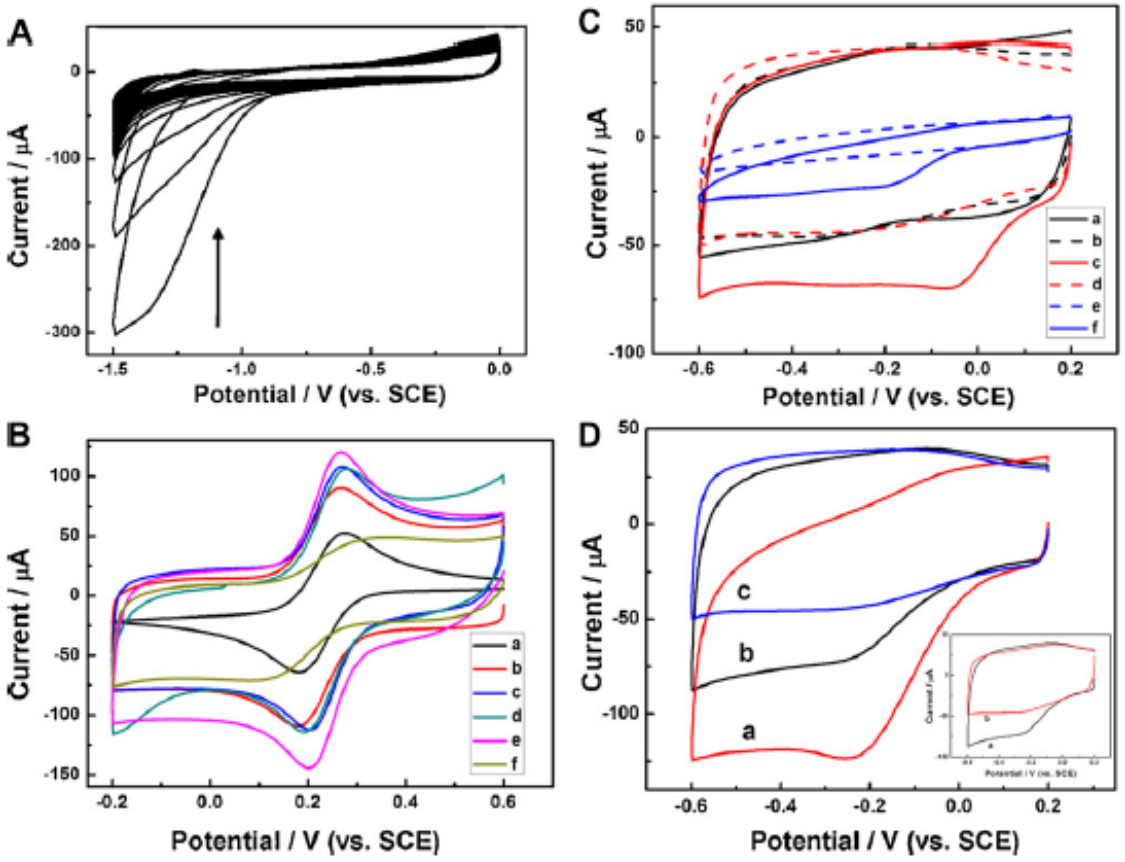

Fig. 4.4: Cyclic voltammograms of (A) GO-modified GCE in deaerated 0.05 M pH 5.0 PBS (100 cycles starting at -1.5 V). The big arrow indicates the progression of potential scanning while the small one denotes the reduction peak of GO. (B) (a) bare, (b) ERGO, (c) ERGO-AuNPs, (d) ERGO-PdNPs, (e) ERGO-

AuPdNPs, (f) ERGO-AuPdNPs-GOx modified GCEs in 5.0 mM $K_3[Fe(CN)_6]$ + 1.0 M KCl. (C) (a, b) ERGO (black), (c, d) ERGO-AuPdNPs (red), (e, f) AuPdNPs (blue) modified GCEs in 0.05 M pH 7.4 PBS saturated with (a, c and f) air (solid lines) and (b, d and e) N_2 (dotted lines). (D) ERGO-AuPdNPs-GOx modified GCE in 0.05 M pH 7.4 PBS saturated with (a) O_2, (b) air and (c) N_2. Inset shows ERGO-AuPdNPs-GOx modified GCE in air-saturated 0.05 M pH 7.4 PBS in the absence (a) and presence (b) of 3.0 mM Glc. Scan rates for all figures: 0.1 V s^{-1}.

4.3.4 Electrocatalytic performance of ERGO-AuPdNPs-GOx biosensor

The electrocatalysis of O_2 reduction was investigated by CV in 0.05 M pH 7.4 PBS at 0.1 V s^{-1} (**Fig. 4.4C**). In N_2-saturated PBS, AuPdNPs modified GCE did not show any significant peaks (curve e) while ERGO modified GCE displayed a pair of weak and broad redox peaks with cathodic peak lying between -0.4 and -0.3 V and anodic peak at around -0.2 V (curve b), due to subtle incomplete electrochemical reduction of oxygen species. In fact, most unstable oxygen-containing groups in ERGO (as the high cathodic current in **Fig. 4.4A**) have been reduced or eliminated with very weak redox peaks observed, while the remaining unreduced ones are only a small portion which might have been electrochemically-stabilized during the extensive CV cycling, with little damage on its electrical properties (Shao et al. 2010). As for ERGO-AuPdNPs modified GCE, it retained the minor redox peaks from ERGO in a nearly rectangular shape, interpreting good electron propagation within the electrode (curve d). On the other hand, in air-saturated PBS where O_2 is present, ERGO modified GCE only exhibited a tiny negligible current response towards O2 (curve a), illustrating very few defects are present and most oxygenated groups have been successfully removed. In contrast, both AuPdNPs (curve f) and ERGO-AuPdNPs (curve c) modified GCEs yielded a significant current increase, with onset potential of -0.05 V for AuPdNPs and +0.1 V for ERGO-AuPdNPs. Therefore, AuPd metal alloy NPs of ERGO-AuPdNPs nanocomposites play the key role in ORR. Moreover, the onset potential of ORR for ERGO-AuPdNPs is more positive than N-doped graphene (-0.2 V) (Qu et al. 2010), N-doped MWCNT arrays (-0.05 V) (Gong et al. 2009) and porous carbon-tetrathiafulvalene composites (-0.05 V) (Ndamanisha et al. 2010). Apparently, the current response of ERGO-AuPdNPs against O_2 was much higher than that of AuPdNPs and the peak potential of oxygen reduction at ERGO-AuPdNPs was -0.05 V compared to that of AuPdNPs at -0.2 V. The obviously low cathodic overpotential of ORR demonstrates a higher electrocatalytic activity of ERGO-AuPdNPs. This superior O_2 electrocatalytic performance of ERGO-AuPdNPs over AuPdNPs is attributed to the larger surface area, more electroactive sites, faster electron transfer kinetics and the

interpenetrating low-resistance 2-D network of ERGO, favorable for AuPdNPs dispersion and nucleation. Also regarding its relatively simple and environment-friendly synthesis, ERGO-AuPdNPs has the potential to be an excellent material for ORR.

Based on the consumption of oxygen in the enzymatic reaction with Glc and the enormously enhanced catalytic activity of ERGO-AuPdNPs nanocomposites towards oxygen reduction, an enzymatic biosensor was fabricated by immobilizing GOx into ERGO-AuPdNPs network. In this biosensor, Glc is selectively oxidized into gluconolactone (which is then hydrolyzes into gluconic acid) by oxygen in the enzymatic cycle of GOx, which in turn leads to a decreased concentration of dissolved oxygen in the system. Glc concentration can therefore be monitored by decrease of cathodic current signal from ORR, in a mechanism shown as below:

O_2 consumption: D-glucose + O_2 + H_2O $\xrightarrow{GO_x}$ D-gluconic acid + H_2O_2

O_2 reduction: $O_2 + 2H_2O + 4e^- \xrightarrow{AuPd} 4OH^-$

After GOx immobilization, ERGO-AuPdNPs-GOx exhibited a higher cathodic current in air-saturated PBS (curve b) than in N_2-saturated PBS (curve c), proving it reserved the electrocatalytic activity of ERGO-AuPdNPs towards O_2 (**Fig. 4.4D**). This was further confirmed by the observation of a much more remarkable current increase in O_2-saturated PBS (curve a) than air-saturated PBS. The cathodic peak potential of ERGO-AuPdNPs-GOx shift from from -0.05 V at ERGO-AuPdNPs to around -0.2 V, accompanied by diminishing peak current, was triggered by the enzyme film. In the air-saturated PBS solution with 3.0 mM Glc added, an obvious peak current decrease of ORR due to consumption of O_2 was seen (**Fig. 4.4D inset**), which could be used for in combination with the good selectivity of GOx towards determination of Glc.

Different durations of electrodeposition could lead to different densities, sizes, and even shapes of NPs formed on ERGO, resulting in different catalytic activities against O_2 reduction. The effect of deposition time on electrocatalytic activity of O2 reduction at ERGO-AuPdNPs modified GCE was shown in **Fig. 4.5A**. The highest electrocatalysis of O2 was achieved at 100 s. At shorter deposition time, the electroactive sites on ERGO surface could not be entirely occupied and AuPdNPs could not efficiently nucleate, causing a low density of NP dispersion, less electrocatalytic sites and thereby a low sensitivity against O_2 reduction. On the other hand, however, longer time would cause aggregation of NPs into larger particles or bulk clusters, eliminating the advantage of NPs with larger reactive surface area. Furthermore, the

electrocatalytic activity of bimetallic ERGO-AuPdNPs was also compared with ERGO-AuNPs and ERGO-PdNPs (**Fig. 4.5A inset**). It was observed that ERGO-AuNPs could only achieve about 70% the electrocatalytic activity of ERGO-AuPdNPs, whereas ERGO-PdNPs also had a comparatively lower electrocatalytic activity than ERGO-AuPdNPs. It should be noted that Pd showed astonishingly superior initial performance in O_2 reduction and the high performance could not be sustained, though Pd is famous as a strong catalyst. This decrease in catalytic performance is due to gradual dissolution of Pd and its vulnerability towards intermediate species (Zhang et al. 2010a). Therefore, introduction of Au in Pd could both enhance the catalytic activity and stability against O_2, owing to the isolation of single Pd sites by Au, which can facilitate the coupling of surface species (Chen et al. 2005).

Glc determination was accomplished by DPV in air-saturated 0.05 M pH 7.4 PBS (**Fig. 4.5B**). When Glc was absent, only one peak between -0.1 and -0.2 V which ascribed to oxygen reduction at ERGO-AuPdNPs-GOx was found, without any other peaks interfering the detection. Upon Glc addition, the current of the peak began to decrease, with a linear dependence on Glc concentration in the range of 0.5-3.5 mM (i(μA)=18.70-4.53*C, R^2=0.99). It should be pointed out that, with increasing Glc concentration, the weak and unnoticeable peak from ERGO at around -0.3 V began to become noticeable (relatively obvious for DPV with addition of 3.5 mM Glc and higher), though it did not hinder the detection. Based on the calibration curve, the sensitivity of the biosensor is calculated to be 266.6 μA mM^{-1} cm^{-2} (**Fig. 4.5B inset**), with a detection limit of 6.9 μM at signal/noise ratio of 3. This sensitivity is higher than many enzymatic sensors such as 5.2 μA mM^{-1} cm^{-2} at GOx/Pd-Au/ASWCNTs/Si (Claussen et al. 2009), 13.0 μA mM^{-1} cm^{-2} at N doped-MWCNTs-GOx (Deng et al. 2009a), 37.9 μA mM^{-1} cm^{-2} at GOx-graphene-chitosan (Kang et al. 2009), 61.5 μA mM^{-1} cm^{-2} and 47.9 μA mM^{-1} cm^{-2} at Pt or PdNPs-xGnPs-GOx (Lu et al. 2008) as well as non-enzymatic ones such as 160.0 μA mM^{-1} cm^{-2} at PdNPs-SWNTs (Meng et al. 2009) and 10.8 μA mM^{-1} cm^{-2} at nanoporous PtPb (Wang et al. 2008b). The indicator of enzyme-substrate reaction kinetics, the apparent Michaelis-Menten constant (K_m^{app}), was calculated according to the electrochemical version of Lineweaver-Burk equation to evaluate the affinity and biological reactivity of the immobilized enzyme to the substrate:

$$\frac{1}{i} = \frac{1}{i_{max}} + \frac{K_m^{app}}{C i_{max}}$$

The K_m^{app} of the biosensor was 10.5 mM, presenting a good substrate affinity towards Glc.

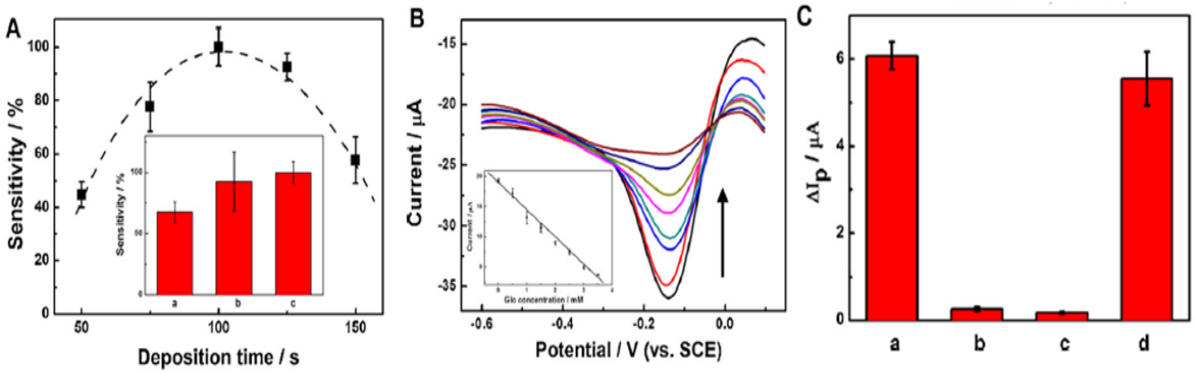

Fig. 4.5: (A) Effect of deposition time on sensitivity against O_2. Inset shows sensitivities of (a) ERGO-AuNPs, (b) ERGO-PdNPs, (c) ERGO-AuPdNPs modified GCEs against O_2. (B) Differential pulse voltammograms of ERGO-AuPdNPs-GOx modified GCE in air-saturated 0.05 M pH 7.4 PBS containing 0.0-3.5 mM Glc from outside to inside as the arrow indicates, at a potential step of 4 mV, a frequency of 60 Hz and amplitude of 50 mV. Inset shows linear dependence of peak currents on Glc concentrations as calibration curve. (C) Peak current decreases of DPV at ERGO-AuPdNPs-GOx modified GCE in air-saturated 0.05 M pH 7.4 PBS in the presence of (a) 1.0 mM Glc, (b) 1.0 mM AA, (c) 1.0 mM UA and (d) 1.0 mM Glc after being stored for two weeks. Error bars indicate standard deviations of triplicate measurements.

4.3.5 Analytical applications of ERGO-AuPdNPs-GOx biosensor

The influence of oxidizable interfering species possibly coexisting with Glc in human serum was examined by investigating the ORR peak current change of DPV with 1.0 mM UA or AA added to 1.0 mM Glc in air-saturated 0.05 M pH 7.4 PBS (**Fig. 4.5C**). There was only a minimal interference of 4.2% and 2.9% from AA and UA respectively to Glc, without appearance of any additional peaks. A good selectivity against endogenously-coexisting electroactive species was presented by ERGO-AuPdNPs-GOx biosensor (Wang et al. 2008b), due to the low overpotential at which these species generate negligible responses. The stability was tested by measuring the peak current decrease of ORR against 1.0 mM Glc (**Fig. 4.5C, d**) with the biosensor stored in 0.05 M pH 7.4 PBS at 4 ºC. There were no significant decrease in response in several days and only an 8.6% loss of original response was observed after two weeks of storage, implying the enzyme was stably immobilized in ERGO-AuPdNPs network with its bioactivity well-reserved. The reproducibility of the biosensor was checked by detecting 1.0 mM Glc using five independently-fabricated electrode, with an acceptable relative standard deviation (RSD) of 9.7%, while 10 successively measurements of 1.0 mM Glc were conducted at the same electrode with a RSD of 6.3%.

Serum sample (#)	Concentration by Roche Modular System (mM)	Concentration by the proposed biosensor (mM)	Recovery rate (%)
1	8.07	7.56 ± 0.48	93.19
2	5.27	5.86 ± 0.55	95.66
3	4.86	4.37 ± 0.43	107.98
4	8.50	8.22 ± 0.36	101.54

Table 4.1: Determination of Glc concentrations in human serum samples by our proposed biosensor (n=3) and clinical chemistry analyzer

The clinical performance of the biosensor was tested by measuring Glc concentration in human blood serum samples from a hospital, with comparison with a Roche Modular Chemistry Analyzer (**Table 4.1**). Serum samples of 4 individuals were drawn and tested without any sample pretreatments. The normal Glc concentration in human serum is in the range of 3.0-8.0 mM, while some patients with diabetes can reach as high as 13.0 mM. Limited by the comparative narrow linear range of our biosensor which only has an upper limit of 3.5 mM, the serum samples were diluted before testing. The results from our biosensor were consistent with those obtained by clinical analyzer, with errors around or within 10%. The recovery rates of our sensor were estimated to be over 90%, validating its accuracy as a novel nanocomposite material and a potential candidate for routine Glc measurements, though some limitations of the biosensor do exist. Some limitations include the relatively narrow linear range, high detection limit, long detection time using DPV, the stringent reaction conditions for enzymes (e.g., pH, temperature) and last but not the least, a strictly-controlled O_2-free environment. In our future work, we will try to further optimize the biosensor performances on Glc by varying the atomic ratio of metals, doping additional metals in the alloys, introducing biopolymer membranes to increase biocompatibility, as well as application on other oxidases.

4.4 Conclusions

This study explores a simple, controllable, fast, convenient and green electrochemical approach towards synthesis of reduced GO-AuPdNPs nanocomoposites in which oxygenated species are efficiently removed without any reducing agents. The synthesized ERGO-AuPdNPs

show a homogeneous dispersion is of the bimetallic alloy NPs in the wrinkled ERGO scaffold, with good biocompatibility, fast electron transfer kinetics, large electroactive surface area, high sensitivity and stability against O_2 reduction. Based on these appealing characteristics, a Glc biosensor can be fabricated by detecting the O_2 consumption during the enzymatic reaction of GOx. The as-prepared biosensor exhibits a high sensitivity, good stability, acceptable reproducibility, high substrate affinity and specificity in Glc detection and can be successfully applied in clinical detection of Glc in human serum, offering a new approach for development of oxidase-based biosensors.

Chapter 5: Enzymatic biosensing using paper fluidic devices

5.1 Introduction

In the analytical field, there has always been an unmet demand for highly sensitive, specific, stable, cost-effective biosensors for clinical diagnosis(Wu et al. 2008), food safety and quality control(Boehm et al. 2007; Yang et al. 2012b) and environmental monitoring(Tan et al. 2010), preferably with in-field portability as well as simple and facile fabrication and storage. Paper and its derivatives have been and will continue to be the major analytical platform most noticeable in low-volume immuno- and enzyme-based bioassays(Martinez et al. 2008). Paper as a thin porous medium is an agglomeration of bonded hygroscopic cellulose fibers easy for wicking; it is also ubiquitous and inexpensive. Paper not only offers extra advantages such as minimal weight per surface area, flexibility, disposability, biocompatibility, biodegradability, power-free fluid control by capillary pressures but also alleviates the environmental concerns as it is a natural and renewable material. Paper-based microfluidic device uses capillary action through the pores of the paper structure to transport sample liquids and molecules. This eliminates moving parts or external connections for liquid handling and results in low-cost, on-site analysis. Paper is also easy to store, transport, and manipulate and already commercially available in a lot of engineered forms(Martinez et al. 2008), with the functional groups on cellulose fibers for easy functionalizations. Unwanted large particulates and dusts can be filtered from analytical samples depending on the pore size and it can be used as a chromatographic support to elute and separate analytes(Metcalf et al. 1982). Thus, paper-fluidic devices are increasingly considered as point-of-care analytical devices.

Paper-based analytical methods have been achieved with infrared (IR) spectroscopy(Trafela et al. 2007), colorimetric assays(Martinez et al. 2008; Zhao et al. 2008), electrochemiluminescence (ECL)(Delaney et al. 2011), mass spectrometry (MS)(Ho et al. 2011), chemuluminescence(Yu et al. 2011b) and surface enhanced Raman spectroscopy(Yu and White 2010). Using paper-fluidic devices in conjunction with electroanalytical sensors is a new trend in routine analytical chemistry (Lankelma et al. 2012b; Nie et al. 2010) due to the combined advantages of miniaturization, low-cost, high sensitivity, easy operations, etc.. It gives convenience and simplicity in terms of use and storage with low cost and a long shelf life. Paper has been popular in enzyme assays and enzyme paper test strips are readily available for a long time. In fact, oxidative enzymes such as laccase and peroxidase are also widely used for

biobleaching of virgin pulp and recycled secondary fiber to increase both mechanical and optical qualities for inexpensive and stable paper(Knutson and Ragauskas 2004). Some studies have been conducted using paper-fluidic enzymatic electrochemical biosensors. Nie et al. fabricated microfluidic paper-based electrochemical devices for heavy metal and Glc detection(Nie et al. 2010). Another study was carried out for Glc, lactate and uric acid detection with printed Prussian Blue electrode detecting H_2O_2 (Dungchai et al. 2009).They both involved photolithography or wax printing patterning along with enzyme spotting technique so that the complicated immobilization and storage procedures for enzyme electrodes are largely avoided.

Herein we report a simple and facile paper-based microfluidic electrochemical enzymatic biosensor using GO_x as a model enzyme with ambient O_2 as cosubstrate. Rather than spotting and filtration techniques, dip coating technique was employed to make standard enzyme strips. This technique allows making multiple reproducible enzyme-adsorbed paper pads at the same time from an enzyme solution without the assistance of a micropipette. It is potentially suitable for reproducible mass manufacturing if the concentration of enzyme solution can be well maintained between batches. After enzyme modification, the paper retains its hydrophilicity, flexibility and mechanical properties and behaves even better at break strain. A commercially available SPE was modified by electrochemically-synthesized PtNPs in a precursor solution without utilizing reducing reagents. PtNPs is more selective for detection of the enzyme reaction product H_2O_2 than standard carbon electrodes with boosted hydrophillicity, electrical conductivity, surface area and electrocatalytic activities. In the meantime, its operation potential is much lower which is less likely to cause other undesirable electrocatalytic reactions. In our device, ABS holders provide good alignment and hold of enzyme paper chips and SPEs to achieve a stable sensing signal. In this way, SPEs can be used for multiple times unlike enzyme electrodes with disposable enzyme paper chips and stored away from a PBS buffer. SPEs can be replaced with fresh ones by dismantling the device (**Scheme 5.1**). PtNPs-modified SPE showed similar electrochemical behaviors in paper substrate to bulk solution, independent of sample volumes larger than saturation volume. Its amperometric detection displayed a typical diffusion-limited current signal. Concentration effects in paper are observed due to repetitive additions but an upper limit reached with about three additions. It also has potential for real-time multiple detections and regeneration ability to eliminate memory effects. Potentially, the device can incorporate other enzymes and other inorganic electrode materials for sensing. All these traits make it a fascinating inexpensive, eco-friendly and portable analytical device.

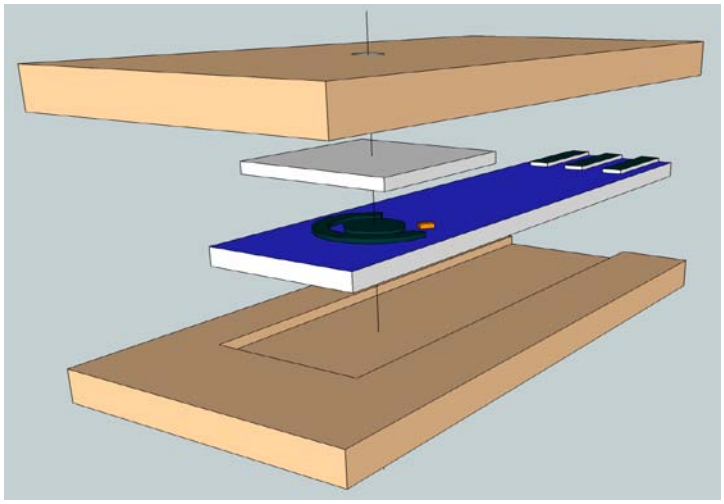

Scheme 5.1: A schematic diagram of the whole device setup.

5.2. Experimental design

5.2.1 Chemicals and reagents

Dihydrogen hexachloroplatinate(IV) hexahydrate ($H_2PtCl_6 \cdot 6H_2O$) was obtained from Alfa Aesar and GO_x (Type X, activity>100·mU g^{-1}, from *Aspergillusniger*) was purchased from MP biomedicals. Methylene blue and filtered10x phosphate buffered saline (PBS) stock solution were acquired from Fisher Scientific. The buffer was diluted to 1x solution by water upon use with a final phosphate concentration of 11.9 mM at pH 7.4. All other chemicals were of analytical grade and used as received. Doubly distilled Milli-Q water (>18.2 MΩ) was employed in the whole study. Whatman grade 1 chromatography paper (Whatman 1 Chr) made of pure cellulose (thickness 180 µm from provider)was used as the paper fluidic substrate for analytical filtering, separation and sensing owing to its smooth surface, good fluid wicking ability and fast fluid linear flow rate (130 mm/30 min). Commercially-available SPEs with integrated three electrode configurations were provided by Zensor, featuring graphitic carbon working (with geometric area of ~7.07 mm^2) and counter electrodes and Ag/AgCl pellet reference electrode. 11.9 mM PBS pH 7.4 was used throughout the study unless otherwise noted.

5.2.2 Apparatus

Surface morphology was analyzed by scanning electron microscopy (SEM) using LEO 1530 Gemini FESEM (Carl Zeiss, USA). Water contact angles were measured by OCA 15 Optical Contact Angle Measuring System (Data Physics, USA) with 8.0 µL of water at a medium rate of

1.0 µL·s^{-1}. MTS Insight® Electromechanical Testing System (5 kN standard length) was used to test the mechanical properties of different paper (MTS, USA). All test specimens for tensile tests are dried and with exactly the same dimensions. All electrochemical measurements were performed with a CHI 660D electrochemical analyzer (CH Instruments, TX, USA) at ambient temperature (25±1°C) using three-electrode configuration. High speed zoom camera (HS EX-FH100, CASIO, Japan) with 224 x 168 (420 fps) recorded pixels, F5.7 aperture and 11.9x optical zoom was used to observe the liquid behaviors within paper.

5.2.3 Fabrication of apparatus

Aapparatus to hold SPE and paper strip was fabricated by three dimensional milling machine (iModela IM-01, Roland co.) using ABS sheet. The holder is composed of two plates. The bottom plate has an engraved groove to hold SPE. The top plate has a 3 mm diameter through hole to apply sample liquid in the center of electrodes area in SPE. The 1 cm^2 square-shape Whatman No. 1 filter paper was cut and located between top cover and SPE. The paper was aligned on top of SPE sensing area. The holder was clipped with a binding clip to provide a constant uniaxial vertical force for good alignment between the paper and SPE sensor.

5.2.4 Modification of SPEs and paper

Before electrode modification, SPEs were immersed into the N_2-purged precursor solution comprised of 2.0 mM $H_2PtCl_6$and 0.5 M KCl and stabilized for 10 min. The modification of SPEs with PtNPs was conducted at a constant potential of -0.4 V in the above solution for 100 s. The modified SPEs were rinsed with PBS and dried at room temperature. Whatman No. 1 cellulose paper (10 mm x 10 mm) was soaked in an enzyme solution (120 U of GO_x enzyme activity) for 2 h at 4°C, dried overnight for a prolonged time and stored under the same temperature before use for preservation of enzymatic activities. The enzyme is immobilized and stored in paper through physisorption and hydrogen bonding between cellulose fibers and enzymes, similar to filtration (Comfort et al. 1989) and spotting(Martinez et al. 2008) approaches, while the mild drying procedure can optimally retain the enzyme activity. After the paper was dried, it slightly turned from white to yellow due to the enzyme adsorption. For comparison, water-soaked paper was treated in a similar manner in DI water. For real-time amperometric measurements, 20 µL (determined from both wicking test and electrochemical experiments) 11.9 mM PBS pH 7.4 was typically added to wick the paper substrate beforehand as a stable baseline current to

make good electrical contacts between paper and electrode surface. It is also ascribed to the conductivity differences between liquid (buffer) and air, otherwise blank buffer is likely to cause false detectable current signals.

5.3 Results and discussion

5.3.1 Surface and mechanical characterizations of the paper-fluidic electrochemical biosensor

Typical flake-like graphitic carbon sheet particles were observed on the SEM image of unmodified carbon SPE (**Fig. 5.1B**). They are covered with blurred and irregular materials which might be polymeric binders, forming a webbed surface but not thoroughly filling up the interparticle gaps. These rather porous and rough surface structures are generally directly correlated to large electroactive sites and fast electron transfers, with the exposed edge plane-like sites and defects as sole origins of electron transfers(Kadara et al. 2009a). After synthesis, PtNPs with sizes of 100-150 nm in spherical shape were homogeneously distributed in the porous carbon network (**Fig. 5.1A**), serving as sensitive catalysts for H_2O_2 detection. Untreated Whatman No. 1 paper has an extremely low ash content of <0.06% (from provider) and a porous randomly-felted micro-scale fiber network with loose and hollow structures between the bonded microfiber aggregates (**Fig. 5.1C**). The averaged diameter of rolled fibers is 10.3 µm. This structure features a great water-absorbing ability of paper which is directly related to the paper porosity(Cerpakovska et al. 2009). Enzyme immobilization does not cause a significant change to the overall morphology and the fibers preserve the cellulosic fibrous network (**Fig. 5.1D**). Enzymes in a 'mushy' appearance attach to the fiber surface uniformly, form a thin composite cladding around them and also fill up the hollow interfiber space to an extent, due to the excellent biocompatibility of cellulose(Liu et al. 2012).The resulting material network looks compact, filled and hard with little open pore volume. This typical structure might also be an explanation to the enhanced mechanical properties of enzyme-modified paper observed in later study.

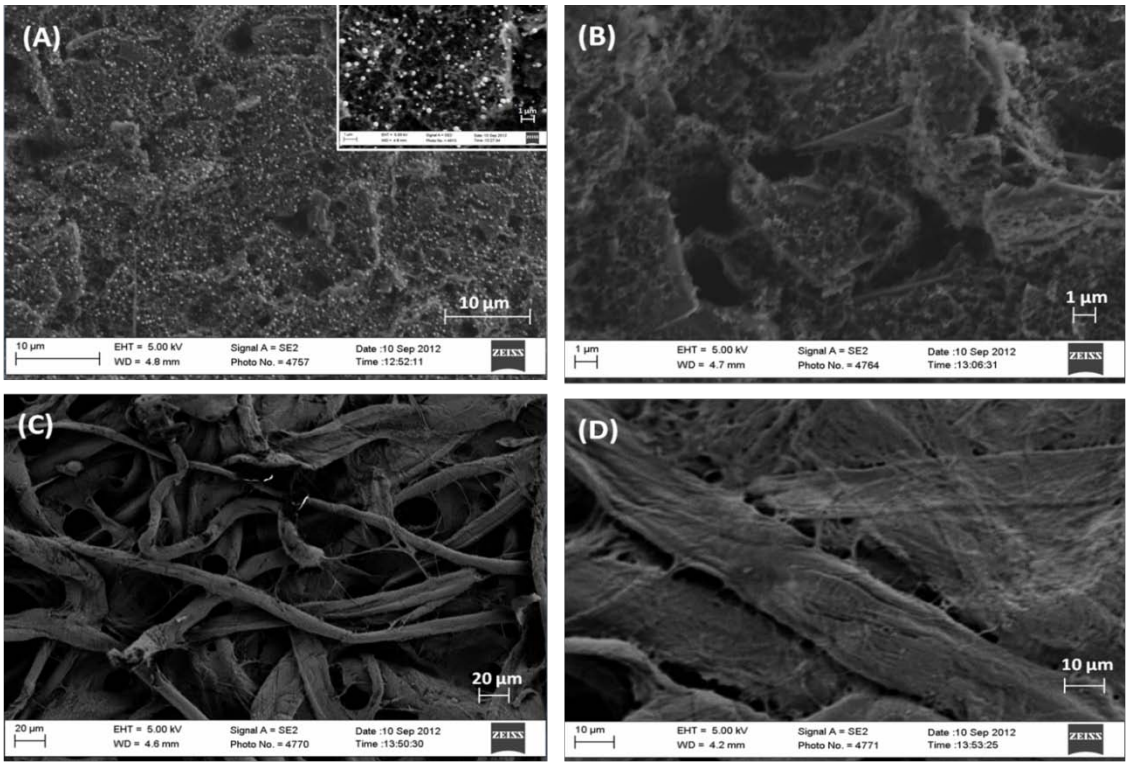

Fig. 5.1: SEM images of (A) PtNPs-modified SPE (higher magnification shown as inset) (B) bare SPE (C) unmodified paper (D) enzyme-modified paper

The hydrophilicity is measured quantitatively by static water contact angles. The bare carbon SPE displayed a fairly large contact angle of 105.9° (**Fig. 5.2A**). After modification with PtNPs, a decreased contact angle of 75.5° could be found indicating a considerable increase in hydrophilicity for PtNPs-SPE. This may be in favor of more efficient sensing in an aqueous environment when samples are delivered to electrode surface by paper for better electrical contacts and sensing. Whatman No. 1 paperhas been known for its hydrophilicity (**Fig. 5.2C**) and the cellulose paper still keeps its extraordinary water absorbing ability after enzyme immobilization (**Fig. 5.2D**), due to the hydrophilic nature of the enzyme. Therefore, the enzyme-functionalized paper is still capable of storing the samples, 'mixing' them with the immobilized enzymes and efficiently transporting them to the sensing region with comparable properties as native cellulose paper.

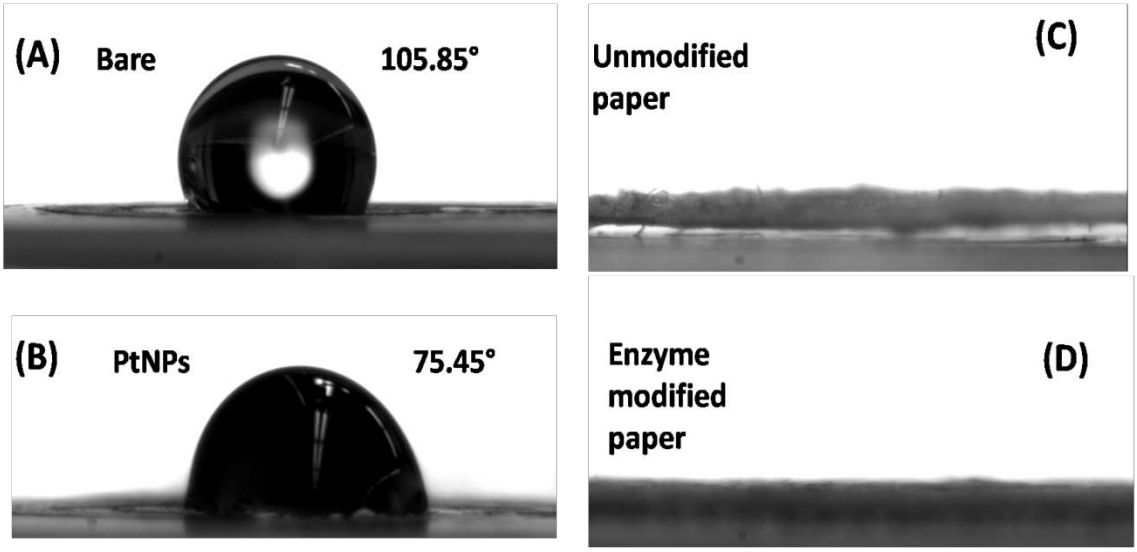

Fig. 5.2: Water contact angles of (A) bare SPE (B) PtNPs-modified SPE (C) unmodified paper (D) enzyme-modified paper.

The mechanical properties of paper were investigated by a tensile strength test as shown in the stress-strain curves (**Fig. 5.3A**).Young's modulus (or modulus of elasticity) determined by the nature of materials from Hook's Lawas the ratio of stress and strain ($E=\sigma/\varepsilon$) is insensitive to heat treatment and compositionand it serves as an indicator of material stiffness to resist elastic deformation. As the same tensile stress ($\sigma=F/S_0$) which is the ratio of tensile load to cross-sectional area applied, enzyme-modified paper (b) exhibited a tensile strain comparable to that of native paper (a), both of which are much smaller than that of water-soaked and dried paper. As such, from the slope of elastic linear portion, comparable Young's Modulus of enzyme-modified paper and native paper can be obtained (**Fig. 5.3B** 1a and 3a), larger than water-soaked paper (2a). Meanwhile, enzyme-modified paper also has the widest reversible elastic deformation (or proportional limit stress) and irreversible plastic deformation ranges and largest yield strength, with the larger peak tensile strength (or ultimate/maximum tensile strength) and strain at break (**Fig. 5.3B** b and c) than native and water-soaked paper. These findings in excellent mechanical properties of enzyme-modified paper are consistent with previous reports that water-soaking can decrease the tensile strength and tear resistance of paper(Cerpakovska et al. 2009) and oxidative enzymes such as peroxidase, xylanase and laccase (in our case, GO_x) result in improvements in paper sheet strength(Chandra and Ragauskas 2005; Mansfield 2002). Water absorption can cause plasticization of cellulose fibers, relaxing and weakening of inter-fiber bonding and loss of water-soluble paper adhesives as seen by the weight loss in soaked

paper, though this influence on decreased mechanical properties is not likely to depend on quantity of soaked water(Cerpakovska et al. 2009).After enzyme immobilization, the increase in mechanical properties might be a synergic effect of hydrogen bonding between cellulose fibers and enzymes as well as fiber oxidation with increased fiber surface carboxylic acid groups(Chandra and Ragauskas 2005).

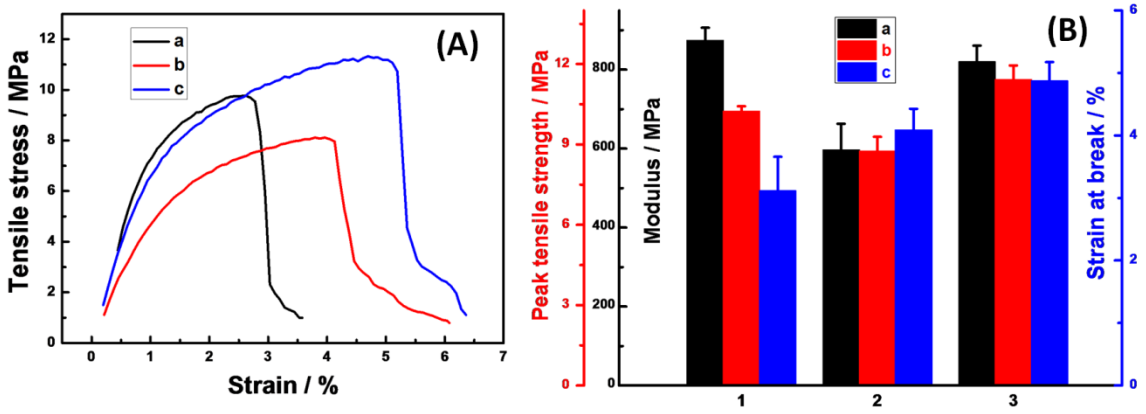

Fig. 5.3: (A) Stress-strain curves of (a) untreated paper, (b) water-soaked and dried paper, and (c) enzyme-modified paper. (B) Comparison of (a) Young's modulus, (b) peak tensile strength and (c) strain at break of (1) untreated paper, (2) water-soaked and dried paper, and (3) enzyme-modified paper.

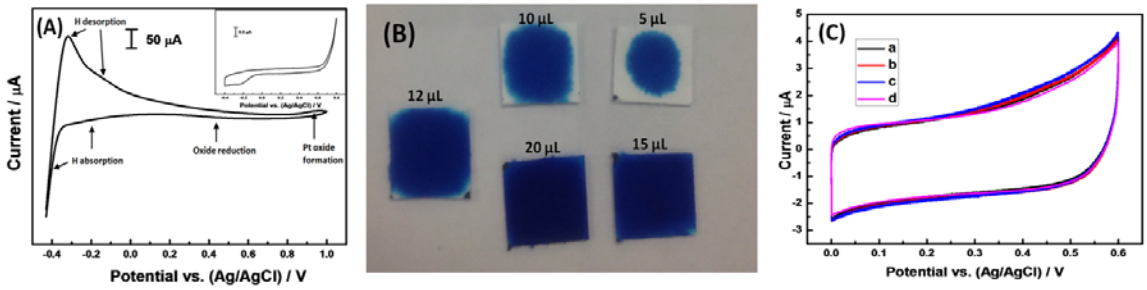

Fig. 5.4: CVs of (A) PtNPs-modified and unmodified (inset) SPEs in 1.0 M H_2SO_4. (B) Wicking test of paper with 5, 10, 12, 15 and 20 µL methylene blue solution. (C) PtNPs-modified SPE with (a) 30, (b) 60 and (c) 90 µl additions of 11.9 mM pH 7.4 PBS buffer in the paper substrate, and (d) in a PBS bulk solution in a conventional electrochemical cell under the same conditions. Scan rate: 100 $mV \cdot s^{-1}$.

5.3.2 Electrochemical characterizations of the paper-fluidic electrochemical biosensor

The electrochemical behaviors of SPEs were studied in 1.0 M H_2SO_4 by cyclic voltammetry (CV). The characteristic peaks of hydrogen adsorption and desorption along with Pt oxide formation and oxide reduction from crystalline Pt could be observed (**Fig. 5.4A**). This typical

behavior is much different from an unmodified carbon electrode (**Fig. 5.4A** inset), indicating PtNPs are successfully synthesized on the SPE carbon support. Therefore, PtNPs-modified SPE has a large electrochemical active surface area for electrocatalysis, as estimated from the area (charge) under the voltammetric curve.

The electrical resistance and the dielectric constant of paper are known to vary with moisture or water content, which are important for paper-fluidic electrochemical sensing. Low water content will not only hinder sample being delivered to SPE sensing surface for detection but also prevent the paper from being a 'beaker' to achieve electrical contacts. In our preliminary paper-based electrochemical testing, we found low sample volume injection can cause low current background or even fail in current measurement due to unsaturated paper and high electrical resistance, even though the uniaxial vertical force is applied at the ABS device. Therefore, a water absorption wicking test was conducted using a methylene blue dye solution to investigate the amount of sample needed to fully saturate the paper strip (**Fig. 5.4B**). It was observed at least 20 µL liquid is required to completely wick the paper test strip. Although from our experiments this amount is enough to achieve a stable current signal ignoring evaporation during the measurement, this does not mean the paper is actually saturated. The actual maximum liquid retention value (LRV) of paper can be much larger because porous cellulose fibers can be swelled by water especially in compressed condition(Mantanis et al. 1995)provided by our device and water as a dipole molecule can also be absorbed outside the paper via hydrogen bonding from out-of-plane H and O atoms on the sugar molecules. Liquid can also be stored between the spacing of two ABS holders and thus our device can 'hold' much more liquid in addition to the 'inside' of the paper structure. PtNPs-modified SPE exhibited similar voltammetric behaviors in PBS-wetted paper with different volumes (**Fig. 5.4C**) to that of bulk solution in a beaker, consistent to a previous report in Whitesides' group that diffusion is close in paper and bulk, and mass-limited electron transfer from redox reactions is not slowed in paper compared to bulk solution(Nie et al. 2010). Therefore, we conclude the sample volumes (typically >20µL for the paper size) do not significantly affect electrochemical behaviors.

5.3.3 H_2O_2sensing performances of the paper-fluidic electrochemical biosensor

Since the detection mechanism of our paper-fluidic electrochemical biosensor towards Glc is based on detecting the enzyme reaction peroxide product with consumption of ambient

oxygen cosubstrate, in a manner similar to the first generation of biosensors except without using enzyme electrodes:

$$\text{D-glucose} + O_2 + H_2O \xrightarrow{GO_x} \text{D-gluconic acid} + H_2O_2$$

The electrochemical oxidation of H_2O_2 involves three steps(Hall et al. 2000): binding of H_2O_2 to oxidized Pt surface sites to form a surface complex; internal electron transfer to reduce the surface site back to Pt; in-situ electrochemical oxidation to recover oxidized Pt site. This reaction is of great importance for a lot of amperometric enzyme-based biosensors. The electrocatalytic activities of unmodified and PtNPs-modified SPEs against H_2O_2 were tested by CV in PBS with or without H_2O_2 in paper substrate, as depicted in **Fig. 5.5A**. Unmodified SPE only displayed a puny current signal (**Fig. 5.5A** inset b) and in contrast, PtNPs-modified SPE showed an overwhelmingly large oxidation current against H_2O_2 (c), illustrating PtNPs are good electrocatalysts and sensitive to H_2O_2.Noticeably in our study, the oxidation current signal of PtNPs-SPE in PBS containing H_2O_2 (b) is comparable to that with a PBS addition and a following addition of PBS containing H_2O_2 after complete wicking (c). The mobility of liquid in paper is lower in wet state than in dry state, as the mobility resistance in liquid is larger than in air. Probably the first PBS addition pre-occupied the porous structure of dry paper near the sensing surface and they diffused out to the edges far away from sensing area quickly. The second addition containing H_2O_2can thus easily 'wash away' the previous PBS and took place of the pores near the sample injection hole which is designed near the 3-electrode sensing region. As a result, they have comparable oxidation current signals. If another drop of PBS containing the same H_2O_2 concentration is added subsequently (d), it generated a slightly higher signal (but not double) due to temporarily high local concentration, usually known as 'concentration effect'. It is caused by retention of H_2O_2in the sensing region from the second addition which is added up with the third addition and causes larger current, but this concentration effect is not infinite and has an upper limit. The concentration effect due to repetitive sample addition and retention is an important characteristic of paper-based sensing (Rattanarat et al. 2012). Meanwhile, the current signal also decreases slowly with time by diffusion, following Fick's Second Law.

Fig. 5.5: (A) CVs of PtNPs modified SPEs with (a) 30 µl 11.9 mM pH 7.4 PBS buffer, (b) 90 µl PBS + 30 µl PBS containing 1.0 mM H_2O_2, (c) 30 µl PBS containing 1.0 mM H_2O_2, (d) 90 µl PBS + 30 µl 1.0 mM H_2O_2 +30 µl 1.0 mM H_2O_2 in PBS added consecutively to the paper substrate. Inset shows CVs of bare SPEs with (a) 30 µl 11.9 mM pH 7.4 PBS buffer and (b) 30 µl PBS containing 10.0 mM H_2O_2. Scan rate: 100 $mV{\cdot}s^{-1}$. (B)

Amperometric i-t curves of (a) PtNPs-modified SPE with 20 µl 11.9 mM pH 7.4 PBS containing 1.0 mM H_2O_2, and (b) bare SPEs with 20 µl 11.9 mM pH 7.4 PBS containing 10.0 mM H_2O_2 added to the paper substrate at time=50 s. (C) On-line amperometric measurements of PtNPs modified SPEs with intermittent additions of 20 µl 11.9 mM pH 7.4 PBS containing 0 antd 1.0 mM H_2O_2 to the paper substrate t a time interval of 50 s. (D) Linear dependence of H_2O_2 concentration on current intensity from amperometric i-t curves. Inset shows amperometric responses of PtNPs modified SPEs with step-wise additions of 20 µl 11.9 mM pH 7.4 PBS containing 0.5, 1.0, and 1.5 mM H_2O_2 to the paper substrate. (E) Real-time amperometric responses of PtNPs modified SPEs with 20 µl 11.9 mM pH 7.4 PBS containing 1.0 mM H_2O_2 continuously added to the paper substrate. The arrows indicate introduction of PBS buffer. Applied potential: +0.4 V.

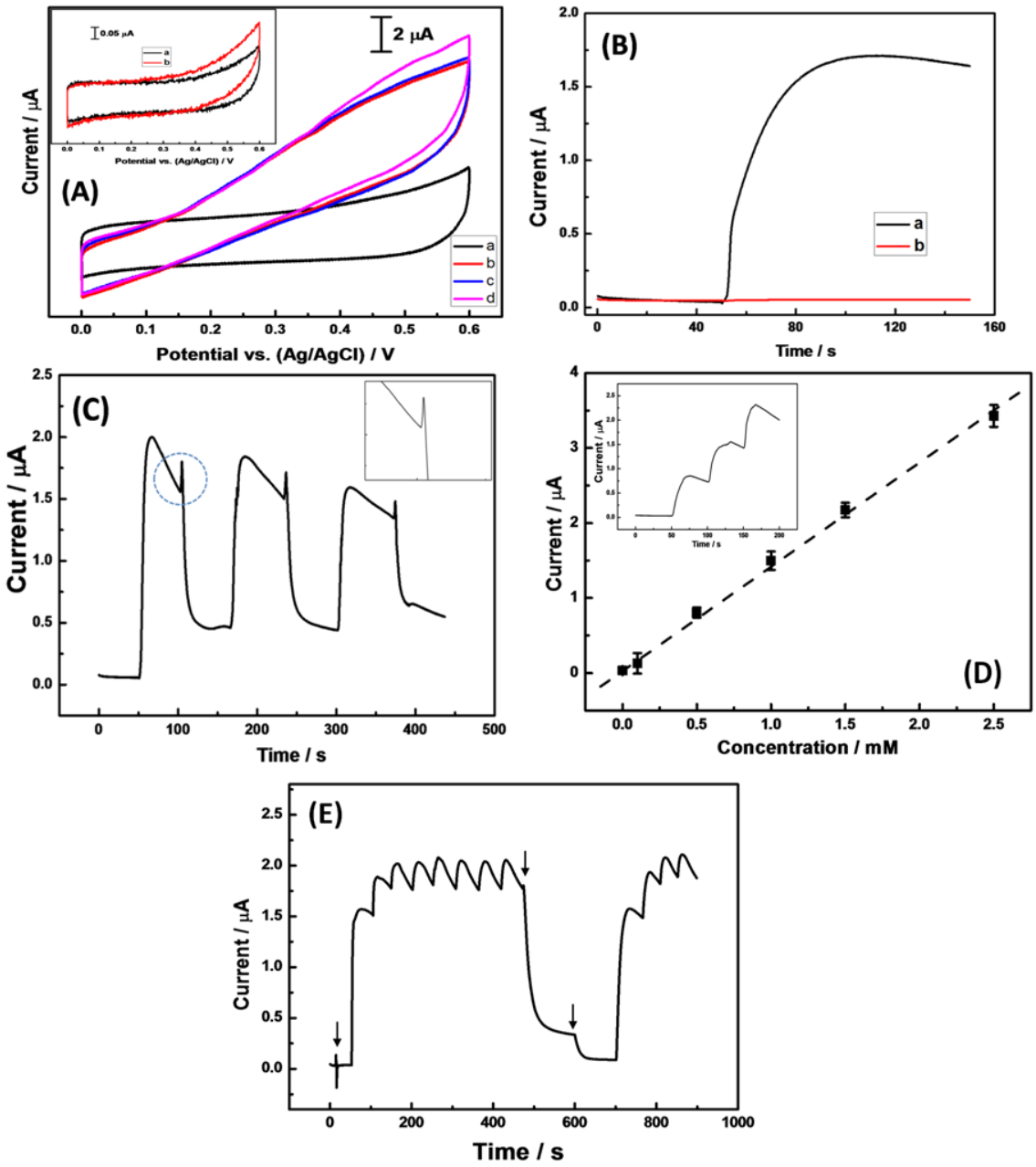

Amperometric i-t curves of bare and PtNPs-modified SPEs are compared in **Fig. 5.5B**. PtNPs-SPE (a) produced much larger oxidation current signal than bare SPE (b) even at1/10 of analyte concentration, consistent with results of CVs. It is obvious that the current at PtNPs-SPE increases dramatically after H_2O_2 addition and decreased slowly with time as a typical non-steady state diffusion, similar to the Cotrell behaviors of diffusion-limited condition in a still solution in a conventional electrochemical cell. Therefore, the diffusion in paper for PtNPs-SPE also follows Fick's Law. Furthermore, it takes a fairly long time of about 40 s to achieve the largest current signal as a result of the slow energy-free diffusion within paper, while in a conventional electrochemical cell it might usually take less time than that. For practical applications, it is vital to accomplish real-time and regenerative detections. Real-time analysis was evaluated by consecutively introducing PBS with or without H_2O_2 (**Fig. 5.5C**).The current signal rises immediately after onset of H_2O_2 injection, reaches maximum value with the highest local concentration on SPE surface and decays gradually due to diffusion and decrease in local concentrations. Moreover, the current signal is fairly smooth and flow-induced current fluctuation is barely seen, indicating paper-fluidic is an efficient, energy-free and stable approach to deliver liquid for electrochemical sensing. Apart from the fast and sensitive response, the recovery of the paper-fluidic electrochemical sensor is also rapid with introduction of buffer. The current returns to a new baseline level to achieve steady-state current within 30 s, but an apparent memory effect can be observed probably caused by retention of previous samples in the paper network. As the mobility of liquid is slower in a wicked paper, one buffer introduction might not be sufficient to 'wash off' the previous samples leading to the comparatively higher baseline. The buffer introduction also caused an amperometric spike before rapid decays (**Fig. 5.5C** inset), which is likely to be caused by instantly increased local diffusion rate after introduction. This phenomenon is similar to that in a flow injection analysis (FIA) system where oxidation current increases with increasing flow rate (Zhao et al. 2007b). In spite of some memory effects, repetitive injections of equal H_2O_2 concentrations yielded similar reproducible absolute oxidation current values, demonstrating its potential for multiple measurements.

The amperometric current responses towards H_2O_2 oxidation followed a linear dependence (R^2=0.997) on H_2O_2 concentration with a sensitivity of 19.4 μA mM^{-1} cm^{-2} (**Fig. 5.5D**). The detection limit for H_2O_2 at signal-to-noise ratio (S/N) of 3 is calculated to be 2.4 μM. Successive additions of equally increasing concentrations of 0.5, 1.0 and 1.5 mM result in

uniform step-wise increasing current signals (**Fig. 5.5D** inset), but this linear behavior in the same paper is limited. On one hand, it may exceed the dynamic working range while on the other hand subsequently much higher concentration could be 'diluted' by former lower concentrations, causing the observed signal lower than the actual signal. The higher a subsequent concentration is than the previous, the more inaccurate the signal is, from the same paper. Regarding this problem, more reliable calibration curves should be calculated based on different new paper substrates but no successive additions, regardless of the techniques used (amperometry, voltammetry etc.). This concern is also validated from **Fig. 5.5A** as the concentration effect gives false inaccurate larger signals with repetitive additions of the same analyte concentration. The result is further confirmed by repetitive addition of the same H_2O_2 concentration (**Fig. 5.5E**). Pure PBS buffer did not cause significant increase in current but only a temporary current spike from changing local diffusion rate which disappeared quickly (first arrow). Following the first introduction of H_2O_2 which caused a drastic current rise, the second and third repeated injections led to continuous minute increases corresponding well to the observation of concentration effect in CVs (**Fig. 5.5A**). As demonstrated above, this effect has an upper limit and in our study from the fourth addition on, further addition no longer triggered concentration effect, with the maximum plateau current maintained at the same level. Even after so many additions, the paper-fluidic biosensor still showed acceptable recovery ability and the second PBS addition (third arrow) can completely regenerate the sensor by returning the current to its original level and eliminating the memory effect. The second detection gave highly reproducible results and still exhibited concentration effects in the first three introductions. These results proved the paper device with applied compressed force can be subject to a large liquid volume, suitable for continuous or repetitive detections.

5.3.4 Simple 2-D capillary behaviors in paper

The liquid fluidic behavior in porous paper such as absorption, flow rate (wicking rate) and retention are important characteristics for electrochemical sensing. For better and easier understandings, a simple 2-D capillary-flow model is built. External applications of hydrodynamic compression pressures provided by holders in this study are known to influence the wicking behaviors in that increasing applied pressure leads to an increase in liquid absorption rate and a decrease in saturation time(Masoodi et al. 2010), favorable for rapid sample delivery and subsequent electrochemical sensing. However, since the applied pressure in our study can

hardly be accurate measured even if it is nearly constant, this compression effect is neglected. Therefore, the sole driving force for wicking behaviors is capillary pressure. As another important factor that affects wicking, swelling of cellulose fibers occurs when the wetting liquid such as water comes into contact, until they reach the equilibrium state. The swelling which is related to water holding capacity is caused by fiber-water interactions. The structure and molecular arrangement of fibers are changed during swelling process in turn leading to changes in the capillary pore radius, porosity and permeability of paper, depending on material crystallinity. Swelled fibers lead to larger pores which thus have more room for water retention. This effect is also ignored. The porous paper substrate is assumed to be comprised of numerous capillary tubes of constant radii. In each capillary tube, the flow physics is assumed to be single-phase. The capillary-tube based flows are regarded as 2-D instead of 3-D in paper, with the thickness of paper and gravity neglected. In reality based on Fick's model concentration-dependent diffusion, the wicking speed could be a little different from the actual value, but the concentration effect is not taken into account for simplicity. From **Fig. 5.6**, we can see that the liquid sample travels technically at equal speeds vertically and horizontally within the cellulose network of paper. The acceleration decreases with passed time upon addition of sample and the speeds also decrease due to hindrance of the matrices.

Fig. 5.6: (A) Time-dependant photographs taken by high-speed camera. The ruler shows a scale of 0.5 mm. (B) Vertical length average of the droplet travels vs. time. (C) Horizontal length average of the droplet travels vs. time.

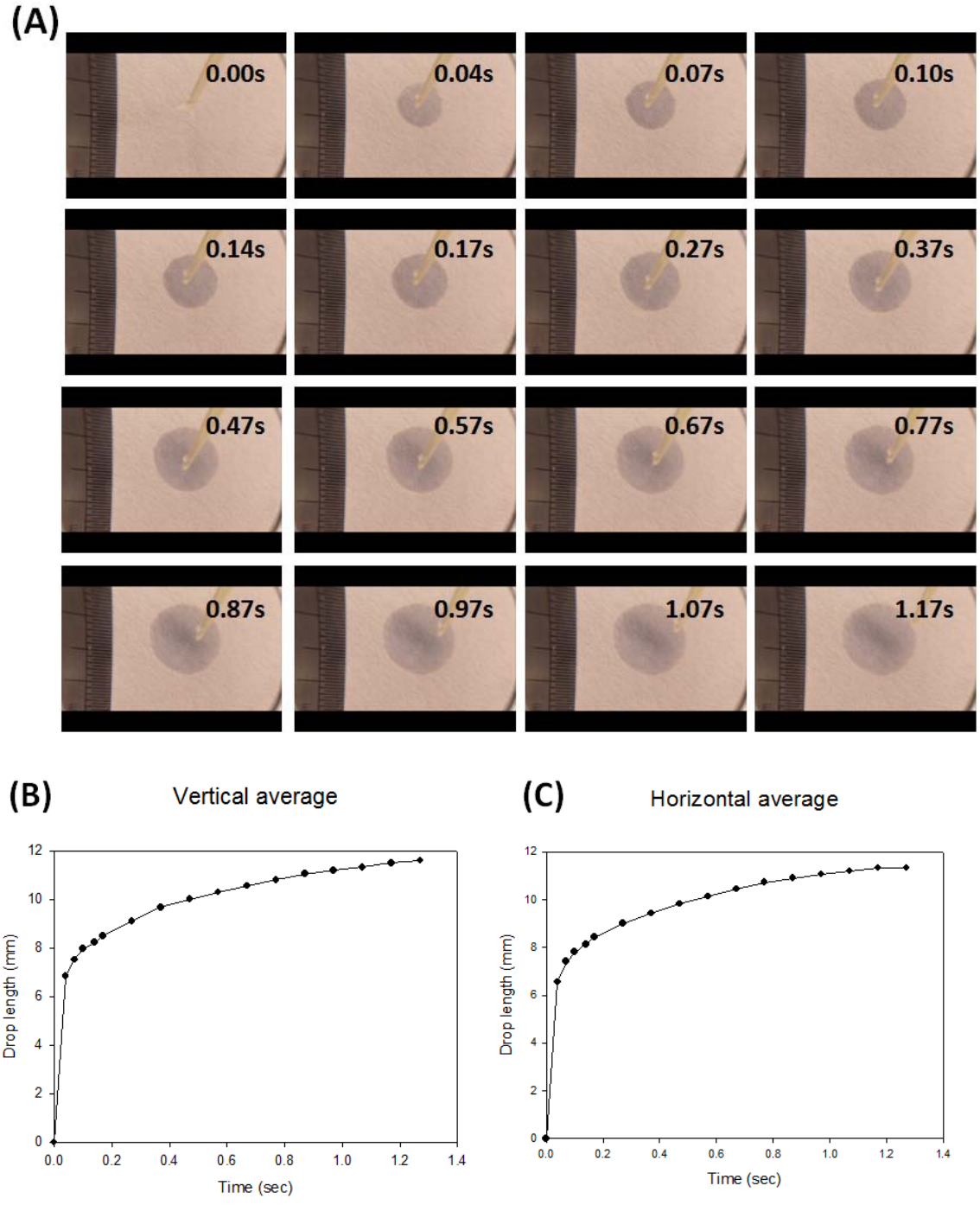

5.3.5 Glc sensing using the paper-fluidic electrochemical biosensor

Glc sensing performance of the paper-fluidic electrochemical biosensor was assessed by CVs in PBS in the absence of Glc and in the presence of a series of different Glc concentrations

(**Fig. 5.7A**). After Glc introduction, a strong oxidation current (b)with the voltammetric behavior similar to H_2O_2 oxidation (**Fig. 5.5A**) can be observed, manifesting it is aroused by oxidation of the enzymatic reaction product H_2O_2. The oxidation current increases with increasing Glc concentrations and a linear dependency of current at +0.4 V on Glc concentration can be built (R^2=0.994), giving a sensitivity of 10.5 µA mM^{-1} cm^{-2}, a detection limit of 9.3 µM (at S/N=3) and a dynamic working range from 0.5 to 3.0 mM. The indicator of enzyme-substrate reaction kinetics, the apparent Michaelis-Menten constant (K_m^{app}), was calculated according to the electrochemical version of Lineweaver-Burk double reciprocal equation to evaluate the affinity and biological reactivity of the enzyme-functionalized paper to the substrate(Zeng et al. 2009b):

$$\frac{1}{i} = \frac{1}{i_{max}} + \frac{K_m^{app}}{C i_{max}}$$

The K_m^{app} of the biosensor is0.8mMwhich is smaller than enzyme electrodes with enzymes immobilized on chitosan-ionic liquid-AuNPs (7.8 mM)(Zeng et al. 2009b), reduced graphene sheet-AuPd NPs (10.5 mM) (Yang et al. 2011b), nano Co phthalocyanine (12.4 mM)(Wang et al. 2005), N-doped carbon nanotubes (2.2 mM)(Deng et al. 2009b) and comparable layer-by-layer assembly on carbon nanotubes (0.95 mM)(Deng et al. 2010). Thereby it presents a good substrate affinity and high preserved enzyme activity towards Glc after immobilization on paper. Others have large K_m^{app} since those are in bulk liquid, hence has longer diffusion time for the analyte from liquid into surface.

Fig. 5.7: (A) CVs of PtNPs-modified SPEs with 20 µl 11.9 mM pH 7.4 PBS containing 0, 0.5, 1.0, 1.5, 2.0, 2.5 and 3.0 mM Glc added to enzyme-modified paper substrate. Inset shows the linear relationship of Glc concentration on current. (B) Amperometric i-t curves of PtNPs-modified SPEs with (a) 5.0 mM Glc added to unmodified paper substrate and (b) 1.0 mM Glc added to enzyme-modified paper substrate. Applied potential: +0.4 V.

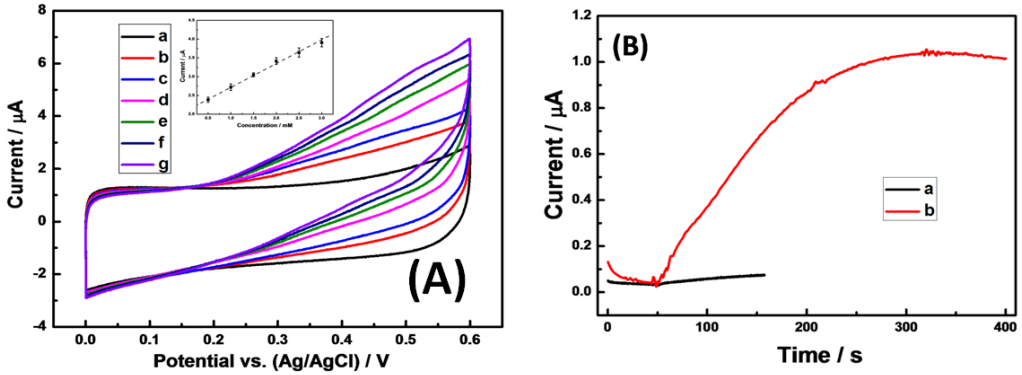

Amperometric detection using the paper-fluidic electrochemical biosensor was also examined as shown in **Fig. 5.7B**. The amperometric response is much larger with enzyme-modified paper (b) than in an unmodified paper (a) both with PtNPs-SPE for detection, even the latter has a 5-fold higher Glc concentration than the former. It elucidates that the strong current comes from oxidation of the enzymatic reaction product H_2O_2 rather than direct Glc oxidation, while the minor current increase in unmodified paper should be ascribed to non-enzymatic Glc oxidation in Pt nanostructures(Park et al. 2012). Notably it takes even longer time to achieve the current signal in Glc detection (200 s) than H_2O_2 detection, owing to the time needed for enzymatic reaction and delivery of the product H_2O_2 in paper to the sensing region. A major advantage of the dip-coating approach used in the study is the large-scale parallel preparation of multiple enzyme paper strips. We found at least 10 enzyme-functionalized paper strips can be prepared with maintained enzyme activities for a 5 ml enzyme solution giving as satisfactory relative standard deviation (RSD) of 7.6% with 1.0 mM Glc addition. However, new enzyme solution is required for larger amount preparation, since previous manufacture will potentially decrease the enzyme units in the solution and thus affect the enzymes absorbed onto the paper with reduced sensing performances. The preservation of enzyme activities was examined after the paper was stored at 4°Cin a Petri dish over a period of 2 weeks and the sensing performance was barely affected other than standard deviations. A previous study has suggested enzyme-spotted paper can retain its activities for 30 days when stored at 25°C without excluding air(Martinez et al. 2008). The stability of the enzyme immobilized in paper will further increased by using optimized drying method such as lyophilization, as well as addition of preserving chemicals.These results claim that paper can well reserve enzyme activities for long term storage and be used conveniently for reliable detections with mass production capability than other approaches such as filtering and spotting. The preparation and sensing methods in this study can be easily extended for many other enzymes.

5.4 Conclusions

We described an analytical portable device for enzyme assays free from any complicated immobilization and modification procedures. This paper-based microfluidic electrochemical enzymatic biosensor stands out from using a standard enzyme electrode with the aid of dip-coated enzyme-modified paper which serves for sample delivery and mixing with diffusion in the absence of external power supply, together with enzymatic reaction. Furthermore, an external

clamped ABS holder in this device ensures stable alignment between paper and SPE, and a close contact between liquid sample and electrode surface by supplying a constant hydrodynamic compression pressure for faster and larger liquid absorption capability. The simple fabrication, ease of operation, stability and miniaturization of this device enables a good strategy in making enzymatic biosensors for various applications in the future.

Chapter 6: Electrochemical sensing of lean meat powder ingredients in meat samples with a disposable working electrode*

6.1 Introduction

Indium tin oxide (ITO or $InSnO_x$)-coated glass is a promising photoelectric material because of its excellent optical transparency and satisfactory electrical conductivity. Applications of ITO include light-emitting diodes (LED), solar cells, transistors, biosensors, electroluminescence devices, liquid crystal displays (LCD) and shieldings. It can also be easily etched, patterned and microarrayed for targeted surface functionalizaiton and biomolecule immobilization(Grisotto et al. 2011; Ng et al. 2002; Shi et al. 2011). ITO is also widely used as an electrochemical sensing platform(Shi et al. 2011). The use of ITO for sensing applications can be significantly enhanced by introducing graphene sheets due to many desirable properties such as high surface-to-volume ratio, large surface area, high electrocatalytic activity, fast electron transfer kinetics, robust mechanical properties, good film-forming ability, flexibility, and electronic conductivity(Stankovich et al. 2006). Compared to carbon nanotubes (CNTs)(Yang et al. 2011d), graphene sheets can be easily synthesized in a chemical route from inexpensive graphite(Xu et al. 2008a). Unfortunately, the existence of excessive residual defects and oxygenated functional groups in graphene can greatly affect its electronic and electrocatalytic properties(Guo et al. 2009). Thus effectively eliminating defects and oxygen contents in graphene oxide (GO), which increases the size of sp^2 domains(Eda et al. 2010), is essential to avoid any undesirable reactions and electrostatic adsorptions and provide a favorable microenvironment for further modification. Gold nanoparticles (AuNPs) are extensively used in analytical research as they offer high surface energy, strong adsorption ability, biocompatibility, enhanced electrical conductivity, and excellent catalytic activity. The AuNPs can be formed into nanocomposites with graphene sheets with synergistic results(Han et al. 2011).

Possibly the most important catecholamine, the neurotransmitter DA (4-(2-aminoethyl) benzene-1,2-diol) plays an indispensable part in the central nervous, renal, hormonal and cardiovascular systems of animals. DA has been associated with important brain functions and pathological process of neurodegenerative diseases such as Parkinson's disease(Swamy and Venton 2007). High concentration of DA can lead to abnormally high pulse and blood pressure. DA is also one kind of widespread 'lean meat powder' added to animal feed to help stocks build muscle rather than fat as an adrenergic neural stimulant. Use of DA in animal feed has been

*This work has been published: (Yang et al. 2012b)

banned in most countries, and it is essential to prevent its illegal use. Therefore detecting the presence of DA in physiological or biological samples is of great significance for both diagnostics and therapeutics. Current approaches for detecting DA include but not limit to UV-vis spectrometry, fluorescence(Yu et al. 2011a), capillary electrophoresis(Williams et al. 2002), and chemiluminescence(Swamy and Venton 2007). Electrochemical detection offers several advantages over these methods in its easiness, high sensitivity, environment-friendliness, rapidity, capability to be used in turbid or colored fluids, suitability for both *in vitro*(Koehne et al. 2011) and *in vivo*(Njagi et al. 2010) detection and most importantly, the portability to be carried out of labs with a hand-held analyzer. Some studies have been reported using different materials for detecting DA such as MWCNT-silica-AuNPs nanocomposite(Komathi et al. 2010), NiAl layered double hydroxides-graphene nanocomposites(Li et al. 2011), and a tyrosinase-immobilized carbon fiber microsensor(Njagi et al. 2010). However, these methods are complicated in terms of material synthesis and sensor preparation.

Herein we report a facile and green approach to reduce GO at room temperature without using any chemical reducing agent and subsequently synthesize AuNPs *in situ* in the carbon network. The reduction of GO was highly effective and rapid with oxygenated defective sites removed and electronic properties improved. Further modification of reduced GO sheets (rGOS) with AuNPs can enhance their electrical conductivity and electrocatalytic activity, in an electrochemically controllable process. The as-synthesized AuNPs-rGOS-ITO sensor showed extraordinary electrocatalytic activity against DA. Also, owing to its low cost and miniature size, it can be microfabricated as one-time-use disposable sensors, and thus it can eliminate complicated and laborious cleaning steps needed while using common solid electrodes. This sensor is also compatible for some lithographic approaches(Kim et al. 2004) and has the potential in microfluidic applications for DA detection.

6.2 Experimental

6.2.1 Chemicals and reagents

Graphite powder was obtained from Sinopharm Chemical Reagent. Dopamine hydrochloride, Uric acid (UA) and L-ascorbic acid (AA) were received from Acros Organics and Gold (III) tetrachloride trihydrate ($HAuCl_4 \cdot 3H_2O$) was purchased from Sigma-Aldrich. ITO-coated glass

slides (surface resistance 8 to 100 $\Omega \cdot sq^{-1}$, thickness 0.55 mm and optical transparence >85%) were acquired from Nanocs. All other chemicals were of analytical grade and used as received without further purification. High quality Milli-Q water (>18.2 MΩ) was used throughout the study. High purity N_2 was applied for deaeration where needed.

6.2.2 Instrumentation

Hitachi S-4800 (Hitachi, Japan) scanning electron microscope (SEM) was employed for characterizing surface morphology. Attenuated total reflectance-Fourier transform infrared spectroscopy (ATR-FTIR) was conducted with PerkinElmer Spectrum 100 (PerkinElmer, MA, USA). UV-vis spectra were recorded with Cary 50 Bio UV-vis spectrophotometer (Varian, CA, USA). Cyclic voltammetry (CV), differential pulse voltammetry (DPV) and amperometry were performed on a CHI 660D electrochemical analyzer (CH Instruments, TX, USA) at ambient temperature (25±1^{o}C) in a three-electrode configuration, with Pt wire counter electrode (CE), saturated Ag/AgCl (3 M KCl) reference electrode (RE) and rGOS-ITO or AuNPs-rGOS-ITO as the working electrode (WE).

6.2.3 Preparation of AuNPs-rGOS-ITO

GO was synthesized following a modified Hummer's method using graphite powder as the precursor as we previously reported(Yang et al. 2011a). Exfoliated GO can be obtained using the approach composed of pre-oxidization and oxidization steps of graphite in concentrated acidic medium. A piece of ITO sheet (5 mm x 25 mm) was sonicated successively in water, acetone, ethanol and water and dried in an oven at 50 ^{o}C. Nail enamel (epoxy resin) was used for insulation coating with an exposed surface area of 0.071±0.003 cm^2 as WE as defined by a well-cut paper cover, while leaving the upper area for electrical connection (**Scheme 6.1**). 3 μL of 1 $mg \cdot mL^{-1}$ as-prepared GO solution was drop-cast fully covering the exposed ITO surface and then dried in ambient conditions. The reduction of GO on ITO was carried out by repetitive potential sweeping from 0.0 V to -1.5 V at a scan rate of 0.1 $V \cdot s^{-1}$ in deaerated 0.05 M pH 5.0 PBS (NaH_2PO_4/Na_2HPO_4) for 100 cycles (Yang et al. 2011a), and then it was thoroughly rinsed with water and dried at room temperature. AuNPs was synthesized *in situ* in rGOS network by immersing the rGOS-ITO in a deareated 2.5 mM $HAuCl_4$ precursor solution containing 0.1 M KCl and applying a constant potential of -0.2 V for 100 s. After growth of AuNPs, rGOS-ITO was rinsed with copious water and dried under room temperature.

Scheme 6.1: Fabrication of AuNPs-rGOS-ITO dopamine sensor with a disposable working electrode.

6.2.4 Meat sample preparation and detection of lean meat powder

Beef (Angus) meat was purchased in a local market. The sample was prepared by the protein precipitation approach with $ZnCl_2$(Zaworski and Gill 1988). Briefly, 2.0 g of the beef sample was triturated and homogenized with mortar and pestle into a fine paste. It was then mixed with 10.0 mL 1M $ZnCl_2$ and aged for 10 min with occasional homogenizing. The mixture was then centrifuged at 4,000 rpm and 4^{o}C for 15 min and filtered through a Millipore Nylon filter with 0.2 µm pore size. The resulting sample was used for DA detection in PBS buffer.

6.3. Results and Discussion

6.3. 1 Characterization of AuNPs-rGOS-ITO

A typical SEM image of rGOS (**Fig. 6.1A**) exhibited the characteristic wrinkled and folded sheet structure of graphene. After electrochemical reduction, GO nanosheets were overlapped in parallel in a few layers, corrugated and crumpled into intermittent wrinkled sheet structures, which can greatly increase the surface roughness and area. These structural changes both minimize the surface energy and improve the mechanical properties such as Young's modulus and tensile strength due to sheet interlocking in nanoscale(Xu et al. 2008b). Apart from the wrinkled and folded area, the rGOS sheets appeared flat and parallel to ITO substrate surface,

indicating good film-forming ability with large surface coverage on substrate. The formation of rug-like interconnected network and the lowering of defects and oxygen content after reduction favored the conduction pathways for charge transport. The SEM of the AuNPs-modified rGOS showed that AuNPs were evenly distributed in the rGOS network (**Fig. 6.1B**), providing larger surface area, good biocompatibility, electrocatalytic activity and enhanced conductivity with additional conducting pathways for fast electron transfers(Yang et al. 2011d). The as-synthesized AuNPs were fairly uniform with diameters of 187.3±29.2 nm (**Fig. 6.1C**). It has been reported that it is hard to decorate hydrazine-reduced GO with AuNPs using the chemical citrate reduction route, because few positively-charged free Au(III) ions in the precursor solution can reach rGOS via electrostatic interactions due to the removal of most negatively-charged oxygenated groups in GO(Goncalves et al. 2009). In our approach of electrodeposition, the Au(III) ions can easily reach rGOS surface both by free and negative potential-driven diffusions for *in situ* nucleation without any aging steps. Moreover, AuNPs were distributed in fewer numbers on rGOS substrate with large inter-particle distances and tended to agglomerate to some degree, resulting in a relatively larger size. This might be caused by the electrochemically-stable unreduced oxygenated groups and local charge differences in the wrinkled rGOS during deposition, similar to what was observed in thermally-reduced GO(Goncalves et al. 2009).

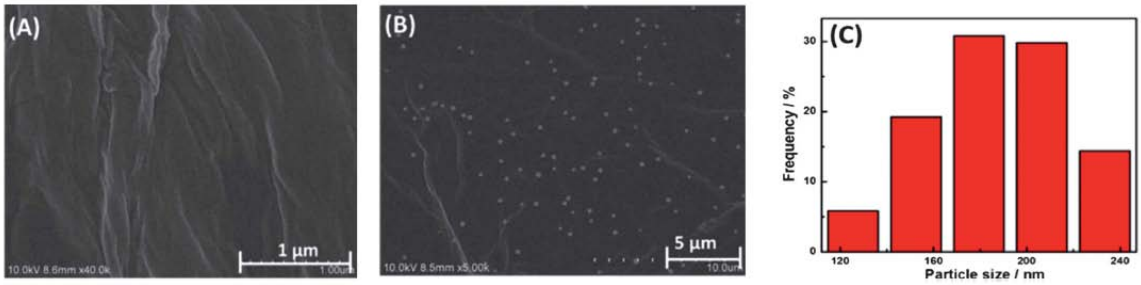

Fig. 6.1: SEM images of (A) rGOS-ITO and (B) AuNPs-rGOS-ITO. (C) Histogram of particle size distribution of AuNPs.

Repetitive CVs in a potential range from 0 to -1.5 V for electrochemical reduction of GO to rGOS on ITO are shown in **Fig. 6.2A**. A considerably large cathodic current starting at a potential of about -0.65 V with the peak at -1.35 V was observed in the first cycle, similar to the electrochemical reduction behaviors of GO on a glassy carbon electrode(Yang et al. 2011a). This overwhelming cathodic current was caused by the reduction of surface-oxygenated groups in GO, because the reduction of water to hydrogen happens at more negative potentials (i.e., -1.5

V)(Guo et al. 2009). From the second cycle on, the reduction of current decreased dramatically and dropped continuously until it completely disappeared in several more cycles and reached a plateau. These results, as well as the absence of anodic peaks, demonstrate that the entire reduction process only takes place at potentials more negative than -0.65 V on the ITO surface and is rapid, irreversible and conveniently controllable by the number of potential scans, scan rates and potential ranges. An obvious change in the color from brown to black can be seen before and after reduction of GO (**Fig. 6.2A** inset). Moreover, when the black pellet is mildly stripped off and dispersed in water, it was more poorly soluble than the unreduced GO, suggesting that the hydrophilic surface oxygen functional groups in GO were successfully removed after reduction, which affords enhanced stability for electrochemical applications.

ATR-FTIR transmittance spectra of bare ITO, GO-ITO and rGOS-ITO are shown in **Fig. 6.2B** to evaluate the effect of reduction. In all samples, a strong band around 890 cm^{-1} is seen, which could be associated with Si-O-Si stretching vibration involving an O-M bridging, while the other obvious band around 770 cm^{-1} could be ascribed to Si-O-M stretching vibration(Sidorov 1967). Meanwhile, a shoulder band seen at 1150 cm^{-1} in ITO and GO-ITO shifted to 1220 cm^{-1} in rGOS-ITO. This is related to the antisymmetric vibration mode of Si-O-Si(Sidorov 1967), and the shift might be attributed to the cathodic polarization during reduction of GO. This band might also overlap with C-OH stretching band in rGOS-ITO, if there were any remaining reduced C-OH groups. The presence of a number of different oxygen functionalities in GO results from the successful oxidation of graphite (**Fig. 6.2B** b): a broad and intense band centered at 3400 cm^{-1} of O-H stretching vibration (intercalated water), another overlapping broad and strong band at 3200 cm^{-1} of O-H coupling stretching vibration (carboxylic acid), a sharp peak at 1740 cm^{-1} of C=O stretching vibration (carbonyl), a weak band at 1420 cm^{-1} of O-H deformation vibration (carboxyl), a weak band at 1220 cm^{-1} for C-OH stretching vibration (alcohol), and a shoulder band at 1060 cm^{-1} of C-O stretching vibration (epoxy or alkoxy), similar to those previously reported(Xu et al. 2008c). The C=C band at 1620 cm^{-1} was caused by skeletal vibrations of unoxidized graphitic domains (Guo et al. 2009). After reduction, bands of O-H stretching at 3400 cm^{-1} (due to the hydrophobicity of rGOS), O-H deformation at 1420 cm^{-1}, and C-O stretching at 1060 cm^{-1} completely disappeared in rGOS (**Fig. 6.2B** c) while intensities of bands of O-H stretching at 3200 cm^{-1} and C=O stretching vibration 1740 cm^{-1} greatly decreased, suggesting GO was efficiently reduced with most oxygenated groups eliminated. Moreover, the C=C skeletal vibrations of unoxidized graphitic bands increased in intensity and shifted to lower

wavenumbers, indicating that the resulting rGOS has high purity. Compared to chemical reduction with hydrazine, in which carboxyl groups could not be well removed and even cause sharper characteristic bands(Li et al. 2008b), the electrochemical reduction of GO turns out to be a quick, effective, inexpensive and green approach.

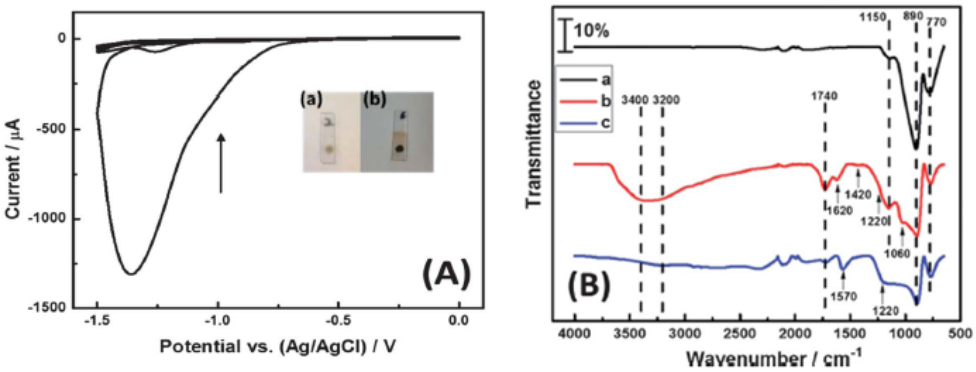

Fig. 6.2: (A) Cyclic voltammograms of GO-modified ITO in deaerated 0.05 M pH 5.0 PBS (100 cycles with initial potential of 0.0 V), the arrow shows the progression of cycling. Scan rates: 100 $mV \cdot s^{-1}$. Insets show GO-modified ITO (a) before reduction and (b) after reduction. (B) ATR-FTIR spectra of (a) bare ITO, (b) GO-ITO and (c) rGOS-ITO.

6.3.2 Electrocatalysis of AuNPs-rGOS-ITO sensor against DA

The electrocatalytic activity of AuNPs-rGOS-ITO against DA was investigated by CV (**Fig. 6.3**). In the absence of DA, rGOS-ITO did not exhibit any obvious peaks due to reduction (*c*). However, with AuNPs-rGOS-ITO, there was an increase in background current with a pair of weak redox peaks around +0.14 V and +0.31 V, respectively which should be due to the redox reactions of deposited Au species in rGOS scaffold (*a*, pair of arrows). This electrochemical process starts from surface adsorption of water molecule and/or electrosorption of hydroxyl ions, and AuOH forms as potentials go more positively(Akbari-adergani et al. 2010), resulting in the formation of gold oxide with strong eletrocatalytic activities (Eqs. 1 and 2). With addition of 0.1 mM DA, there was only a minor increase in the anodic current at rGOS-ITO (d) whereas a pair of sharp redox peaks with different peak intensities, resulting from redox reaction of DA (Eq. 3), was found around +0.18 V and +0.22 V at AuNPs-rGOS-ITO (*b*). This demonstrates the excellent electrocatalytic performance of AuNPs-rGOS-ITO against DA, owing to its large surface area and electrochemically active sites. During this process, peak A (*b*) corresponds to the oxidation of DA into open-chain quinine and the other peak B (*b*) relates to reduction of quinine back to DA(Venton and Wightman 2003). From the second cycle on, an additional oxidation peak C (*e*) at

more positive potential appeared, which is presumed to be oxidation of an unknown compound formed in the first cycle according to Wang et al.(Wang et al. 2002). Meanwhile, another pair of redox couples (oxidation peak around -0.25 V and reduction peak around -0.28 V), corresponding to dopaminechrome (transformed from dopaminequinone via intramolecular cyclization)-leucodopaminechrome, was found (data not shown) in a wider potential window, similar to the reported data(Wang et al. 2002; Zhao et al. 2001). Noticeably, the intensities of peaks A and B greatly decreased in the second cycle. However, this would not be an issue for the detection since the oxidation of DA is rapid and stable current can be achieved quickly, which can also be seen in the amperometric responses (**Fig. 6.5B**). The whole electrochemical process of DA at AuNPs-rGOS-ITO can be summarized as shown in equations below(Bernsmann et al. 2011; Wang et al. 2002). With intensive repetitive CV scans, the originally colorless DA solution obviously turned yellowish-red and then black (**Fig. 6.3** inset). The yellowish-red product is dopaminechrome and the black polymeric material is melanin, the formation of which undergoes a number of complicated pathways(Bernsmann et al. 2011).

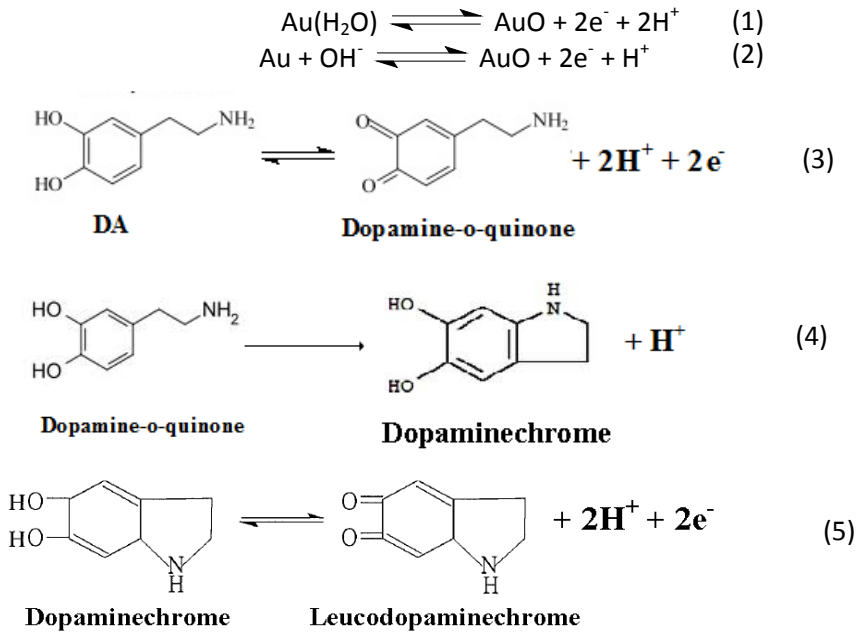

Fig. 6.3: Cyclic voltammograms of AuNPs-rGOS-ITO (a, b) and rGOS-ITO (c and d) electrodes in 0.05 M pH 7.0 PBS in the absence (a and c) or presence (b and d) of 0.1 mM DA. (e) is the second cycle of AuNPs-rGOS-ITO in 0.05 M pH 7.0 PBS containing 0.1 mM DA, scanning from +0.6 V. Insets show the color change

of DA during potential cycling. Scan rates: 100 mV·s^{-1}.

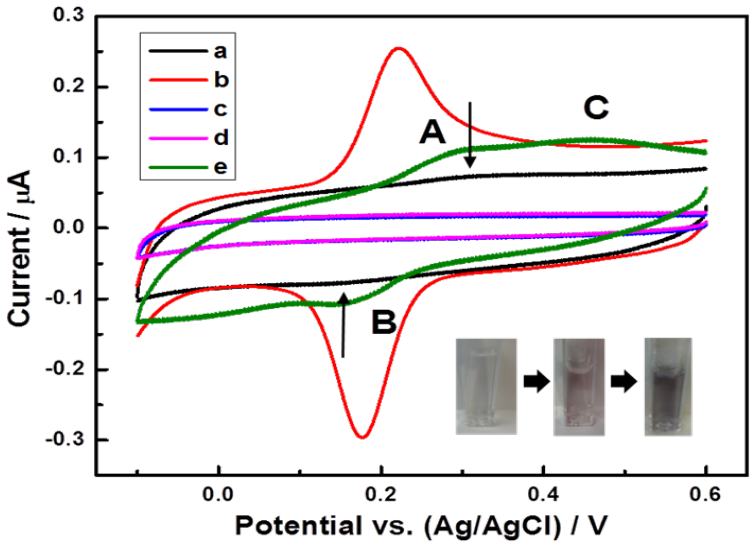

The influence of scan rates (ν) on the electrochemical response of 0.1 mM DA at AuNPs-rGOS-ITO was examined by varying scan rates from 10 to 400 mV·s^{-1} (**Fig. 6.4A**). As the scan rate increased, both anodic and cathodic peak currents increased gradually while anodic and cathodic peak potentials slightly shifted to more positive and negative potentials respectively, generating increased potential separations (ΔE_p). A good linear dependence of redox peak currents on scan rate, but not its square root, was found in the range of scan rates (**Fig. 6.4A** inset; linear regression equations (both with R=0.9985):

Ipa (μA)=1.2121x10^{-3}*ν (mV·s^{-1}) + 9.7472x10^{-3}

Ipc (μA)=-1.3163x10^{-3}*ν (mV·s^{-1})-8.2362x10^{-4}

Integration of the area under anodic peaks led to really close charge values (Q) independent of scan rate. These results signify the electrochemical reaction is controlled via surface adsorption of DA molecules(Yin et al. 2010a). As for a quasi-reversible adsorption-controlled process, surface coverage concentration of redox species (Γ) and the number of electrons (n) can be acquired according to Laviron's equation(Laviron 1974, 1979):

$$I_p = \left(\frac{n^2F^2}{4RT}\right) A\Gamma\nu = \frac{nF}{4RT} Q\nu \qquad (6)$$

Where, A is the electrode surface area, F is Faraday's constant, T is temperature, R is ideal gas constant. From **Fig. 6.4A**, Q is calculated to be 6.189x10^{-8} ±2.653x10^{-9} C and together with the

slope, n is calculated to be 2.012 ±0.4118, indicating a two-electron and two-proton process(Medintz et al. 2010) at the sensor interface consistent with Eq. 3. The surface concentration (Γ) of DA can be obtained as 4.51x10^{-12} ±5.06x10^{-13} mol·cm^{-2}. When ν is more than 150 mV·s^{-1}, ΔE_p is close to or larger than 100 mV. The relationship between redox peak potentials and ln v was also built (**Fig. 6.4B**) and linear dependence can be found at higher scan rates from 150 to 500 mV·s^{-1}, expressed as:

E_{pa} (V)=0.0218*lnν (V·s^{-1})+0.2886 (R=0.9923)

E_{pc} (V)=-0.0236*lnν (V·s^{-1})+0.1154 (R=0.9900)

which can be represented by Lavrion models(Laviron 1979):

$$E_{pa} = E^{o''} + \frac{RT}{(1-\alpha)nF}\ln\frac{(1-\alpha)Fn}{RTk_s} + \frac{RT}{(1-\alpha)nF}\ln\nu \quad (7)$$

$$E_{pc} = E^{o''} - \frac{RT}{\alpha nF}\ln\frac{\alpha Fn}{RTk_s} - \frac{RT}{\alpha nF}\ln\nu \quad (8)$$

Therefore, from the slopes, the electron transfer coefficient α is estimated to be 0.478, close to the theoretical value of 0.5 for a quasi-reversible process. From Eqs. 7 and 8, it can be obtained:

$$\Delta E_p = \frac{RT}{(1-\alpha)\alpha nF}\left[\alpha\ln(1-\alpha) + (1-\alpha)\ln\alpha - \ln\frac{RT}{nF} - \ln k_s\right] + \frac{RT}{(1-\alpha)\alpha nF}\ln\nu \quad (9)$$

From the intercept of the dependence of ΔE_p on $\ln\nu$ (**Fig. 6.4B** inset, R=0.9976), the apparent heterogeneous electron transfer rate constant k_s can be obtained as 1.456 ±0.034 s^{-1}, indicating a fairly fast electron transfer during the electrocatalytic reaction.

Fig. 6.4: (A) Cyclic voltammograms of AuNPs-rGOS-ITO in 0.05 M pH 7.0 PBS containing 0.1 mM DA at different scan rates of 10, 20, 40, 60, 80, 100, 150, 200, 250, 300, 350 and 400 mV·s^{-1} (from inside to outside). Inset shows the plots of anodic and cathodic peak currents vs. scan rates. (B) The plot of peak potentials (E_p) on neperian logarithm of scan rates (*ln*(ν)), with linear fitting from scan rates 150-500 mV·s^{-1}. Inset shows the dependence of peak potential separation (ΔE_p) on *ln*(ν).

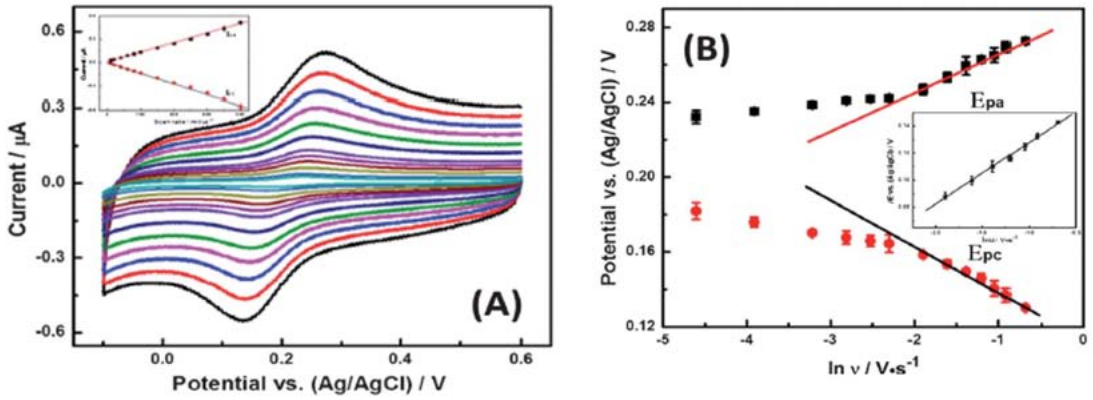

6.3.3 Detection of DA at AuNPs-rGOS-ITO

Since the electrocatalytic reaction at AuNPs-rGOS-ITO sensor is a two electron and two proton process (Eq. 3), the pH value should have a great impact in amperometric responses. As in **Fig. 6.5A**, the amperometric responses increased with pH from 5.9 to 8.0, because high pH can potentially drive the reaction forward more favorably. Noticeably, while the amperometric responses increased almost linearly from pH 6.5 to 8.0, the current responses were extremely low at pH 5.9 or lower (data not shown) making it unsuitable for detections at extreme low pH. With regard to the convenience and practical applications, pH 7.0 which is close to physiological levels was used in the study.

The amperometric responses to DA at AuNPs-rGOS-ITO sensor were investigated with stepwise increases in concentration by 0.1 mM (b) and 0.5 mM DA (a), respectively (**Fig. 6.5B**). Obvious stepwise increases in current could be observed with successively increasing concentrations of DA. Interestingly, at higher DA concentrations, the initial current was considerably large, which then slowly decreased until steady-state was achieved in 10 s. This phenomenon is caused by high instant local concentration at the sensor interface under mild stirring after addition and also the current decrease right after the first run, as observed in CV (**Fig. 6.3**). The current response is linearly proportional to the DA concentration with 4.5 mM as the upper detection limit (**Fig. 6.5C**), and the two calibration lines nearly overlapped (the calibration curve for 0.5 mM stepwise is I (μA)=0.5604+1.4216*C (mM), R=0.9932). So the detection sensitivity is 20.11 $\mu A \cdot mM^{-1} \cdot cm^{-2}$. Meanwhile, DA was also determined by DPV due to its higher sensitivity and minimization of any noises from stirring. When DA was absent, there

was a negligible and broad peak at +0.25 V due to Au species (**Fig. 6.6A** black). In the presence of DA, while no obvious peak was observed at rGOS-ITO in response to DA (**Fig. 6.6B** inset a), a well-defined sharp peak centered around +0.20 V can be seen at AuNPs-rGOS-ITO. A linear relationship of peak current and DA concentration (**Fig. 6.6A** inset) can be established as I (μA)=1.5919x10^{-4}+4.4355x10^{-3}*C (μM) (R=0.9994) from 10 to 1000 μM, with sensitivity of 62.74 μA·mM^{-1}·cm-^{2}.The detection limit (DL) is determined to be 6.0x10^{-8} M (at signal/noise=3), based on the following equation where σ is the standard deviation of three measurements and S is the slope of the calibration line:

$$DL = \frac{3\sigma}{S} \qquad (10)$$

Fig. 6.5: (A) pH effects on amperometric responses of AuNPs-rGOS-ITO sensor against 0.1 mM DA in 0.05 M PBS. (B) Amperometric responses of AuNPs-rGOS-ITO sensor in 0.05 M pH 7.0 PBS with stepwise addition of 0.1 (a) and 0.5 mM DA (b) in a time period of 50 s. Applied potential: +0.3 V. (C) Dependence of current responses at AuNPs-rGOS-ITO sensor on DA concentrations of 0.1 mM (■) and 0.5 mM (●) per drop, the dotted line shows linear fitting.

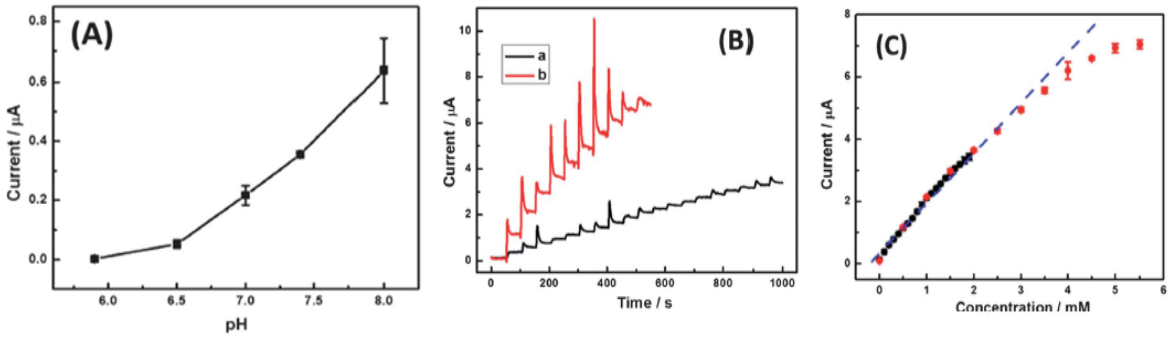

6.3.4 Sensing performance compared with UV detection

Since DA strongly absorbs light in the UV region with a well-known signature peak maximized at 280 nm, the UV-vis spectrophotometry is considered a useful tool for the detection of DA in matrices without UV absorbing compounds. Typical UV absorption spectra of DA in various concentrations are shown in **Fig. 6.6B**, clearly displaying distinct peaks at 280 nm. A good linear relationship was established for the absorbance peak intensity vs. DA concentration from 0.1 to 1.0 mM (R=0.9982). However, besides its inability to detect DA in the presence of UV-absorbing species, the dynamic working range was also poor (**Fig. 6.6B** inset)

when compared to 4.5 mM upper limit of our sensor, making it unsuitable to quantify DA at concentrations higher than 1.5 mM. However, an excellent correlation (R=0.9973) was found between the AuNPs-rGOS-ITO sensor and UV-vis spectrophotometry (**Fig. 6.6C**). Therefore, this sensor can be a supplement to or a substitute for the conventional UV detection, especially for dilution-free high DA concentrations and in presence of UV-vis absorbing species in biological or physiological samples at wavelengths nearby (such as nucleic acids, certain vitamins and proteins with peaks around 280 nm).

Fig. 6.6: (A) DPVs of AuNPs-rGOS-ITO sensor in 0.05 M pH 7.0 PBS containing 0, 10, 20, 30, 50, 80, 100, 200, 400 and 1000 µM DA (the arrow indicated increasing concentrations). Inset shows the linear dependence of peak currents on DA concentrations. (B) UV-vis spectra of 0.1, 0.2, 0.3, 0.5 and 1.0 mM DA (the arrow indicated increasing concentrations). Inset shows the absorbance dependence on concentration of DA with the dotted line for linear fitting. (C) Linear correlation of UV-vis detector with our as-prepared sensor.

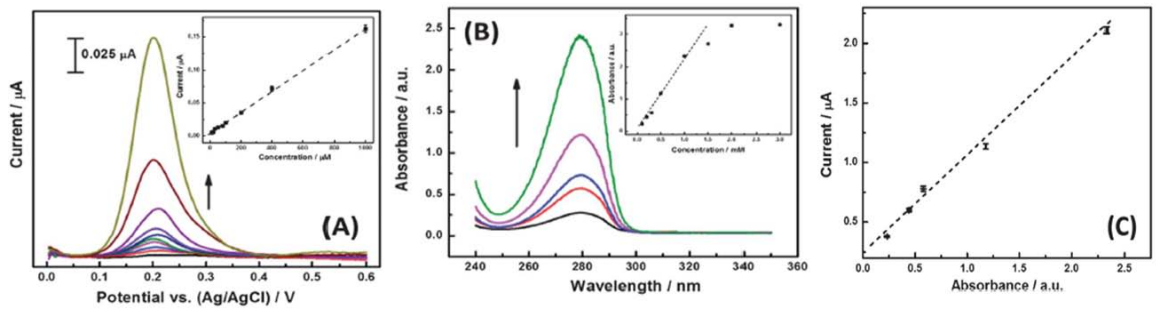

6.3.5 Sensor stability, selectivity and performance in beef samples

Although we designed the AuNPs-rGOS-ITO sensor primarily for low-cost one-time use, its reproducibility was tested by measuring 0.1 mM DA. After the signal was stable, the relative standard deviation (RSD) for five consecutive measurements using the same sensor is 3.17 %, while the RSD for three sensors fabricated under the same conditions was 6.47 %, indicating a reasonable reproducibility. After being stored away from air under room temperature for one week, there was a minimal loss in sensitivity of 7.65 %, showing great stability.

The effect of the presence of oxidizable compounds such as AA and UA that commonly coexist with DA in physiological or biological samples was evaluated. In amperometric detection, there was an obvious current increase after addition of DA. However, AA can elicit a 22.8% current change of the DA current signal (**Fig. 6.7A**), exhibiting interference to some extent,

though the detection potential is only as low as +0.3 V. Despite UA nearly causes zero interference, amperometry with the sensor is reluctant for applicable uses on any samples potentially containing high concentrations of AA. In this case, the sensor could be improved by coating with an outer selective membrane or doping with other catalyst by using amperometry. In contrast, DPV in the mixture of DA, AA and UA in equal concentrations produced nearly the same current-potential pattern as that of DA (**Fig. 6.7A** inset). There are no additional peaks observed in the screening range, because AA and UA are known to be oxidized out of the pulsed potential range by AuNPs(Yin et al. 2010b). Furthermore, most of the common ions in beef such as K^+, Na^+, Mg^{2+}, Zn^{2+}, Cl^-, NO_3^-, SO_4^{2-}, $H_2PO_4^-$, and HPO_4^{2-} did not interfere with the detection under 20-fold concentration for both amperometry and DPV, all with current changes less than 4.68%.

The data from analyzing the meat samples indicated that there was no DA present, as would be expected in commercial samples sold in the USA. Furthermore, the meat sample analysis was a good indication that real food matrices do not interfere with the peaks of DA in CV and DPV (there are no additional peaks but a slight increase in background current at higher positive potentials) as well as UV-vis spectra. The UV-vis results (data not shown) in the UV region without peaks around 280 nm imply the absence of tryptophan and tyrosine, resulting from the successful removal of proteins in the filtrates during sample preparation. However, there was a strong absorbance peak at 250 nm (data not shown), which might be attributed to the abundant vitamin species in beef such as E, B1, B2 and B12, with peaks around this wavelength. Meanwhile, in spite of little interferences observed using DPV and CV, the beef sample causes a huge amperometric current in i-t curves, similar to **Fig. 6.7A**, possibly due to the presence of large amount of vitamins. When beef samples were spiked with 50, 100 and 500 µM DA, the sensor exhibited acceptable detection accuracy of greater than 91 % (**Fig. 6.7B**). Thus, the sensor can be used to detect DA using DPV in real matrices with good sensitivity, reproducibility, stability and little interferences from UA and AA. In our future work, we will examine the sensor performance in pharmaceuticals containing dopamine as well as the incorporation of the sensor into a microfluidic device built on glass sides to achieve possible lab-on-glass detection.

Fig. 6.7: (A) Interference study of AuNPs-rGOS-ITO sensor operated under amperometry mode in 0.05 M pH 7.0 PBS at -0.3 V with sequential addition of 0.1 mM DA, 0.05 mM AA and 0.05 mM UA. Inset shows DPVs of rGOS-ITO (a) and AuNPs-rGOS-ITO (b and c) in 0.05 M pH 7.0 PBS containing 0.1 mM in the absence (a and b) or presence (c) of 0.1 mM AA and UA. (B) Pretreated beef sample detection by DPV with spiked DA (n=3) (a) spiked (b) detected.

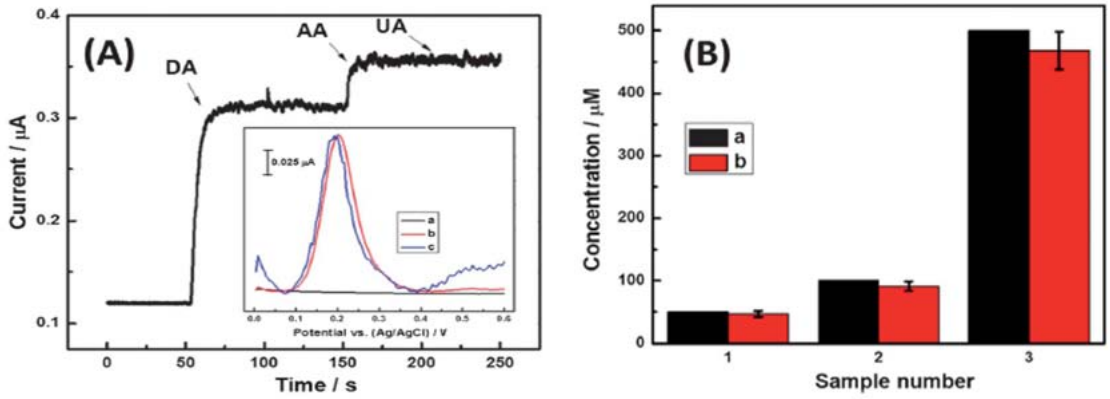

6.4 Conclusions

We have reported the fabrication of a disposable DA sensor based on synthesis of AuNPs-rGOS nanocomposites on ITO through an inexpensive, easy, and green electrochemical route. The results show that GO nanosheets were efficiently oxidized directly on ITO surface to form a wrinkled and folded interconnecting network with its oxygen contents largely removed. Further electrochemical modification generated uniformly dispersed AuNPs with good electrocatalytic activity by forming Au oxides in the reaction. The as-prepared AuNPs-rGOS-ITO sensor displayed satisfactory sensitivity, wide working range, stability, and selectivity against DA. The sensor results correlated well with those obtained using the conventional UV technique. It was also capable of detecting DA in real food matrices.

Chapter 7: Electrochemical detections of food additive H_2O_2 using Fe_3O_4 mimetics peroxidase thin film electrodes*

7.1 Introduction

Rapid, sensitive, and accurate determination of H_2O_2 has become a major concern not only because it is a by-product of several important oxidases, but also because it serves as a significant mediator in food, clinical, industrial, pharmaceutical, and environmental products (Tan et al. 2009). Though widely used in applications such as aseptic packaging, antimicrobial wound treating, disinfecting, dental bleaching, food processing etc., H_2O_2 is not entirely safe. Industrial strength H_2O_2 is a strong oxidizer and is able to corrode eyes and skin, causing irreversible damage. H_2O_2 found in the eye lens and aqueous fluid, at concentrations only slightly higher than normal physiological levels, produced a significant number of DNA single-strand breaks in lens epithelial cell cultures (Spector et al. 1989) and tissue damage (LopezOngil et al. 1996) including blindness. If consumed in excess, H_2O_2 can induce potentially life-threatening neurological reactions and damage to the upper gastrointestinal tract (Humberston CL 1990). Health Canada and US Food and Drug Administration (FDA) have issued a warning in 2006 against human consumption of H_2O_2.

Current methods to detect H_2O_2 such as titrimetry, chemiluminescence, and spectrometry suffer from several shortcomings (Lei et al. 2003). For instance, they are often laborious, time-consuming, lab-based, costly in devices or consumables such as enzymes, and require trained individuals to perform the test. Electrochemical approaches for detecting various analytes have received extensive attention in recent years due to their low cost, high sensitivity, fast response, accuracy, capability of operating in the presence of optically-interfering substances etc. (Grieshaber et al. 2008a). Enzyme-based (i.e., horse radish peroxidase, HRP) (Yuan et al. 2008) and enzymeless electrochemical H_2O_2 sensors (Hsu et al. 2008) are very popular. However, there are intrinsic drawbacks of enzyme-based sensors such as complicated preparation steps, poor reproducibility, stringent operating conditions (pH, temperature, humidity, ionic strength etc.), high cost and most importantly unsuitablity for mass production (Li et al. 2009a; Wilson and Turner 1992), which limit their applications.

In contrast, enzymeless sensors are mostly based on metal, metal oxides or hybrid materials. Cao et al. synthesized Co_3O_4 nanoparticles and used them in H_2O_2 sensing (Cao et al.

*This work has been published: (Yang et al. 2011c)

2008). Y. Tian's group successfully detected cellular H_2O_2 from living cancer cells based on ZnO nanosheets (Tian et al. 2010). Chakraborty et al. used Pt nanoparticles in H_2O_2 electrochemical sensing (Chakraborty and Retna Raj 2009). A H_2O_2 sensor has also been fabricated using layer-by-layer assembled Fe_3O_4 nanoparticles and poly(diallyldimethylammonium chloride) (PDDA) through the electrostatic interaction (Zhang et al. 2008a). Though good analytical performances have been achieved, these nanomaterial-based sensors are expensive and are difficult to mass produce for a wide range of applications. Therefore, developing simple, facile, and reliable enzymeless H_2O_2 sensors is a pressing need. Thin-film technology offers such advantages as low cost, simple synthesis, high durability, good electric properties, and possibility of mass manufacturing of high quality sensors (Yu and Zhou 1995). For example, gold (Au) thin film as working electrodes for amperometric detection has already been commercialized and widely employed in high performance liquid chromatography (HPLC), microfluidics, and other techniques.

Herein, we report an approach to synthesize thin film of epitaxially-grown Fe_3O_4 with columnar grain structures in orientations of (001) on correspondingly-oriented TiN-buffered substrates by DC magnetron reactive sputtering and its usefulness in electrochemical H_2O_2 sensing. Fe_3O_4 is an artificial peroxidase mimetic with similar intrinsic activity to natural peroxidases but can hardly be inhibited or digested by proteases and other enzymes (Gao et al. 2007; Wei and Wang 2008). Fe_3O_4, the most stable iron oxide, is a ferromagnetic compound with inverse spinel structure and has been widely used as electrode materials with an electrical conductivity dramatically higher ($x10^6$ times) than that of ferric oxide (Fe_2O_3), resulting from fast electron exchange between Fe(II) and Fe(III). The as-developed enzyme-free electrochemical sensor based on epitaxially-grown crystalline Fe_3O_4 thin film (140-nm thick) we synthesized is simple, stable, rapid, highly sensitive for H_2O_2 sensing and suitable for mass production.

7.2 Materials and Methods

7.2.1 Materials

D(+)-glucose, D(+)-maltose, β-D-lactose, L-ascorbic acid (AA), uric acid (UA), dopamine (DA), D-fructose, sucrose and mannose (from Alfa Aesar); bovine serum albumin (BSA) (from Fisher Scientific); histamine, caffeine and casein (from Acros Organics); xanthan gum (from MP Biomedicals); and β-lactoglobulin (from Sigma Aldrich) were purchased. All other reagents were

of analytical grade and used without further purification. Food and medical samples for testing were purchased from local supermarket and they were centrifuged as needed. High quality deionized Milli-Q water (resistivity=18.2 MΩ) was used throughout the experiments. N/Phos type Si wafer with (001) orientation and resistivity 1 to 20 Ω·cm (Wafer World Inc., FL, USA) was used as the substrate for material synthesis.

7.2.2 Instrumentation

X-ray diffraction (XRD) patterns were recorded using X'Pert RPO MRD high resolution diffractometer (PANalytical Inc., MA, USA) with Cu Kα radiation (λ=0.15406 nm) at scanning rate of 4° min^{-1} and 2θ ranging from 30° to 90°. Surface morphology of the Si(001)/TiN/Fe_3O_4 was characterized by atomic force microscope (AFM) (Digital Instruments Inc., CA, USA). The magnetization hysteresis loops of the films were measured at room temperature by vibrating sample magnetometry (VSM) while the chemical states of Fe were confirmed by PHI 5400 x-ray photoelectron spectroscopy (XPS) (RBD Instruments Inc., OR, USA). Attenuated total reflectance-Fourier transform infrared spectroscopy (ATR-FTIR) was conducted with PerkinElmer Spectrum 100 (PerkinElmer, MA, USA). Chromatography analysis was performed using Dionex ICS-3000 HPLC system (Dionex Corporation, MA, USA) equipped with Supelcogel C-610H column at 30 °C and UV detector at 210 nm. Eluent was 0.1 % phosphoric acid at a rate of 0.7 mL/min and H_2O_2 was eluted with a peak at about 13.8 min under these conditions.

All electrochemical measurements, including electrochemical impedance spectroscopy (EIS), were performed using a CHI 660D Electrochemical Analyzer (CH Instrument Inc., Austin, TX, USA). A conventional three-electrode configuration was used with Pt wire counter electrode, saturated Ag/AgCl (3 M KCl) reference electrode and Fe_3O_4 or TiN-buffered Si(001) electrodes as the working electrode. All potentials were referenced to the Ag/AgCl (3M KCl) electrode. 100 mM KCl solution containing equimolar $[Fe(CN)_6]^{4-/3-}$ redox probes was used as supporting electrolyte for EIS with applied frequencies from 0.1 Hz to 100 kHz under open circuit potentials. Equivalent circuit and simulation data fitting were achieved using ZVIEW 2 software. All measurements were carried out at room temperature (25±1 °C). Temperature control was monitored real-time by Traceable® Ultra™ thermometer from Fisher Scientific.

7.2.3 Preparation of epitaxially-grown Fe_3O_4 electrode

Si(001) substrate was cleaned using 3:1 of H_2SO_4:H_2O_2 for 10 min at 90 °C to remove any organic contaminants and subject to etch by 10 % hydrogen fluoride (HF) solution for one minute to eliminate oxides on the surface. Synthesis of multi-layered stacks of substrate/TiN/Fe_3O_4 was conducted by DC magnetron reactive sputtering with a home-built system under base pressure better than 2.0 x 10^{-7} Torr, following recently reported procedures (Xiang et al. 2010a; Xiang et al. 2010b) with minor modifications. Briefly, 10-nm thick stoichiometric TiN buffer layer was first reactively sputtered on 3 mm x 3 mm Si(001) substrate (geometric area = 0.09 cm^2) in a mixed atmosphere of Ar and N_2 at the substrate temperature of 550 °C for 30 s at 250 W, which is required for epitaxial growth of Fe_3O_4 to eliminate any reactivity with Si substrate at high temperature. After cooling to room temperature, epitaxial crystalline Fe_3O_4 was deposited on the TiN layer under DC sputtering power of 60 W at 300 °C for 10 min under Ar and O_2,. The deposition procedure was repeated once more to obtain a 140-nm-thick Fe_3O_4 thin film with epitaxial columnar grains. The substrate with Fe_3O_4 was fabricated as an electrode by connecting it to the surface of a glassy carbon electrode (GCE) with Flash-Dry™ conductive silver paint (SPI Supplies/Structure Probe Inc., PA, USA) with edges carefully insulated with fast-dry nail enamel (Maybelline, USA). The TiN-buffered substrate was processed in the same way as a comparison.

7.3 Results and Discussion

7.3.1 Characterizations

Surface morphology of the epitaxially-grown crystalline Fe_3O_4 is shown in **Fig. 7.1**, the surface of the 10-nm-thick TiN-buffer layer is flat, smooth, and uniform (**Fig. 7.1A**), while the surface of the 140-nm-thick Fe_3O_4 is apparently rougher with island structures composed of epitaxial columnar grains (**Fig. 7.1B**) in fairly homogeneous height profiles. These columnar grains evolve from the island nuclei formed from the initially-sputtered Fe_3O_4 layer and coalesce into larger column-like structures with increasing film thickness (Xiang et al. 2010b). These grain-oriented needle-like columnar structures can greatly increase the surface roughness and effective surface area, making it an ideal material for sensing purposes.

Fig. 7.1: AFM images of (A) TiN-buffered substrate and (B) Fe_3O_4.

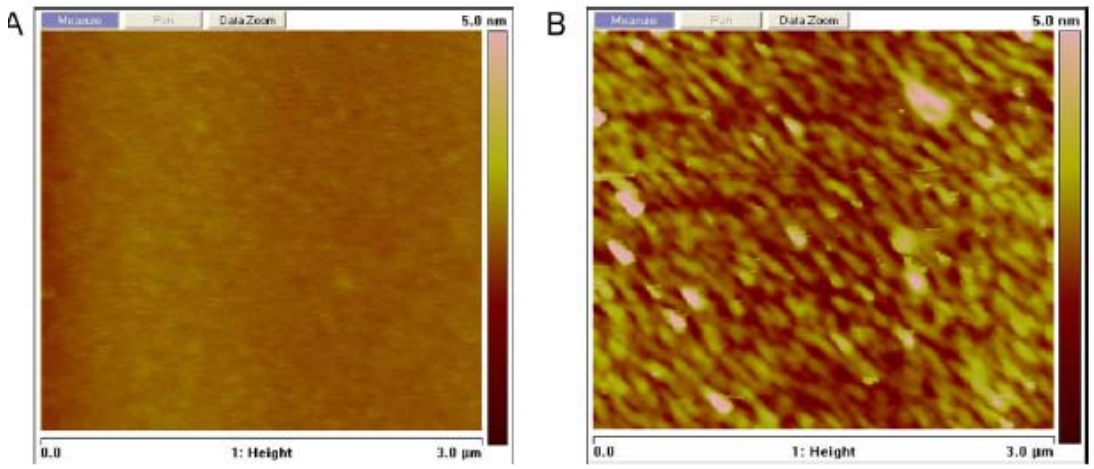

Typical XRD profile of the as-synthesized epitaxial Fe_3O_4 on TiN-buffered Si(001) substrate is displayed in **Fig. 7.2A**. A sharp and intense peak at 2Θ=69.1° is attributed to the Si (004) from the Si(001) substrate (JCPDS 65-1060). Another comparatively broad peak was observed at 2Θ of around 43°. This peak is also observed for the TiN-buffered substrate, though not as broad as that for Fe_3O_4 on TiN-buffered substrate, indicating it should be indexed as TiN (002) at 2Θ=42.6° (JCPDS 65-0715), as reported previously (Ji et al. 2008). However, since the lattice parameter of Fe_3O_4 (a=0.840) is almost twice as that of TiN (a=0.424), it is quite likely that the peak of Fe_3O_4 (004) at 2Θ=43.1° (J CPDS 65-3107) overlaps with that of TiN (002), producing a broader peak than that for pure TiN. This result cannot confirm the presence of Fe_3O_4, but can well exclude presence of any other iron oxide species such as FeO and Fe_2O_3 without their signature peaks observed.

Fig. 7.2: (A) XRD patterns of Fe_3O_4 on TiN-buffered Si substrate. # indicates reflections of Si and * indicates the overlapped peaks from Fe_3O_4 and TiN. (B) High resolution XPS spectra of Fe 2*p* region of Fe_3O_4. (C) Magnetic hysteresis loops of Fe_3O_4. (D) ATR-FTIR spectra of TiN-buffered substrate (a) and Fe_3O_4 (b). (E) EIS spectra of TiN-buffered substrate (■) and Fe_3O_4 (●) in 100 mM KCl containing 10 mM $K_4[Fe(CN)_6]/K_3[Fe(CN)_6]$. Dotted lines indicate the simulation results to fit the experimental data, and the inset shows equivalent circuit of Fe_3O_4. R_s: solution resistance, R_{ct}: electron transfer resistance, C_{dl}: double layer capacitance, Z_w: Warburg impedance.

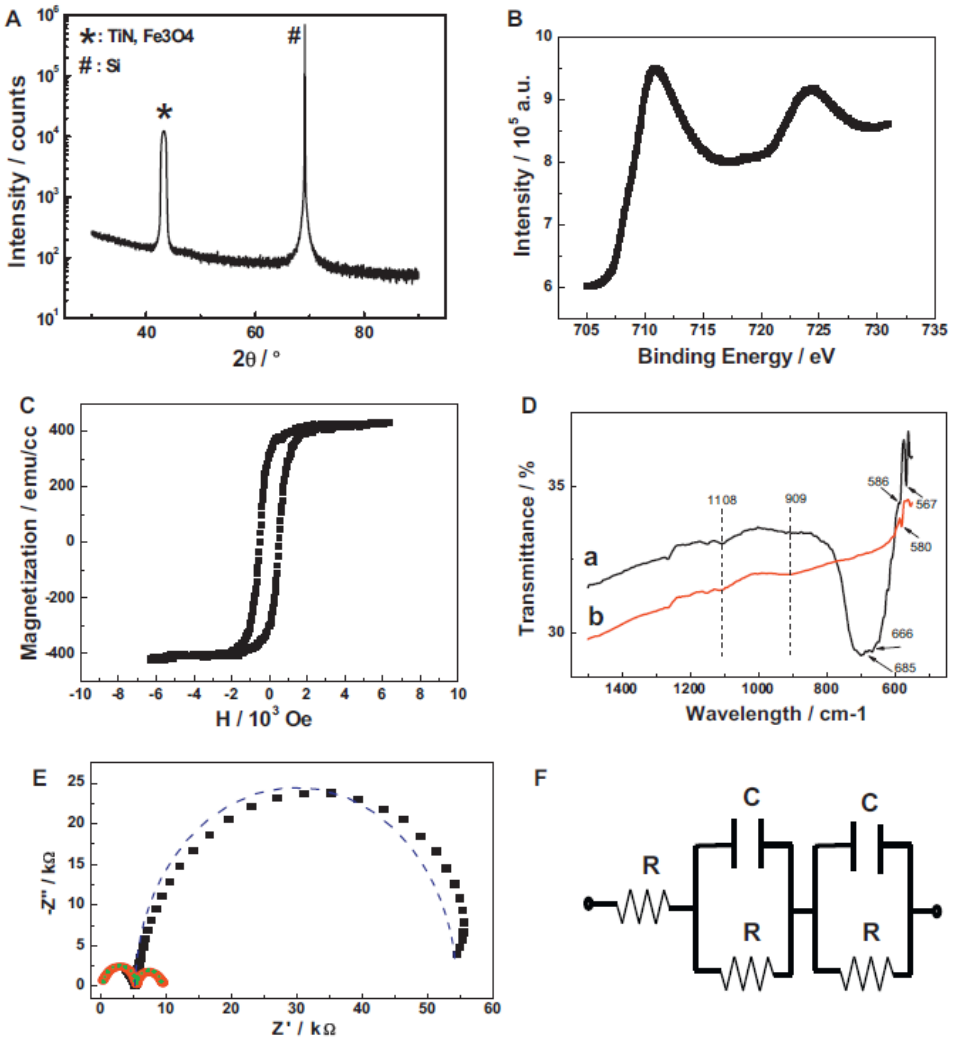

XPS was employed to further confirm the valence state of the synthesized iron oxides. A high resolution spectrum in the Fe 2*p* region is shown in **Fig. 7.2B**. Two peaks observed at binding energies of 710.9 and 724.4 eV, are assigned to Fe $2p_{3/2}$ and $2p_{1/2}$ respectively, consistent with published literature (Liu et al. 2010). It demonstrates the coexistence of Fe^{3+} and Fe^{2+} valence states from Fe_3O_4 and eliminates possible existence of other iron oxide species also with regards to XRD data. As a result, it can be further confirmed the peaks of TiN and Fe_3O_4 do overlap in XRD profiles, indicating epitaxial Fe_3O_4 (004) was successfully grown on TiN-buffered substrate.

Fe_3O_4 is marked and distinguished from other iron species by its well-known outstanding magnetic properties. Inherent magnetic properties of the epitaxial Fe_3O_4 thin film were investigated by the magnetic hysteresis loops measured by VSM at room temperature (**Fig. 7.2C**). The as-synthesized Fe_3O_4 film displayed strong ferrimagnetic behavior with coercivity of about 500 Oe and saturation magnetization greater than 430 emu cc^{-1} which is not even completely saturated in the range investigated, as a typical phenomenon of epitaxially-grown Fe_3O_4 film (Margulies et al. 1996). The ferromagnetism is reported to be closely associated with anisotropy, arising from the anti-parallel spins with different types and unequal magnitudes of Fe^{2+} and Fe^{3+} cation sites in the interpenetrating sublattices separated by O^{2-} ions (Zhang et al. 2011c). This demonstrates the successful synthesis of Fe_3O_4 with distinct magnetic properties, which may be useful in practical applications.

ATR-FTIR spectra of TiN-buffered substrate and Fe_3O_4 are shown in **Fig. 7.2D**. The band at 1108 cm^{-1} is assigned to Si-O-Si while one at 909 cm^{-1} to Si-O-Ti is also present (Snyder et al. 2006). The band at 580 cm^{-1} in TiN-substrate should be due to vibrations from Ti-N (Jackson et al. 2006), which is observed in Fe_3O_4 to shift to 586 cm^{-1} with decreased intensity possibly due to the interactions and bonding between TiN and initially-sputtered Fe_3O_4. This assumption is supported by a ~2 nm intermixing layer at TiN/Fe_3O_4 interface, with 8 % of Ti diffused into Fe_3O_4 (Xiang et al. 2010b) as well as the absence of Si-O-Fe bonds around 857 cm^{-1} (Thomas et al. 2008). The fairly obvious bands, which are only seen in Fe_3O_4 at around 567 cm^{-1} and 666 cm^{-1} is attributed to the Fe-O stretching vibration in octahedral and tetrahedral sites of Fe_3O_4 respectively, in consistent with published data (Chen and et al. 2008; Thomas et al. 2008). The drastically strong and broad band between 600 and 800 cm^{-1} with the peak centered at round 685 cm^{-1} is considered to be the bending of Fe-O-H, which usually exists in iron oxides (Mitra and et al. 2007; Zhang et al. 2011c). These results well support the formation of Fe_3O_4 on the buffer-layer.

To study the electron transfer between the electrolyte and electrode surface, Nyquist complex plane plots were obtained by room-temperature AC-impedance measurements using $Fe(CN)_6^{4-/3-}$ redox probes (**Fig. 7.2E**). One semicircle is seen for TiN-buffered substrate, meaning an electron transfer-controlled process with a large electron transfer resistance (R_{ct}) indicated by the diameter of the semicircle. This illustrates the dominance of overall impedance by grain boundary resistance, a typical characteristic of TiN (Qiu and Gao 2005). In Fe_3O_4, however, an

entirely different plot is observed, featuring two much smaller consecutive semicircles, which are caused by the competition between dissolution and growth processes on Fe_3O_4 surface. As the equivalent circuit of Fe_3O_4 shows, each parallel RC element is represented by a semicircle with diameters of each more than ten times smaller than that of TiN-buffered substrate, manifesting a much faster electron transfer on the interface and higher conductivity as an electrochemical sensing platform. The dotted lines indicate that the simulated data for each element fit the experimental data well.

7.3.2 Electrochemical catalytic activity

The electrocatalytic activity of epitaxial Fe_3O_4 sensor towards the reduction of H_2O_2 was investigated by voltammetric responses in CV (**Fig. 7.3**). There are no obvious peaks at TiN-modified electrode in the absence of H_2O_2 in the scanned potential range (curve a), while, in contrast, two anodic (at -0.0375 and +0.025 V) and one cathodic peaks can be seen at Fe_3O_4-modified electrode, due to electrochemical behaviors of iron species at different valence states (curve c). The cathodic peak at -0.320 V is probably ascribed to the reduction of Fe(III) in the Fe_3O_4 into Fe, similar to previous observations (Kulkarni and Lokhande 2003), whereas the anodic peaks are associated with the oxidation of Fe and Fe(II) into Fe(III). With 0.5 mM H_2O_2 added, there is only a minor current response seen for TiN-buffered substrate (curve b), which is negligible compared to the remarkably large increase in reduction current from around 0.0 V occurring at Fe_3O_4-modified electrode (curve d), indicating the Fe_3O_4 thin film is a promising material for sensitive H_2O_2 sensing. The cathodic peak of Fe_3O_4 towards H_2O_2 reduction is around -0.5 V. Fe_3O_4 with valence state of Fe(II) and Fe(III) was therefore identified as the electrocatalyst responsible for H_2O_2 reduction, which proceeds as a two-electron and two-proton participating reduction step with generation of H_2O as products. This sensing process is also accompanied by the reductive valence state of Fe(II) on Fe_3O_4 being oxidized into Fe(III) and after that, oxidative valence state Fe(III) is regenerated back into Fe(II) (Rossi et al. 2004). Actually, due to the biocompatibility, facile synthesis and ferrimagnetic properties for easy separations, Fe_3O_4 is used as inert support for enzyme immobilization in the detection of H_2O_2 (Tan et al. 2009). In our present work, however, the as-synthesized epitaxial Fe_3O_4 is capable of efficiently catalyzing the H_2O_2 reduction itself, making it unsuitable as an inert enzyme platform but it is appealing as a stable, ‘green’ and inexpensive peroxidase-like material.

Fig. 7.3: Cyclic voltammograms of electrodes modified with TiN-buffered substrate (a and b) and Fe_3O_4 (c and d) in pH 5.9 50 mM PBS in the absence (a and c) and presence (b and d) of 0.5 mM H_2O_2. Scan rate: 100 $mV \cdot s^{-1}$.

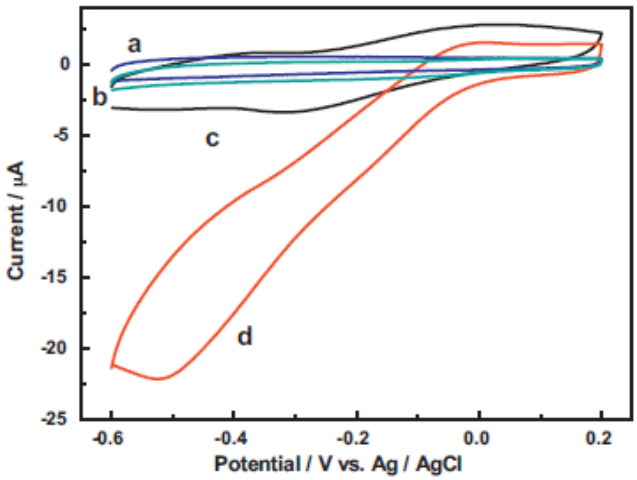

7.3.3 Optimization of sensing

Since the electrochemical catalysis of Fe_3O_4 towards H_2O_2 involves a two-proton process (Lin and Leu 2005), the pH has a strong effect on the sensor performance, predicted to be in favor of mild acidic conditions. The pH dependence of Fe_3O_4-modified electrode was investigated in the pH range of 5.3-8.0 (**Fig. 7.4A**). The amperometric response first increased and then decreased with an increase in pH values, reaching the highest current response at pH 5.9, which is chosen as optimal. Unlike the linear increase in current responses with decreasing pH values down to pH 3.0 in a paper on Fe_3O_4 powder (Lin and Leu 2005), there might be an acidic corrosion process undergoing on the thin film surface at too low a pH, and thus decrease its catalytic activity. However, it is worth noting that the amperometric responses do not change much from pH 5.3 to 7.0, with only about 10 % difference between the highest and lowest responses, indicating the as-synthesized Fe_3O_4 is highly reliable and stable as a sensor in mild acidic conditions, which is advantageous over the use of enzymes.

Fig. 7.4: Amperometric responses of Fe_3O_4 electrode against 0.1 mM H2O2 under (A) different pH under at room temperature and applied potential of -0.4 V, (B) different applied potential at room temperature and pH 5.9 of 50 mM PBS, (C) different temperature at pH 5.9 of 50 mM PBS and applied potential of -0.4 V, while (●) indicates measurements at room temperature around 25 °C. Error bars indicate triplicate measurements.

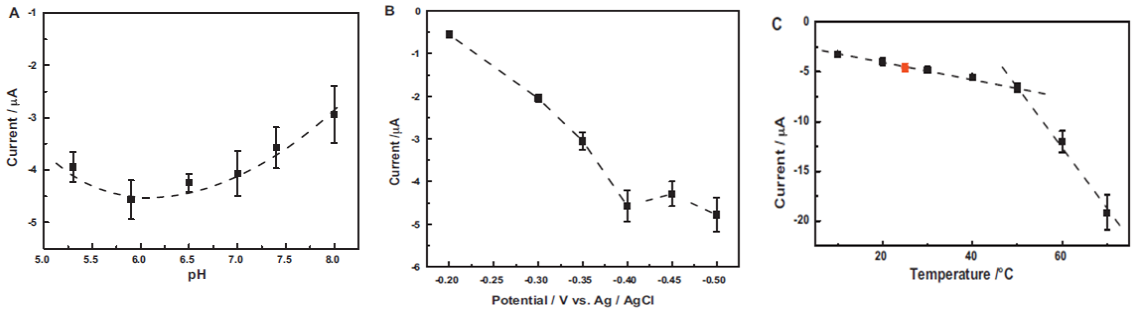

The effect of applied potential on the sensor performance was also studied (**Fig. 7.4B**). The amperometric response is observed to increase almost linearly with an increase in the applied potential of -0.20 to -0.40 V due to increasing driving force for the electrochemical reduction of H_2O_2 (Lin and Leu 2005) and nearly remains unchanged for applied potential larger than -0.40 V. Regarding many compounds in real samples and/or reaction intermediates could be electrochemically reactive under high potentials and extreme pH values, it is more appropriate to carry out the detection under mild pH conditions and relatively low potentials. Therefore, -0.4 V was selected as the working potential.

The effect of temperature on the detection was also investigated (**Fig. 7.4C**). At temperature ranging from 10 to 50 °C, the amperometric responses against 0.1 mM H_2O_2 is linearly dependent on the temperature, with a slope of -0.082 μA/°C (R^2=0.990), including the ambient condition around 25 °C. Judged by the low increase, the sensor has a fairly stable performance within ±10 °C temperature variance at any temperature in this range. Another linear dependence is observed from 50 to 70 °C, with a slope of -0.627 μA/°C (R^2=0.994). These results suggest the Fe_3O_4-modified electrode has an increasing amperometric response in cathodic current with increase in temperature and at higher temperature, the current response increases more remarkably due to faster electrocatalytic kinetics. An important advantage of this oxide-based non-enzymatic sensor is that it can endure a wider temperature range than enzyme-based sensors. Higher temperature (e.g., 70 °C) results in a higher sensitivity, which allows more sensitive detection of H_2O_2. However, though the sensor exhibits higher catalytic performances at higher temperature, with regards to solution evaporation, convenience, and practical routine uses, our entire study was conducted at room temperature.

The voltammetric behavior at different scan rates of the Fe_3O_4-modified electrode were evaluated (**Fig. 7.5**). Identical to **Fig. 7.3** (curve c), two anodic and one cathodic peaks can be observed. With the increasing scan rates from 20-200 $mV \cdot s^{-1}$, the two anodic peaks shifted

positively while the cathodic peak shifted negatively. Their peak currents all increased linearly (R^2=0.988, 0.990 and 0.986 for peaks a1, a2 and c1, respectively) along with the increase in square root of scan rates (**Fig. 7.5** inset). These results reveal a non-surface controlled electrochemical process at Fe_3O_4 electrode, caused by electron hopping. This result was further supported by our finding that the thickness of the thin film (90, 180, 270 nm) does not have any significant influence on the electrocatalytic effect on H_2O_2, in accordance to the non-surface-controlled electrocatalytical process.

Fig. 7.5: Cyclic voltammograms of Fe_3O_4 electrode in pH 5.9 in 50 mM PBS at different scan rates of 20, 30, 40, 60, 80, 100, 120, 140, 160, 180 and 200 $mV \cdot s^{-1}$ in an increasing order from inner to outer (a to k) as the arrow indicates. Anodic and cathodic peaks are labeled as in the figure. Inset shows the plots of anodic and cathodic peak currents vs. square root of scan rates.

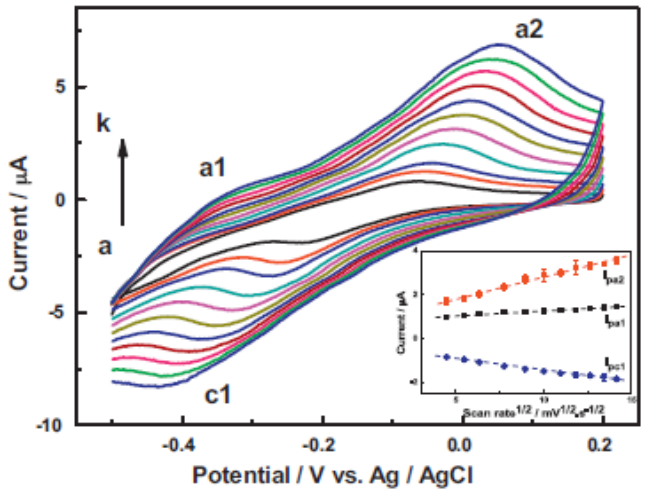

7.3.4 Analytical performances

The amperometric sensing of H_2O_2 at the TiN-substrate and Fe_3O_4-modified electrodes was accomplished at optimal pH 5.9 and in 50 mM PBS under optimal potential of -0.4 V with stepwise addition of 0.1 mM H_2O_2 (**Fig. 7.6A**). Obviously, the amperometric current responses at Fe_3O_4-modified electrode are significantly larger than the nearly negligible responses at TiN-substrate, consistent with the results from CV (**Fig. 7.3** b and d), which once again confirms that Fe_3O_4 is the key contributing element in the sensing application. It is also clearly seen that with gradual addition of H_2O_2, the current response first increased and then decreased with further additions, implying a progressive electrocatalytic inactivation in the presence of higher concentration of H_2O_2, possibly caused by the generation of reaction intermediates. A good

linear dependence of current response vs. H_2O_2 concentration (i(μA)=-38.9*C-2.34, R^2=0.991) at Fe_3O_4 electrode was found within the linear range of up to 0.7 mM (**Fig. 7.6B**), with an acceptable sensitivity of 432.2 μA mM^{-1} cm^{-2}. The detection limit is determined to be 1.0 μM (at signal/noise=3) which is lower than other enzymatic or enzymeless Fe_3O_4-based biosensors such as Fe_3O_4 NP-PDDA composite film (Zhang et al. 2008a), HRP-Fe_3O_4-Chitosan modified GCE (Tan et al. 2009), and Fe_3O_4-Ag hybrid materials (Liu et al. 2010). This high sensitivity and low detection limit are owing to the large and rough surface area of epitaxially-grown columnar grains as well as the high electrocatalytic activity of as-synthesized Fe_3O_4.

Fig. 7.6: (A) Current-time responses of (a) TiN-buffered substrate and (b) Fe_3O_4 electrodes with stepwise additions of 0.1 mM H_2O_2 every 50 s. (B) Linear dependence of current response on H_2O_2 concentration at Fe_3O_4 electrode. Error bars indicate triplicate measurements. Applied potential: -0.4 V.

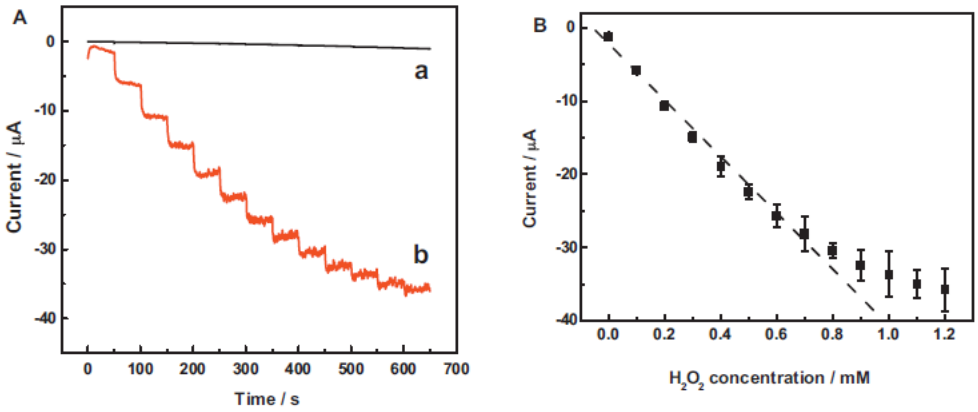

7.3.5 Sensor stability and specificity

The stability of the sensor was tested by measuring its current response to H_2O_2 after being stored under ambient conditions and there were no obvious decrease in the response within one week, and lost only about 10 % of its original sensitivity over 20 days, suggesting its acceptable stability over this period. The operational stability was also investigated by measuring its amperometric response over 20 min (**Fig. 7.7A**), and the current response maintained a stable and well-defined plateau with little observable loss. The sensor responded extremely fast upon addition of H_2O_2 and was able to achieve 95 % of steady-state current within about 5 s (**Fig. 7.7A** inset). The rapid response could be attributed to the rough surface of the epitaxial thin film as well as the facilitation of electron transfers by the columnar Fe_3O_4 grains. The reproducibility of the sensor was studied by measuring the current response to 0.1

mM H_2O_2 10 times using the same electrode, only with a relative standard deviation of 6.8 %. Meanwhile, three electrodes prepared at identical conditions had a RSD of 9.2 %. These results confirm satisfactory stability and good reproducibility of our sensor. Given its simple material synthesis, easy preparation and availability for mass manufactures, the epitaxial Fe_3O_4 thin film is a promising material for H_2O_2 sensing.

Fig. 7.7: (A) Stability of the amperometric response of Fe_3O_4 electrode towards 0.1 mM H2O2 in pH 5.9 50 mM PBS at -0.4 V over an operational time of 1200 s. Inset shows the response time to achieve a steady-state current. (B) Correlation of Fe_3O_4 sensor to HPLC-UV. Error bars indicate triplicate measurements.

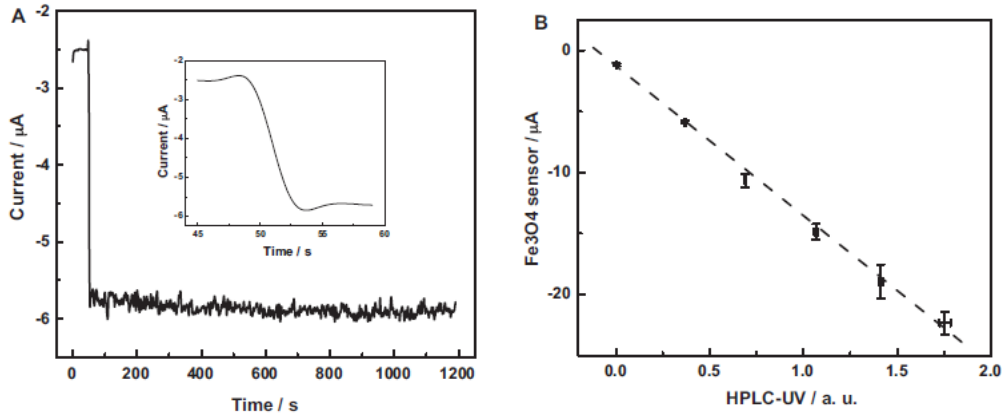

Electrochemically active compounds that can simultaneously generate detectable current signals along with detecting substrates have remained a significant challenge for electrochemical sensors. The general pharmaceutical grade of H_2O_2 for products at drugstores or supermarket such as antimicrobial agents for treating wounds and sanitizing agents is about 3 %, while the beautician grade can be 6 % for hair coloring. In food industry for production of foods such as cheese, eggs, and whey-containing products, the food grade is as high as 35 %. However, though the concentration of H_2O_2 in these real samples is much higher than potentially oxidizable ingredients, it has still been frequently reported that some organic acids such as AA and UA (Chen et al. 2010; Xiao et al. 2000) as well as some sugars (Batchelor-McAuley et al. 2008b) can possibly produce highly influencing electrochemical signals. We examined the specificity of our sensor by investigating a number of interfering species such as sugars, salts, proteins etc. that possibly co-exist with H_2O_2 in real samples. As shown in **Table 7.1**, the current response from H_2O_2 sensing was barely influenced by any interferents, producing negligible interferences between 0.02 to 5.86 %. Noticeably, the chloride poisoning which is

usually a major issue for signal loss in most metal or metal oxide based enzymeless sensors, is not observed with our sensor even at very high concentration of chloride ions. It could be inferred that our sensor has excellent specificity to H_2O_2 and immune to wide range of interferents and thus is suitable for use as an enzymeless and interference-free sensor in complex sample matrices.

Table 7.1: Effects of different interferents on H_2O_2 determination by our sensor

Interferents	Current ratio (%)	Interferents	Current ratio (%)	Interferents	Current ratio (%)
Sucrose	**5.60**	**glycine**	**4.55**	**Mg(NO3)2**	**0.85**
D-fructose	**4.10**	**histamine**	**0.09**	**CaCl2**	**4.64**
D-(+)-maltose	**1.08**	**fumaric acid**	**2.12**	**Al2(SO4)3**	**0.88**
β-D-lactose	**0.02**	**caffeine**	**0.10**	**BSA[a]**	**3.18**
D-(+)-glucose	**0.79**	**citric acid**	**3.89**	**KCl**	**2.37**
Na2CO3	**0.05**	**Mannose**	**2.09**	**Xanthan gum[a]**	**0.04**
NaCl[c]	**1.57**	**Dopamine**	**0.06**	**Ascorbic acid**	**0.20**
Uric acid	**0.40**	**Casein[b]**	**1.60**	**β-lactogluboin[a]**	**5.86**
KH2PO4[c]	**1.86**	**Na2HPO4[c]**	**2.03**		

7.3.6 H_2O_2 testing in real samples

The performance of our sensor was compared with that of a commercially-available HPLC system equipped with UV detector for measuring H_2O_2 in medical and food products. A series of standard H_2O_2 solutions were tested using the two techniques; the results correlated well, with R^2=0.996 (**Fig. 7.7B**). Further tests were conducted using complex matrices which are readily available on the market such as dental care product (Crest Whitening mouthwash solution), sanitizing agent (Walgreens antiseptic/oral debriding agent), and food samples (Diet Coke, Gatorade), which were diluted and tested. The results obtained with our sensor are consistent with those obtained with HPLC-UV (**Table 7.2**). Our sensor also displayed acceptable recovery rates and therefore can well serve as a potential candidate for routine analysis both for prevention of internal consumption and monitor in manufacturing and environmental aspects.

Table 7.2: Comparing the performance of our sensor to that of an HPLC in determination of H_2O_2 in different commercial samples (n=6)

Samples	HPLC	Our proposed sensor	Recovery rate	Added
Walgreen antiseptic/oral debriding agent	0.736±0.015 M	0.785±0.056 M	99.54%	0.1 mM
Crest whitening mouthwash solution	0.336±0.009 M	0.417±0.034 M	91.74%	0.1 mM
Diet coke	N/A	N/A	101.63%	0.1 mM
Gatorade	N/A	N/A	97.48%	0.1 mM

7.4. Conclusions

A facile and easy approach to synthesize epitaxial Fe_3O_4 thin film with needle-like columnar surface structures suitable for mass scale production has been developed. The as-synthesized material displayed extraordinary electrocatalytic activity to H_2O_2 reduction with a dynamic working range of up to 0.7 mM with a low detection limit of 1.0 µM, a rapid response time of less than 5 s and a high sensitivity of 432.2 µA mM^{-1} cm^{-2}. As an ideal enzymeless sensing candidate material, it also has good stability, acceptable reproducibility and satisfying specificity against common interferents co-existing in medical and food products. Taking the miniaturization of electrochemical devices, it is possible to fabricate a hand-held detection device for routine analysis in industry.

Summary and Future Work

In this thesis, different carbon or carbon hybrid based electrochemical biosensors are developed for detection of food ingredients and additives such as sugars. I presented the controlled synthesis of vertically-aligned MWCNTs by CVD using Co catalyst. Further modifications of the MWCNTs arrays with certain nanostructures synthesized in different routes endow them with excellent electrocatalytic activities towards Glc, thereby qualified as highly-sensitive enzyme-free sensors. Despite the satisfactory sensitivity and acceptable selectivity of this group of sensors, they only work well under limited systems such as blood serum testing and experience some drawbacks such as gradual oxidation of the catalyst materials and loss in sensitivities over time when exposed in air. However, they still have unbelievable potentials especially when they are in combined use with good separation systems such as HPLC where electrochemical sensors are the major detectors for sugar analysis. In the meantime, a green, facile and controllable electrochemical reduction for synthesis of reduced graphene oxide starting from graphite was shown and the ERGO was applied for different sensing purposes. Specifically, two different types of enzymatic sensors were also investigated in this thesis to justify their performances based on indirect detections of the consumption of solvated O_2 in the system or the enzymatic product H_2O_2 respectively. Apparently, the sensitivities of enzymatic sensors are not as high as enzyme-free ones and involve more complicated fabrication processes as well as more legitimate systems (such as closed system), but they offer better selectivity and more straightforward detection mechanisms. Lastly, some other food contaminants or additives such as dopamine and H_2O_2 were successfully detected. In order to carry out out-of-lab detections, microfluidic devices incorporating SPEs or ITO-based disposable working electrodes were fabricated to meet the miniaturization needs. Logical extension and further steps in the line of research are to further explore the applications of the materials and methods I developed here and apply them for other sensing purposes such as immunosensing for food-borne pathogens, pH sensing and heavy metal sensing. Some of the work are being carried out underway by myself but cannot be presented here in time.

References:

Adewuyi, S., Kareem, K.T., Atayese, A.O., Amolegbe, S.A., Akinremi, C.A., Chitosan–cobalt(II) and nickel(II) chelates as antibacterial agents. *International Journal of Biological Macromolecules* 2011, 48, 301-303.

Ai, H., Huang, X., Zhu, Z., Liu, J., Chi, Q., Li, Y., Li, Z., Ji, X., A novel glucose sensor based on monodispersed Ni/Al layered double hydroxide and chitosan. *Biosensors and Bioelectronics* 2008, 24, 1048-1052.

Akbari-adergani, B., Norouzi, P., Ganjali, M.R., Dinarvand, R., Ultrasensitive flow-injection electrochemical method for determination of histamine in tuna fish samples. *Food Research International* 2010, 43, 1116-1122.

Arduini, F., Amine, A., Majorani, C., Di Giorgio, F., De Felicis, D., Cataldo, F., Moscone, D., Palleschi, G., High performance electrochemical sensor based on modified screen-printed electrodes with cost-effective dispersion of nanostructured carbon black. *Electrochemistry Communications* 2010, 12, 346-350.

Arumugam, P.U., Chen, H., Siddiqui, S., Weinrich, J.A.P., Jejelowo, A., Li, J., Meyyappan, M., Wafer-scale fabrication of patterned carbon nanofiber nanoelectrode arrays: A route for development of multiplexed, ultrasensitive disposable biosensors. *Biosensors and Bioelectronics* 2009, 24, 2818-2824.

Banks, C.E., Crossley, A., Salter, C., Wilkins, S.J., Compton, R.G., Carbon nanotubes contain metal impurities which are responsible for the "electrocatalysis" seen at some nanotube-modified electrodes. *Angew Chem Int Edit* 2006, 45, 2533-2537.

Batchelor-McAuley, C., Du, Y., Wildgoose, G.G., Compton, R.G., The use of copper(II) oxide nanorod bundles for the non-enzymatic voltammetric sensing of carbohydrates and hydrogen peroxide. *Sensor Actuat B-Chem* 2008a, 135, 230-235.

Batchelor-McAuley, C., Du, Y., Wildgoose, G.G., Compton, R.G., The use of copper(II) oxide nanorod bundles for the non-enzymatic voltammetric sensing of carbohydrates and hydrogen peroxide. *Sensors and Actuators B: Chemical* 2008b, 135, 230-235.

Batchelor-McAuley, C., Wildgoose, G.G., Compton, R.G., Shao, L.D., Green, M.L.H., Copper oxide nanoparticle impurities are responsible for the electroanalytical detection of glucose seen using. *Sensor Actuat B-Chem* 2008c, 132, 356-360.

Bernsmann, F., Ball, V., Addiego, F.d.r., Ponche, A., Michel, M., Gracio, J.J.d.A., Toniazzo, V.r., Ruch, D., Dopamine−Melanin Film Deposition Depends on the Used Oxidant and Buffer Solution. *Langmuir* 2011, 27, 2819-2825.

Boehm, D.A., Gottlieb, P.A., Hua, S.Z., On-chip microfluidic biosensor for bacterial detection and identification. *Sensors and Actuators B: Chemical* 2007, 126, 508-514.

Brett, C.M.A., Electrochemical sensors for environmental monitoring. Strategy and examples. *Pure Appl Chem* 2001, 73, 1969-1977.

Bulwan M., W.K., Zapotoczny S., and Nowakowska M., Chitosan-Based Ultrathin Films as Antifouling, Anticoagulant and Antibacterial Protective Coatings. *Journal of Biomaterials Science* 2011.

Buratti, S., Brunetti, B., Mannino, S., Amperometric detection of carbohydrates and thiols by using a glassy carbon electrode coated with Co oxide/multi-wall carbon nanotubes catalytic system. *Talanta* 2008, 76, 454-457.

Candelaria, S.L., Shao, Y., Zhou, W., Li, X., Xiao, J., Zhang, J.-G., Wang, Y., Liu, J., Li, J., Cao, G., Nanostructured carbon for energy storage and conversion. *Nano Energy* 2012, 1, 195-220.

Cao, D., Chao, J., Sun, L., Wang, G., Catalytic behavior of Co3O4 in electroreduction of H2O2. *J Power Sources* 2008, 179, 87-91.
Casella, I.G., Electrodeposition of cobalt oxide films from carbonate solutions containing Co(II)-tartrate complexes. *Journal of Electroanalytical Chemistry* 2002, 520, 119-125.
Casella, I.G., Gatta, M., Study of the electrochemical deposition and properties of cobalt oxide species in citrate alkaline solutions. *Journal of Electroanalytical Chemistry* 2002, 534, 31-38.
Castro, E.B., Gervasi, C.A., Vilche, J.R., Oxygen evolution on electrodeposited cobalt oxides. *J Appl Electrochem* 1998, 28, 835-841.
Cerpakovska, D., Kalnins, M., Tupureina, V., Dzene, A., Characterization of various kinds of paper as reinforcement for biodegradable polymer composites. *P Est Acad Sci* 2009, 58, 40-44.
Chakraborty, S., Retna Raj, C., Pt nanoparticle-based highly sensitive platform for the enzyme-free amperometric sensing of H2O2. *Biosensors and Bioelectronics* 2009, 24, 3264-3268.
Chandra, R.P., Ragauskas, A.J., Modification of high-lignin kraft pulps with laccase. Part 2. Xylanase-enhanced strength benefits. *Biotechnol Progr* 2005, 21, 1302-1306.
Chen, F.H., et al., The grafting and release behavior of doxorubincin from Fe 3 O 4 @ SiO 2 core–shell structure nanoparticles via an acid cleaving amide bond: the potential for magnetic targeting drug delivery. *Nanotechnology* 2008, 19, 165103.
Chen, J., Zhang, W.D., Ye, J.S., Nonenzymatic electrochemical glucose sensor based on MnO2/MWNTs nanocomposite. *Electrochem Commun* 2008, 10, 1268-1271.
Chen, M., Kumar, D., Yi, C.-W., Goodman, D.W., The Promotional Effect of Gold in Catalysis by Palladium-Gold. *Science* 2005, 310, 291-293.
Chen, Q.D., Shen, X.H., Gao, H.C., Formation of solid and hollow cuprous oxide nanocubes in water-in-oil microemulsions controlled by the yield of hydrated electrons. *J Colloid Interf Sci* 2007, 312, 272-278.
Chen, X.M., Lin, Z.J., Chen, D.J., Jia, T.T., Cai, Z.M., Wang, X.R., Chen, X., Chen, G.N., Oyama, M., Nonenzymatic amperometric sensing of glucose by using palladium nanoparticles supported on functional carbon nanotubes. *Biosens Bioelectron* 2010, 25, 1803-1808.
Chen, Y., Zhang, X.O., Zhang, D.C., Yu, P., Ma, Y.W., High performance supercapacitors based on reduced graphene oxide in aqueous and ionic liquid electrolytes. *Carbon* 2011, 49, 573-580.
Cherevko S., C.C., The porous CuO electrode fabricated by hydrogen bubble evolution and its application to highly sensitive non-enzymatic glucose detection. *Talanta* 2010, 80, 1371-1377.
Choi, B.G., Park, H., Park, T.J., Yang, M.H., Kim, J.S., Jang, S.-Y., Heo, N.S., Lee, S.Y., Kong, J., Hong, W.H., Solution Chemistry of Self-Assembled Graphene Nanohybrids for High-Performance Flexible Biosensors. *Acs Nano* 2010, 4, 2910-2918.
Chou, S.-L., Wang, J.-Z., Choucair, M., Liu, H.-K., Stride, J.A., Dou, S.-X., Enhanced reversible lithium storage in a nanosize silicon/graphene composite. *Electrochem Commun* 2010, 12, 303-306.
Clark L. C., L.C., Electrode systems for continuous monitoring in cardiovascular. *Annals of the New York Academy of Sciences* 1962, 102, 29-45.
Clark L., L.C., Electrode systems for continuous monitoring in cardiovascular. *Annals of the New York Academy of Sciences* 1962, 102, 29-45.
Claussen, J.C., Franklin, A.D., ul Haque, A., Porterfield, D.M., Fisher, T.S., Electrochemical Biosensor of Nanocube-Augmented Carbon Nanotube Networks. *Acs Nano* 2009, 3, 37-44.
Comfort, A.R., Albert, E.C., Langer, R., Immobilized Enzyme Cellulose Hollow Fibers .1. Immobilization of Heparinase. *Biotechnol Bioeng* 1989, 34, 1366-1373.
De Zhang, W., Wen, Y., Liu, S.M., Tjiu, W.C., Xu, G.Q., Gan, L.M., Synthesis of vertically aligned carbon nanotubes on metal deposited quartz plates. *Carbon* 2002, 40, 1981-1989.

Delaney, J.L., Hogan, C.F., Tian, J., Shen, W., Electrogenerated Chemiluminescence Detection in Paper-Based Microfluidic Sensors. *Anal Chem* 2011, 83, 1300-1306.
Deng, C.Y., Chen, J.H., Chen, X.L., Mao, C.H., Nie, L.H., Yao, S.Z., Direct electrochemistry of glucose oxidase and biosensing for glucose based on boron-doped carbon nanotubes modified electrode. *Biosens Bioelectron* 2008, 23, 1272-1277.
Deng, C.Y., Chen, J.H., Nie, Z., Si, S.H., A sensitive and stable biosensor based on the direct electrochemistry of glucose oxidase assembled layer-by-layer at the multiwall carbon nanotube-modified electrode. *Biosens Bioelectron* 2010, 26, 213-219.
Deng, S., Jian, G., Lei, J., Hu, Z., Ju, H., A glucose biosensor based on direct electrochemistry of glucose oxidase immobilized on nitrogen-doped carbon nanotubes. *Biosensors and Bioelectronics* 2009a, 25, 373-377.
Deng, S.Y., Jian, G.Q., Lei, J.P., Hu, Z., Ju, H.X., A glucose biosensor based on direct electrochemistry of glucose oxidase immobilized on nitrogen-doped carbon nanotubes. *Biosens Bioelectron* 2009b, 25, 373-377.
Dungchai, W., Chailapakul, O., Henry, C.S., Electrochemical Detection for Paper-Based Microfluidics. *Analytical Chemistry* 2009, 81, 5821-5826.
Eda, G., Lin, Y.Y., Mattevi, C., Yamaguchi, H., Chen, H.A., Chen, I.S., Chen, C.W., Chhowalla, M., Blue photoluminescence from chemically derived graphene oxide. *Adv Mater* 2010, 22, 505-509.
Gao, L., Zhuang, J., Nie, L., Zhang, J., Zhang, Y., Gu, N., Wang, T., Feng, J., Yang, D., Perrett, S., Yan, X., Intrinsic peroxidase-like activity of ferromagnetic nanoparticles. *Nat Nano* 2007, 2, 577-583.
Garjonyte, R., Malinauskas, A., Amperometric glucose biosensor based on glucose oxidase immobilized in poly(o-phenylenediamine) layer. *Sensor Actuat B-Chem* 1999, 56, 85-92.
Geim, A.K., Novoselov, K.S., The rise of graphene. *Nat Mater* 2007, 6, 183-191.
Ghodbane, O., Roue, L., Belanger, D., Copper electrodeposition on pyrolytic graphite electrodes: Effect of the copper salt on the electrodeposition process. *Electrochim Acta* 2007, 52, 5843-5855.
Goncalves, G., Marques, P.A.A.P., Granadeiro, C.M., Nogueira, H.I.S., Singh, M.K., Grácio, J., Surface Modification of Graphene Nanosheets with Gold Nanoparticles: The Role of Oxygen Moieties at Graphene Surface on Gold Nucleation and Growth. *Chem Mater* 2009, 21, 4796-4802.
Gong, K., Du, F., Xia, Z., Durstock, M., Dai, L., Nitrogen-Doped Carbon Nanotube Arrays with High Electrocatalytic Activity for Oxygen Reduction. *Science* 2009, 323, 760-764.
Goto, M., Obuchi, R., Hiroshi, T., Sakaki, T., Shibata, M., Hydrothermal conversion of municipal organic waste into resources. *Bioresource Technol* 2004, 93, 279-284.
Grieshaber, D., MacKenzie, R., Voros, J., Reimhult, E., Electrochemical biosensors - Sensor principles and architectures. *Sensors-Basel* 2008a, 8, 1400-1458.
Grieshaber, D., MacKenzie, R., Vörös, J., Reimhult, E., Electrochemical Biosensors - Sensor Principles and Architectures. *Sensors-Basel* 2008b, 8, 1400-1458.
Grisotto, F., Metaye, R., Jousselme, B., Geffroy, B., Palacin, S., Charlier, J., Scanning electrochemical microscopy as an etching tool for ITO patterning. *Journal of Materials Chemistry* 2011, 21.
Grossman, S.P., The Role of Glucose, Insulin and Glucagon in the Regulation of Food-Intake and Body-Weight. *Neurosci Biobehav R* 1986, 10, 295-315.
Guo, H.-L., Wang, X.-F., Qian, Q.-Y., Wang, F.-B., Xia, X.-H., A Green Approach to the Synthesis of Graphene Nanosheets. *Acs Nano* 2009, 3, 2653-2659.
Guth, U., Vonau, W., Zosel, J., Recent developments in electrochemical sensor application and technology-a review. *Meas Sci Technol* 2009, 20, -.

Hall, S.B., Khudaish, E.A., Hart, A.L., Electrochemical oxidation of hydrogen peroxide at platinum electrodes. Part V: inhibition by chloride. *Electrochim Acta* 2000, 45, 3573-3579.
Han, D., Han, T., Shan, C., Ivaska, A., Niu, L., Simultaneous Determination of Ascorbic Acid, Dopamine and Uric Acid with Chitosan-Graphene Modified Electrode. *Electroanalysis* 2010, 22, 2001-2008.
Han, J., Zhuo, Y., Chai, Y.-Q., Mao, L., Yuan, Y.-L., Yuan, R., Highly conducting gold nanoparticles–graphene nanohybrid films for ultrasensitive detection of carcinoembryonic antigen. *Talanta* 2011, 85, 130-135.
Hernandez, Y., Nicolosi, V., Lotya, M., Blighe, F.M., Sun, Z., De, S., McGovern, I.T., Holland, B., Byrne, M., Gun'Ko, Y.K., Boland, J.J., Niraj, P., Duesberg, G., Krishnamurthy, S., Goodhue, R., Hutchison, J., Scardaci, V., Ferrari, A.C., Coleman, J.N., High-yield production of graphene by liquid-phase exfoliation of graphite. *Nat Nano* 2008, 3, 563-568.
Ho, J., Tan, M.K., Go, D.B., Yeo, L.Y., Friend, J.R., Chang, H.-C., Paper-Based Microfluidic Surface Acoustic Wave Sample Delivery and Ionization Source for Rapid and Sensitive Ambient Mass Spectrometry. *Analytical Chemistry* 2011, 83, 3260-3266.
Hones J., M.P.a.S.N., The Technology Behind Glucose Meters: Test Strips. *Diabetes Technol. Ther.* 2008, 10, 10-26.
Hsu, C.-L., Chang, K.-S., Kuo, J.-C., Determination of hydrogen peroxide residues in aseptically packaged beverages using an amperometric sensor based on a palladium electrode. *Food Control* 2008, 19, 223-230.
Huang, C.J., Chiu, P.H., Wang, Y.H., Chen, W.R., Meen, T.H., Synthesis of the gold nanocubes by electrochemical technique. *J Electrochem Soc* 2006, 153, D129-D133.
Humberston CL, D.B., Krenzelok EP Ingestion of 35% hydrogen peroxide. *J Toxicol Clin Toxicol* 1990, 28, 95-100.
Hummers, W.S., Offeman, R.E., Preparation of Graphitic Oxide. *J Am Chem Soc* 1958, 80, 1339-1339.
Jackson, A.W., Shebanova, O., Davy-Faraday Research Laboratory, R.I.o.G.B., 21 Albemarle Street, London W1X 4BS], Hector, A.L.E.-m.a.l.h.s.a.u., McMillan, P.F.E.-m.p.f.m.u.a.u., Amorphous and nanocrystalline titanium nitride and carbonitride materials obtained by solution phase ammonolysis of Ti(NMe{sub 2}){sub 4}. *Journal Name: Journal of Solid State Chemistry; Journal Volume: 179; Journal Issue: 5; Other Information: DOI: 10.1016/j.jssc.2006.01.067; PII: S0022-4596(06)00062-4; Copyright (c) 2006 Elsevier Science B.V., Amsterdam, The Netherlands, All rights reserved; Country of input: International Atomic Energy Agency (IAEA)* 2006, Medium: X; Size: page(s) 1383-1393.
Jacobs, C.B., Peairs, M.J., Venton, B.J., Review: Carbon nanotube based electrochemical sensors for biomolecules. *Analytica Chimica Acta* 2010, 662, 105-127.
Jain, R., Rather, J.A., Dwivedi, A., Vikas, Highly Sensitive and Selective Voltammetric Sensor Fullerene Modified Glassy Carbon Electrode for Determination of Cefitizoxime in Solubilized System. *Electroanalysis* 2010, 22, 2600-2606.
Jawaheer, S., White, S.F., Rughooputh, S.D.D.V., Cullen, D.C., Development of a common biosensor format for an enzyme based biosensor array to monitor fruit quality. *Biosensors and Bioelectronics* 2003, 18, 1429-1437.
Jayatissa, A.H., Guo, K., Jayasuriya, A.C., Gupta, T., Fabrication of nanocrystalline cobalt oxide via sol-gel coating. *Mat Sci Eng B-Solid* 2007, 144, 69-72.
Jena, B.K., Raj, C.R., Enzyme-free amperometric sensing of glucose by using gold nanoparticles. *Chem-Eur J* 2006, 12, 2702-2708.
Ji, C.X., Lu, F., Chang, Y.A., Yang, J.J., Rzchowski, M.S., Growth and physical property of epitaxial Co70Fe30 thin film on Si substrate via TiN buffer. *Appl Phys Lett* 2008, 92, -.

Joo, S., Park, S., Chung, T.D., Kim, H.C., Integration of a nanoporous platinum thin film into a microfluidic system for non-enzymatic electrochemical glucose sensing. *Anal Sci* 2007, 23, 277-281.

Kadara, R.O., Jenkinson, N., Banks, C.E., Characterisation of commercially available electrochemical sensing platforms. *Sensors and Actuators B: Chemical* 2009a, 138, 556-562.

Kadara, R.O., Jenkinson, N., Banks, C.E., Characterisation of commercially available electrochemical sensing platforms. *Sensor Actuat B-Chem* 2009b, 138, 556-562.

Kang, X., Wang, J., Wu, H., Aksay, I.A., Liu, J., Lin, Y., Glucose Oxidase-graphene-chitosan modified electrode for direct electrochemistry and glucose sensing. *Biosensors and Bioelectronics* 2009, 25, 901-905.

Kang, X.H., Mai, Z.B., Zou, X.Y., Cai, P.X., Mo, J.Y., A sensitive nonenzymatic glucose sensor in alkaline media with a copper nanocluster/multiwall carbon nano tube-modified glassy carbon electrode. *Anal Biochem* 2007, 363, 143-150.

Katz, E., Willner, I., Biomolecule-functionalized carbon nanotubes: Applications in nanobioelectronics. *Chemphyschem* 2004, 5, 1085-1104.

Katz, E., Willner, I., Wang, J., Electroanalytical and Bioelectroanalytical Systems Based on Metal and Semiconductor Nanoparticles. *Electroanal* 2004, 16, 19-44.

Kim, C.O., Hong, S.-Y., Kim, M., Park, S.-M., Park, J.W., Modification of indium–tin oxide (ITO) glass with aziridine provides a surface of high amine density. *Journal of Colloid and Interface Science* 2004, 277, 499-504.

King, H., Aubert, R.E., Herman, W.H., Global burden of diabetes, 1995-2025 - Prevalence, numerical estimates, and projections. *Diabetes Care* 1998, 21, 1414-1431.

Knutson, K., Ragauskas, A., Laccase-mediator biobleaching applied to a direct yellow dyed paper. *Biotechnol Progr* 2004, 20, 1893-1896.

Koehne, J.E., Marsh, M., Boakye, A., Douglas, B., Kim, I.Y., Chang, S.-Y., Jang, D.-P., Bennet, K.E., Kimble, C., Andrews, R., Meyyappan, M., Lee, K.H., Carbon nanofiber electrode array for electrochemical detection of dopamine using fast scan cyclic voltammetry. *Analyst* 2011, 136.

Komathi, S., Gopalan, A.I., Lee, K.-P., Nanomolar detection of dopamine at multi-walled carbon nanotube grafted silica network/gold nanoparticle functionalised nanocomposite electrodes. *Analyst* 2010, 135.

Kong, T., Chen, Y., Ye, Y.P., Zhang, K., Wang, Z.X., Wang, X.P., An amperometric glucose biosensor based on the immobilization of glucose oxidase on the ZnO nanotubes. *Sensor Actuat B-Chem* 2009, 138, 344-350.

Kulkarni, S.S., Lokhande, C.D., Structural, optical, electrical and dielectrical properties of electrosynthesized nanocrystalline iron oxide thin films. *Mater Chem Phys* 2003, 82, 151-156.

Kurniawan, F., Tsakova, V., Mirsky, V.M., Gold nanoparticles in nonenzymatic electrochemical detection of sugars. *Electroanal* 2006, 18, 1937-1942.

Lankelma, J., Nie, Z., Carrilho, E., Whitesides, G.M., Paper-Based Analytical Device for Electrochemical Flow-Injection Analysis of Glucose in Urine. *Analytical Chemistry* 2012a, 84, 4147-4152.

Lankelma, J., Nie, Z.H., Carrilho, E., Whitesides, G.M., Paper-Based Analytical Device for Electrochemical Flow-Injection Analysis of Glucose in Urine. *Analytical Chemistry* 2012b, 84, 4147-4152.

Laviron, E., Adsorption, autoinhibition and autocatalysis in polarography and in linear potential sweep voltammetry. *Journal of Electroanalytical Chemistry and Interfacial Electrochemistry* 1974, 52, 355-393.

Laviron, E., General expression of the linear potential sweep voltammogram in the case of diffusionless electrochemical systems. *Journal of Electroanalytical Chemistry and Interfacial Electrochemistry* 1979, 101, 19-28.
Lei, C.-X., Hu, S.-Q., Shen, G.-L., Yu, R.-Q., Immobilization of horseradish peroxidase to a nano-Au monolayer modified chitosan-entrapped carbon paste electrode for the detection of hydrogen peroxide. *Talanta* 2003, 59, 981-988.
Li, C., Liu, Y., Li, L., Du, Z., Xu, S., Zhang, M., Yin, X., Wang, T., A novel amperometric biosensor based on NiO hollow nanospheres for biosensing glucose. *Talanta* 2008a, 77, 455-459.
Li, D., Muller, M.B., Gilje, S., Kaner, R.B., Wallace, G.G., Processable aqueous dispersions of graphene nanosheets. *Nat Nanotechnol* 2008b, 3, 101-105.
Li, M., Zhu, J.E., Zhang, L., Chen, X., Zhang, H., Zhang, F., Xu, S., Evans, D.G., Facile synthesis of NiAl-layered double hydroxide/graphene hybrid with enhanced electrochemical properties for detection of dopamine. *Nanoscale* 2011, 3.
Li, X., Zhu, Q., Tong, S., Wang, W., Song, W., Self-assembled microstructure of carbon nanotubes for enzymeless glucose sensor. *Sensors and Actuators B: Chemical* 2009a, 136, 444-450.
Li, X., Zhu, Q.Y., Tong, S.F., Wang, W., Song, W.B., Self-assembled microstructure of carbon nanotubes for enzymeless glucose sensor. *Sensor Actuat B-Chem* 2009b, 136, 444-450.
Li, Y., Song, Y.Y., Yang, C., Xia, X.H., Hydrogen bubble dynamic template synthesis of porous gold for nonenzymatic electrochemical detection of glucose. *Electrochem Commun* 2007, 9, 981-988.
Lim, S.H., Wei, J., Lin, J.Y., Li, Q.T., KuaYou, J., A glucose biosensor based on electrodeposition of palladium nanoparticles and glucose oxidase onto Nafion-solubilized carbon nanotube electrode. *Biosens Bioelectron* 2005, 20, 2341-2346.
Lin, M.S., Leu, H.J., A Fe3O4-Based Chemical Sensor for Cathodic Determination of Hydrogen Peroxide. *Electroanal* 2005, 17, 2068-2073.
Liu, C.B., Wang, K., Luo, S.L., Tang, Y.H., Chen, L.Y., Direct Electrodeposition of Graphene Enabling the One-Step Synthesis of Graphene-Metal Nanocomposite Films. *Small* 2011, 7, 1203-1206.
Liu, C.Y., Chen, C.F., Leu, J.P., Tunable interconnectivity of mesostructured cobalt oxide materials for sensing applications. *Sensor Actuat B-Chem* 2009a, 137, 700-703.
Liu, S.Q., Zhang, X.T., Wu, Y.F., Tu, Y.F., He, L., Prostate-specific antigen detection by using a reusable amperometric immunosensor based on reversible binding and leasing of HRP-anti-PSA from phenylboronic acid modified electrode. *Clin Chim Acta* 2008, 395, 51-56.
Liu, Y., Teng, H., Hou, H., You, T., Nonenzymatic glucose sensor based on renewable electrospun Ni nanoparticle-loaded carbon nanofiber paste electrode. *Biosensors and Bioelectronics* 2009b, 24, 3329-3334.
Liu, Z., Wang, H., Li, B., Liu, C., Jiang, Y., Yu, G., Mu, X., Biocompatible magnetic cellulose-chitosan hybrid gel microspheres reconstituted from ionic liquids for enzyme immobilization. *J Mater Chem* 2012, 22, 15085-15091.
Liu, Z., Zhao, B., Shi, Y., Guo, C., Yang, H., Li, Z., Novel nonenzymatic hydrogen peroxide sensor based on iron oxide-silver hybrid submicrospheres. *Talanta* 2010, 81, 1650-1654.
LopezOngil, S., GinesRuiz, J.A., Iglesias, M.C., Ruiz, P., Bujan, J., RodriguezPuyol, D., Contraction of endothelial cells by hydrogen peroxide (H2O2): A novel putative mechanism of tissue damage. *Kidney Int* 1996, 50, 1795-1795.
Lu, J., Do, I., Drzal, L.T., Worden, R.M., Lee, I., Nanometal-Decorated Exfoliated Graphite Nanoplatelet Based Glucose Biosensors with High Sensitivity and Fast Response. *Acs Nano* 2008, 2, 1825-1832.

Lu, L.-M., Li, H.-B., Qu, F., Zhang, X.-B., Shen, G.-L., Yu, R.-Q., In situ synthesis of palladium nanoparticle-graphene nanohybrids and their application in nonenzymatic glucose biosensors. *Biosensors and Bioelectronics* 2011, 26, 3500-3504.

Lu, L.M., Zhang, L., Qu, F.L., Lu, H.X., Zhang, X.B., Wu, Z.S., Huan, S.Y., Wang, Q.A., Shen, G.L., Yu, R.Q., A nano-Ni based ultrasensitive nonenzymatic electrochemical sensor for glucose: Enhancing sensitivity through a nanowire array strategy. *Biosens Bioelectron* 2009, 25, 218-223.

Luo, L., Li, Q., Xu, Y., Ding, Y., Wang, X., Deng, D., Xu, Y., Amperometric glucose biosensor based on NiFe2O4 nanoparticles and chitosan. *Sensors and Actuators B: Chemical* 2010, 145, 293-298.

Luo, M.Z., Baldwin, R.P., Characterization of Carbohydrate Oxidation at Copper Electrodes. *Journal of Electroanalytical Chemistry* 1995, 387, 87-94.

Luo, X.L., Xu, J.J., Du, Y., Chen, H.Y., A glucose biosensor based on chitosan-glucose oxidase-gold nanoparticles biocomposite formed by one-step electrodeposition. *Anal Biochem* 2004, 334, 284-289.

Maalouf, R., Chebib, H., Saikali, Y., Vittori, O., Sigaud, M., Jaffrezic-Renault, N., Amperometric and impedimetric characterization of a glutamate biosensor based on Nafion((R)) and a methyl viologen modified glassy carbon electrode. *Biosens Bioelectron* 2007, 22, 2682-2688.

Male, K.B., Hrapovic, S., Liu, Y.L., Wang, D.S., Luong, J.H.T., Electrochemical detection of carbohydrates using copper nanoparticles and carbon nanotubes. *Anal Chim Acta* 2004, 516, 35-41.

Mansfield, S.D., Laccase impregnation during mechanical pulp processing - improved refining efficiency and sheet strength. *Appita J* 2002, 55, 49-53.

Mantanis, G.I., Young, R.A., Rowell, R.M., Swelling of Compressed Cellulose Fiber Webs in Organic Liquids. *Cellulose* 1995, 2, 1-22.

Margulies, D.T., Parker, F.T., Spada, F.E., Goldman, R.S., Li, J., Sinclair, R., Berkowitz, A.E., Anomalous moment and anisotropy behavior in Fe_{3}O_{4} films. *Phys Rev B* 1996, 53, 9175.

Martinez, A.W., Phillips, S.T., Carrilho, E., Thomas, S.W., Sindi, H., Whitesides, G.M., Simple telemedicine for developing regions: Camera phones and paper-based microfluidic devices for real-time, off-site diagnosis. *Analytical Chemistry* 2008, 80, 3699-3707.

Martis, P., Dilimon, V.S., Delhalle, J., Mekhalif, Z., Electro-generated nickel/carbon nanotube composites in ionic liquid. *Electrochim Acta* 2010, 55, 5407-5410.

Masoodi, R., Pillai, K.M., Varanasi, P.P., Effect of Externally Applied Liquid Pressure on Wicking in Paper Wipes. *J Eng Fiber Fabr* 2010, 5, 49-66.

McCartney, L.J., Pickup, J.C., Rolinski, O.J., Birch, D.J.S., Near-Infrared Fluorescence Lifetime Assay for Serum Glucose Based on Allophycocyanin-Labeled Concanavalin A. *Anal Biochem* 2001, 292, 216-221.

Medintz, I.L., Stewart, M.H., Trammell, S.A., Susumu, K., Delehanty, J.B., Mei, B.C., Melinger, J.S., Blanco-Canosa, J.B., Dawson, P.E., Mattoussi, H., Quantum-dot/dopamine bioconjugates function as redox coupled assemblies for in vitro and intracellular pH sensing. *Nat Mater* 2010, 9, 676-684.

Meng, L., Jin, J., Yang, G., Lu, T., Zhang, H., Cai, C., Nonenzymatic Electrochemical Detection of Glucose Based on Palladium−Single-Walled Carbon Nanotube Hybrid Nanostructures. *Anal Chem* 2009, 81, 7271-7280.

Merkoci, A., Pumera, M., Llopis, X., Perez, B., del Valle, M., Alegret, S., New materials for electrochemical sensing VI: Carbon nanotubes. *Trac-Trend Anal Chem* 2005, 24, 826-838.

Metcalf, E.C., Morgan, M.R.A., Dean, P.D.G., Chromatographic assay of steroids on immuno-affinity paper strips; a rapid method for the quantitation of digoxin and oestriol-16α-glucuronide concentrations. *Journal of Chromatography A* 1982, 235, 501-506.

Milardovic, S., Kruhak, I., Ivekovic, D., Rumenjak, V., Tkalcec, M., Grabaric, B.S., Glucose determination in blood samples using flow injection analysis and an amperometric biosensor based on glucose oxidase immobilized on hexacyanoferrate modified nickel electrode. *Anal Chim Acta* 1997, 350, 91-96.

Mitra, S., et al., Synthesis of a α-Fe 2 O 3 nanocrystal in its different morphological attributes: growth mechanism, optical and magnetic properties. *Nanotechnology* 2007, 18, 275608.

Mu, Y., Jia, D., He, Y., Miao, Y., Wu, H.-L., Nano nickel oxide modified non-enzymatic glucose sensors with enhanced sensitivity through an electrochemical process strategy at high potential. *Biosensors and Bioelectronics* 2011, 26, 2948-2952.

Muszynski, R., Seger, B., Kamat, P.V., Decorating Graphene Sheets with Gold Nanoparticles. *The Journal of Physical Chemistry C* 2008, 112, 5263-5266.

Nasirpouri, F., Bending, S.J., Peter, L.M., Fangohr, H., Electrodeposition and magnetic properties of three-dimensional bulk and shell nickel mesostructures. *Thin Solid Films* 2011, 519, 8320-8325.

Ndamanisha, J.C., Bo, X., Guo, L., Electrocatalytic reduction of oxygen at ordered mesoporous carbon functionalized with tetrathiafulvalene. *Analyst* 2010, 135, 621-629.

Ng, H.T., Fang, A., Huang, L., Li, S.F.Y., Protein Microarrays on ITO Surfaces by a Direct Covalent Attachment Scheme. *Langmuir* 2002, 18, 6324-6329.

Nie, H., Yao, Z., Zhou, X., Yang, Z., Huang, S., Nonenzymatic electrochemical detection of glucose using well-distributed nickel nanoparticles on straight multi-walled carbon nanotubes. *Biosensors and Bioelectronics* 2011, 30, 28-34.

Nie, Z.H., Nijhuis, C.A., Gong, J.L., Chen, X., Kumachev, A., Martinez, A.W., Narovlyansky, M., Whitesides, G.M., Electrochemical sensing in paper-based microfluidic devices. *Lab on a Chip* 2010, 10, 477-483.

Njagi, J., Chernov, M.M., Leiter, J.C., Andreescu, S., Amperometric Detection of Dopamine in Vivo with an Enzyme Based Carbon Fiber Microbiosensor. *Anal Chem* 2010, 82, 989-996.

Nugent, J.M., Santhanam, K.S.V., Rubio, A., Ajayan, P.M., Fast electron transfer kinetics on multiwalled carbon nanotube microbundle electrodes. *Nano Lett* 2001, 1, 87-91.

Ozkan, S.A., Ozkan, Y., Senturk, Z., Electrochemical reduction of metronidazole at activated glassy carbon electrode and its determination in pharmaceutical dosage forms. *Journal of Pharmaceutical and Biomedical Analysis* 1998, 17, 299-305.

Pal, E., Hornok, V., Oszko, A., Dekany, I., Hydrothermal synthesis of prism-like and flower-like ZnO and indium-doped ZnO structures. *Colloid Surface A* 2009, 340, 1-9.

Palchetti, I., Mascini, M., Electroanalytical biosensors and their potential for food pathogen and toxin detection. *Anal Bioanal Chem* 2008, 391, 455-471.

Park, I., Cheng, J., Pisano, A.P., Lee, E.S., Jeong, J.H., Low temperature, low pressure nanoimprinting of chitosan as a biomaterial for bionanotechnology applications. *Appl Phys Lett* 2007, 90.

Park, S., Boo, H., Chung, T.D., Electrochemical non-enzymatic glucose sensors. *Anal Chim Acta* 2006, 556, 46-57.

Park, S., Chung, T.D., Kim, H.C., Nonenzymatic glucose detection using mesoporous platinum. *Anal Chem* 2003, 75, 3046-3049.

Park, S., Park, S., Jeong, R.A., Boo, H., Park, J., Kim, H.C., Chung, T.D., Nonenzymatic continuous glucose monitoring in human whole blood using electrified nanoporous Pt. *Biosens Bioelectron* 2012, 31, 284-291.

Poh, H.L., Pumera, M., Nanoporous Carbon Materials for Electrochemical Sensing. *Chemistry-an Asian Journal* 2012, 7, 412-416.

Potara, M., Baia, M., Farcau, C., Astilean, S., Chitosan-coated anisotropic silver nanoparticles as a SERS substrate for single-molecule detection. *Nanotechnology* 2012, 23.

Pumera, M., Ambrosi, A., Bonanni, A., Chng, E.L.K., Poh, H.L., Graphene for electrochemical sensing and biosensing. *Trac-Trends in Analytical Chemistry* 2010, 29, 954-965.

Qiu, Y., Gao, L., Novel Polyaniline/Titanium Nitride Nanocomposite: Controllable Struc tures and Electrical/Electrochemical Properties. *The Journal of Physical Chemistry B* 2005, 109, 19732-19740.

Qu, L., Liu, Y., Baek, J.-B., Dai, L., Nitrogen-Doped Graphene as Efficient Metal-Free Electrocatalyst for Oxygen Reduction in Fuel Cells. *Acs Nano* 2010, 4, 1321-1326.

Qureshi, A., Kang, W.P., Davidson, J.L., Gurbuz, Y., Review on carbon-derived, solid-state, micro and nano sensors for electrochemical sensing applications. *Diam Relat Mater* 2009, 18, 1401-1420.

Rattanarat, P., Dungchai, W., Siangproh, W., Chailapakul, O., Henry, C.S., Sodium dodecyl sulfate-modified electrochemical paper-based analytical device for determination of dopamine levels in biological samples. *Anal Chim Acta* 2012, 744, 1-7.

Reitz, E., Jia, W.Z., Gentile, M., Wang, Y., Lei, Y., CuO Nanospheres Based Nonenzymatic Glucose Sensor. *Electroanal* 2008, 20, 2482-2486.

Ren, X., Pickup, P.G., An impedance study of electron transport and electron transfer in composite polypyrrole + polystyrenesulphonate films. *Journal of Electroanalytical Chemistry* 1997a, 420, 251-257.

Ren, X.L., Chen, D., Meng, X.W., Tang, F.Q., Du, A.M., Zhang, L., Amperometric glucose biosensor based on a gold nanorods/cellulose acetate composite film as immobilization matrix. *Colloid Surface B* 2009, 72, 188-192.

Ren, X.M., Pickup, P.G., An impedance study of electron transport and electron transfer in composite polypyrrole plus polystyrenesulphonate films. *J Electroanal Chem* 1997b, 420, 251-257.

Robert H, C., Paul A, R., J. E, M., Guy, R., 1955. The Role of Sugar in the Food Industry. USE OF SUGARS AND OTHER CARBOHYDRATES IN THE FOOD INDUSTRY, pp. 3-20. AMERICAN CHEMICAL SOCIETY.

Rohlfing, C.L., Wiedmeyer, H.-M., Little, R.R., England, J.D., Tennill, A., Goldstein, D.E., Defining the Relationship Between Plasma Glucose and HbA1c. *Diabetes Care* 2002, 25, 275-278.

Ronkainen, N.J., Halsall, H.B., Heineman, W.R., Electrochemical biosensors. *Chem Soc Rev* 2010, 39, 1747-1763.

Rossi, L.M., Quach, A.D., Rosenzweig, Z., Glucose oxidase-magnetite nanoparticles bioconjugate for glucose sensing. *Anal. Bioanal. Chem.* 2004, 380, 606-613.

Royo, B., Sosna, M., Asensio, A.C., Moran, J.F., Ferapontova, E.E., Direct electrochemistry and environmental sensing of rice hemoglobin immobilized at graphite electrodes. *Journal of Electroanalytical Chemistry* 2013, 704, 67-74.

Salimi, A., Roushani, M., Non-enzymatic glucose detection free of ascorbic acid interference using nickel powder and nafion sol–gel dispersed renewable carbon ceramic electrode. *Electrochemistry Communications* 2005, 7, 879-887.

Schumacher, L.C., Holzhueter, I.B., Hill, I.R., Dignam, M.J., Semiconducting and Electrocatalytic Properties of Sputtered Cobalt Oxide-Films. *Electrochim Acta* 1990, 35, 975-984.

Segal, M., Selling graphene by the ton. *Nat Nano* 2009, 4, 612-614.

Shamsipur, M., Najafi, M., Hosseini, M.-R.M., Highly improved electrooxidation of glucose at a nickel(II) oxide/multi-walled carbon nanotube modified glassy carbon electrode. *Bioelectrochemistry* 2010, 77, 120-124.

Shao, M., Palladium-based electrocatalysts for hydrogen oxidation and oxygen reduction reactions. *J Power Sources* 2011, 196, 2433-2444.
Shao, Y., Wang, J., Engelhard, M., Wang, C., Lin, Y., Facile and controllable electrochemical reduction of graphene oxide and its applications. *Journal of Materials Chemistry* 2010, 20, 743-748.
Shi, B.-X., Wang, Y., Zhang, K., Lam, T.-L., Chan, H.L.-W., Monitoring of dopamine release in single cell using ultrasensitive ITO microsensors modified with carbon nanotubes. *Biosensors and Bioelectronics* 2011, 26, 2917-2921.
Sidorov, T.A., Vibration spectra of three-component silicate glasses and the role of chemical elements in the structure of glass. *Journal of Applied Spectroscopy* 1967, 7, 258-261.
Snyder, M.Q., McCool, B.A., DiCarlo, J., Tripp, C.P., DeSisto, W.J., An infrared study of the surface chemistry of titanium nitride atomic layer deposition on silica from TiCl4 and NH3. *Thin Solid Films* 2006, 514, 97-102.
Spector, A., Kleiman, N.J., Huang, R.-R.C., Wang, R.-R., Repair of H2O2-induced DNA damage in bovine lens epithelial cell cultures. *Experimental Eye Research* 1989, 49, 685-698.
Stankovich, S., Dikin, D.A., Dommett, G.H.B., Kohlhaas, K.M., Zimney, E.J., Stach, E.A., Piner, R.D., Nguyen, S.T., Ruoff, R.S., Graphene-based composite materials. *Nature* 2006, 442, 282-286.
Stoller, M.D., Park, S., Zhu, Y., An, J., Ruoff, R.S., Graphene-Based Ultracapacitors. *Nano Lett* 2008, 8, 3498-3502.
Sun, A., Zheng, J., Sheng, Q., A highly sensitive non-enzymatic glucose sensor based on nickel and multi-walled carbon nanotubes nanohybrid films fabricated by one-step co-electrodeposition in ionic liquids. *Electrochim Acta* 2012, 65, 64-69.
Sun, Y.P., Buck, H., Mallouk, T.E., Combinatorial discovery of alloy electrocatalysts for amperometric glucose sensors. *Anal Chem* 2001, 73, 1599-1604.
Swamy, B.E., Venton, B.J., Carbon nanotube-modified microelectrodes for simultaneous detection of dopamine and serotonin in vivo. *Analyst* 2007, 132, 876-884.
Tan, S.N., Ge, L.Y., Wang, W., Paper Disk on Screen Printed Electrode for One-Step Sensing with an Internal Standard. *Analytical Chemistry* 2010, 82, 8844-8847.
Tan, X.C., Zhang, J.L., Tan, S.W., Zhao, D.D., Huang, Z.W., Mi, Y., Huang, Z.Y., Amperometric Hydrogen Peroxide Biosensor Based on Horseradish Peroxidase Immobilized on Fe3O4/Chitosan Modified Glassy Carbon Electrode. *Electroanal* 2009, 21, 1514-1520.
Tao, Y., Gong, F.H., Wang, H., Wu, H.P., Tao, G.L., Microwave-assisted preparation of cerium dioxide nanocubes. *Mater Chem Phys* 2008, 112, 973-976.
Thangaraj, R., Kumar, A.S., Graphitized mesoporous carbon modified glassy carbon electrode for selective sensing of xanthine, hypoxanthine and uric acid. *Analytical Methods* 2012, 4, 2162-2171.
Thomas, S., Sakthikumar, D., Yoshida, Y., Anantharaman, M.R., Spectroscopic and photoluminescence studies on optically transparent magnetic nanocomposites based on sol-gel glass: Fe3O4. *J Nanopart Res* 2008, 10, 203-206.
Tian, Y., Rui, Q., Komori, K., Liu, H.Q., Luo, Y.P., Sakai, Y., Electrochemical biosensor for the detection of H(2)O(2) from living cancer cells based on ZnO nanosheets. *Anal Chim Acta* 2010, 670, 57-62.
Toghill, K.E., Xiao, L., Phillips, M.A., Compton, R.G., The non-enzymatic determination of glucose using an electrolytically fabricated nickel microparticle modified boron-doped diamond electrode or nickel foil electrode. *Sensors and Actuators B: Chemical* 2010a, 147, 642-652.
Toghill, K.E., Xiao, L., Phillips, M.A., Compton, R.G., The non-enzymatic determination of glucose using an electrolytically fabricated nickel microparticle modified boron-doped diamond electrode or nickel foil electrode. *Sensors and Actuators B-Chemical* 2010b, 147, 642-652.

Tominaga, M., Shimazoe, T., Nagashima, M., Taniguchi, I., Composition-activity relationships of carbon electrode-supported bimetallic gold-silver nanoparticles in electrocatalytic oxidation of glucose. *J Electroanal Chem* 2008a, 615, 51-61.
Tominaga, M., Taema, Y., Taniguchi, I., Electrocatalytic glucose oxidation at bimetallic gold-copper nanoparticle-modified carbon electrodes in alkaline solution. *J Electroanal Chem* 2008b, 624, 1-8.
Trafela, T., Strlič, M., Kolar, J., Lichtblau, D.A., Anders, M., Mencigar, D.P., Pihlar, B., Nondestructive Analysis and Dating of Historical Paper Based on IR Spectroscopy and Chemometric Data Evaluation. *Analytical Chemistry* 2007, 79, 6319-6323.
Umar, A., Rahman, M.M., Al-Hajry, A., Hahn, Y.B., Enzymatic glucose biosensor based on flower-shaped copper oxide nanostructures composed of thin nanosheets. *Electrochem Commun* 2009, 11, 278-281.
Venton, B.J., Wightman, R.M., Psychoanalytical Electrochemistry: Dopamine and Behavior. *Anal Chem* 2003, 75, 414 A-421 A.
Vlandas, A., Kurkina, T., Ahmad, A., Kern, K., Balasubramanian, K., Enzyme-Free Sugar Sensing in Microfluidic Channels with an Affinity-Based Single-Wall Carbon Nanotube Sensor. *Analytical Chemistry* 2010, 82, 6090-6097.
Wan, Y., Lin, Z., Zhang, D., Wang, Y., Hou, B., Impedimetric immunosensor doped with reduced graphene sheets fabricated by controllable electrodeposition for the non-labelled detection of bacteria. *Biosensors and Bioelectronics* 2011, 26, 1959-1964.
Wang, D.G., Guo, F., Chen, J.F., Zhao, R.H., Zhang, Z.T., Synthesis of nano-platelets of modified aluminium hydroxide by high-gravity reactive precipitation and hydrothermal method. *Mater Chem Phys* 2008a, 107, 426-430.
Wang, J., Electrochemical biosensors: Towards point-of-care cancer diagnostics. *Biosens Bioelectron* 2006, 21, 1887-1892.
Wang, J., Thomas, D.F., Chen, A., Nonenzymatic electrochemical glucose sensor based on nanoporous PtPb networks. *Anal Chem* 2008b, 80, 997-1004.
Wang, K., Xu, J.J., Chen, H.Y., A novel glucose biosensor based on the nanoscaled cobalt phthalocyanine-glucose oxidase biocomposite. *Biosens Bioelectron* 2005, 20, 1388-1396.
Wang W., Z.L., Tong S., Li X., Song W., Three-dimensional network films of electrospun copper oxide nanofibers for glucose determination

Biosensors and Bioelectronics 2009, 25, 708-714.
Wang, X., Jin, B., Lin, X., In-situ FTIR spectroelectrochemical study of dopamine at a glassy carbon electrode in a neutral solution. *Anal Sci* 2002, 18, 931-933.
Wang, X.D., Chen, H.X., Zhou, T.Y., Lin, Z.J., Zeng, J.B., Xie, Z.X., Chen, X., Wong, K.Y., Chen, G.N., Wang, X.R., Optical colorimetric sensor strip for direct readout glucose measurement. *Biosens Bioelectron* 2009, 24, 3702-3705.
Wei, D., Qian, W., Facile synthesis of Ag and Au nanoparticles utilizing chitosan as a mediator agent. *Colloids and Surfaces B: Biointerfaces* 2008, 62, 136-142.
Wei, H., Sun, J.J., Guo, L., Li, X., Chen, G.N., Highly enhanced electrocatalytic oxidation of glucose and shikimic acid at a disposable electrically heated oxide covered copper electrode. *Chemical Communications* 2009, 2842-2844.
Wei, H., Wang, E., Fe3O4 Magnetic Nanoparticles as Peroxidase Mimetics and Their Applications in H2O2 and Glucose Detection. *Anal Chem* 2008, 80, 2250-2254.
Williams, K.R., Adhyaru, B., German, I., Russell, T., Determination of a Diffusion Coefficient by Capillary Electrophoresis. An Experiment for the Physical and Biophysical Chemistry Laboratories. *Journal of Chemical Education* 2002, 79, 1475.

Wilson, M.S., Electrochemical Immunosensors for the Simultaneous Detection of Two Tumor Markers. *Anal Chem* 2005, 77, 1496-1502.
Wilson, M.S., Nie, W.Y., Electrochemical multianalyte immunoassays using an array-based sensor. *Anal Chem* 2006, 78, 2507-2513.
Wilson, R., Turner, A.P.F., Glucose-Oxidase - an Ideal Enzyme. *Biosens Bioelectron* 1992, 7, 165-185.
Wu, J., Yan, F., Zhang, X.Q., Yan, Y.T., Tang, J.H., Ju, H.X., Disposable reagentless electrochemical immunosensor array based on a biopolymer/sol-gel membrane for simultaneous measurement of several tumor markers. *Clin Chem* 2008, 54, 1481-1488.
Wu, L.-Q., Lee, K., Wang, X., English, D.S., Losert, W., Payne, G.F., Chitosan-Mediated and Spatially Selective Electrodeposition of Nanoscale Particles. *Langmuir* 2005, 21, 3641-3646.
Xiang, H., Ji, C.X., Yang, J.J., Chang, Y.A., Compositional effect of bcc Co100-x Fe (x) electrodes on magnetoresistance in AlO (x) -based magnetic tunnel junctions. *Appl Phys a-Mater* 2010a, 98, 707-710.
Xiang, H., Shi, F.Y., Rzchowski, M.S., Voyles, P.M., Chang, Y.A., Epitaxial growth and magnetic properties of Fe3O4 films on TiN buffered Si(001), Si(110), and Si(111) substrates. *Appl Phys Lett* 2010b, 97, -.
Xiao, L., Chen, J., Cha, C.-s., Elimination of the interference of ascorbic acid in the amperometric detection of biomolecules in body fluid samples and the simple detection of uric acid in human serum and urine by using the powder microelectrode technique. *Journal of Electroanalytical Chemistry* 2000, 495, 27-35.
Xu, C., Wang, X., Zhu, J., Graphene–Metal Particle Nanocomposites. *The Journal of Physical Chemistry C* 2008a, 112, 19841-19845.
Xu, Y., Bai, H., Lu, G., Li, C., Shi, G., Flexible Graphene Films via the Filtration of Water-Soluble Noncovalent Functionalized Graphene Sheets. *Journal of the American Chemical Society* 2008b, 130, 5856-5857.
Xu, Y., Bai, H., Lu, G., Li, C., Shi, G., Flexible graphene films via the filtration of water-soluble noncovalent functionalized graphene sheets. *J Am Chem Soc* 2008c, 130, 5856-5857.
Yan, J., Zhou, H.J., Yu, P., Su, L., Mao, L.Q., A general electrochemical approach to deposition of metal hydroxide/oxide nanostructures onto carbon nanotubes. *Electrochem Commun* 2008, 10, 761-765.
Yang, J., Deng, S., Lei, J., Ju, H., Gunasekaran, S., Electrochemical synthesis of reduced graphene sheet–AuPd alloy nanoparticle composites for enzymatic biosensing. *Biosensors and Bioelectronics* 2011a, 29, 159-166.
Yang, J., Deng, S.Y., Lei, J.P., Ju, H.X., Gunasekaran, S., Electrochemical synthesis of reduced graphene sheet-AuPd alloy nanoparticle composites for enzymatic biosensing. *Biosensors & Bioelectronics* 2011b, 29, 159-166.
Yang, J., Strickler, J.R., Gunasekaran, S., Indium tin oxide-coated glass modified with reduced graphene oxide sheets and gold nanoparticles as disposable working electrodes for dopamine sensing in meat samples. *Nanoscale* 2012a.
Yang, J., Strickler, J.R., Gunasekaran, S., Indium tin oxide-coated glass modified with reduced graphene oxide sheets and gold nanoparticles as disposable working electrodes for dopamine sensing in meat samples. *Nanoscale* 2012b, 4, 4594-4602.
Yang, J., Xiang, H., Shuai, L., Gunasekaran, S., A sensitive enzymeless hydrogen-peroxide sensor based on epitaxially-grown Fe3O4 thin film. *Analytica Chimica Acta* 2011c, 708, 44-51.
Yang, J., Yu, J.H., Strickler, J.R., Chang, W.J., Gunasekaran, S., Nickel nanoparticle-chitosan-reduced graphene oxide-modified screen-printed electrodes for enzyme-free glucose sensing in portable microfluidic devices. *Biosensors & Bioelectronics* 2013, 47, 530-538.

Yang, J., Zhang, W.-D., Gunasekaran, S., An amperometric non-enzymatic glucose sensor by electrodepositing copper nanocubes onto vertically well-aligned multi-walled carbon nanotube arrays. *Biosensors and Bioelectronics* 2010a, 26, 279-284.

Yang, J., Zhang, W.-d., Gunasekaran, S., A low-potential, H2O2-assisted electrodeposition of cobalt oxide/hydroxide nanostructures onto vertically-aligned multi-walled carbon nanotube arrays for glucose sensing. *Electrochim Acta* 2011d, 56, 5538-5544.

Yang, J., Zhang, W.D., Gunasekaran, S., A low-potential, H2O2-assisted electrodeposition of cobalt oxide/hydroxide nanostructures onto vertically-aligned multi-walled carbon nanotube arrays for glucose sensing. *Electrochimica Acta* 2011e, 56, 5538-5544.

Yang, J.A., Zhang, W.D., Gunasekaran, S., An amperometric non-enzymatic glucose sensor by electrodepositing copper nanocubes onto vertically well-aligned multi-walled carbon nanotube arrays. *Biosensors & Bioelectronics* 2010b, 26, 279-284.

Yang, L., Xiong, H., Zhang, X., Wang, S., Zhang, X., Direct electrochemistry of glucose oxidase and biosensing for glucose based on boron-doped carbon-coated nickel modified electrode. *Biosensors and Bioelectronics* 2011f, 26, 3801-3805.

Yang, M.H., Yang, Y., Yang, H.F., Shen, G.L., Yu, R.Q., Layer-by-layer self-assembled multilayer films of carbon nanotubes and platinum nanoparticles with polyelectrolyte for the fabrication of biosensors. *Biomaterials* 2006a, 27, 246-255.

Yang, M.H., Yang, Y.H., Liu, Y.L., Shen, G.L., Yu, R.Q., Platinum nanoparticles-doped sol-gel/carbon nanotubes composite electrochemical sensors and biosensors. *Biosens Bioelectron* 2006b, 21, 1125-1131.

Yang, S., Liu, X., Zeng, X., Xia, B., Gu, J., Luo, S., Mai, N., Wei, W., Fabrication of nano-copper/carbon nanotubes/chitosan film by one-step electrodeposition and its sensitive determination of nitrite. *Sensors and Actuators B: Chemical* 2010c, 145, 762-768.

Ye, J.S., Cui, H.F., Liu, X., Lim, T.M., Zhang, W.D., Sheu, F.S., Preparation and characterization of aligned carbon nanotube-ruthenium oxide nanocomposites for supercapacitors. *Small* 2005, 1, 560-565.

Ye, J.S., Wen, Y., De Zhang, W., Cui, H.F., Gan, L.M., Xu, G.Q., Sheu, F.S., Application of multi-walled carbon nanotubes functionalized with hemin for oxygen detection in neutral solution. *Journal of Electroanalytical Chemistry* 2004a, 562, 241-246.

Ye, J.S., Wen, Y., De Zhang, W., Gan, L.M., Xu, G.Q., Sheu, F.S., Selective voltammetric detection of uric acid in the presence of ascorbic acid at well-aligned carbon nanotube electrode. *Electroanal* 2003, 15, 1693-1698.

Ye, J.S., Wen, Y., Zhang, W.D., Gan, L.M., Xu, G.Q., Sheu, F.S., Nonenzymatic glucose detection using multi-walled carbon nanotube electrodes. *Electrochem Commun* 2004b, 6, 66-70.

Yin, H., Zhou, Y., Ma, Q., Ai, S., Chen, Q., Zhu, L., Electrocatalytic oxidation behavior of guanosine at graphene, chitosan and Fe3O4 nanoparticles modified glassy carbon electrode and its determination. *Talanta* 2010a, 82, 1193-1199.

Yin, H., Zhou, Y., Ma, Q., Ai, S., Chen, Q., Zhu, L., Electrocatalytic oxidation behavior of guanosine at graphene, chitosan and Fe3O4 nanoparticles modified glassy carbon electrode and its determination. *Talanta* 2010b, 82, 1193-1199.

You, T., Niwa, O., Chen, Z., Hayashi, K., Tomita, M., Hirono, S., An Amperometric Detector Formed of Highly Dispersed Ni Nanoparticles Embedded in a Graphite-like Carbon Film Electrode for Sugar Determination. *Analytical Chemistry* 2003, 75, 5191-5196.

Yu, C., Luo, M., Zeng, F., Zheng, F., Wu, S., Mesoporous silica particles for selective detection of dopamine with [small beta]-cyclodextrin as the selective barricade. *Chem Commun* 2011a, 47.

Yu, J.H., Ge, L., Huang, J.D., Wang, S.M., Ge, S.G., Microfluidic paper-based chemiluminescence biosensor for simultaneous determination of glucose and uric acid. *Lab on a Chip* 2011b, 11, 1286-1291.
Yu, K.F., Guo, Y.P., Ding, X.F., Zhao, J.Z., Wang, Z.C., Synthesis of silica nanocubes by sol-gel method. *Mater Lett* 2005, 59, 4013-4015.
Yu, L.G., Zhang, G.M., Wu, Y., Bai, X., Guo, D.Z., Cupric oxide nanoflowers synthesized with a simple solution route and their field emission. *J Cryst Growth* 2008, 310, 3125-3130.
Yu, P., Zhou, D., Thin-film biosensor for the measurement of glucose concentration in human serum and urine. *Anal Chim Acta* 1995, 300, 91-97.
Yu, W.W., White, I.M., Inkjet Printed Surface Enhanced Raman Spectroscopy Array on Cellulose Paper. *Analytical Chemistry* 2010, 82, 9626-9630.
Yuan, B.Y., Wang, C., Li, L., Chen, S.H., Real time observation of the anodic dissolution of copper in NaCl solution with the digital holography. *Electrochem Commun* 2009, 11, 1373-1376.
Yuan, J.H., Wang, K., Xia, X.H., Highly ordered platinum-nanotubule arrays for amperometric glucose sensing. *Adv Funct Mater* 2005, 15, 803-809.
Yuan, P., Zhuo, Y., Chai, Y., Ju, H., Dendritic Silver/Silicon Dioxide Nanocomposite Modified Electrodes for Electrochemical Sensing of Hydrogen Peroxide. *Electroanal* 2008, 20, 1839-1844.
Zaworski, P.G., Gill, G.S., Precipitation and recovery of proteins from culture supernatants using zinc. *Anal Biochem* 1988, 173, 440-444.
Zeng, X., Li, X., Xing, L., Liu, X., Luo, S., Wei, W., Kong, B., Li, Y., Electrodeposition of chitosan–ionic liquid–glucose oxidase biocomposite onto nano-gold electrode for amperometric glucose sensing. *Biosensors and Bioelectronics* 2009a, 24, 2898-2903.
Zeng, X.D., Li, X.F., Xing, L., Liu, X.Y., Luo, S.L., Wei, W.Z., Kong, B., Li, Y.H., Electrodeposition of chitosan-ionic liquid-glucose oxidase biocomposite onto nano-gold electrode for amperometric glucose sensing. *Biosens Bioelectron* 2009b, 24, 2898-2903.
Zhang, J., Lei, J., Pan, R., Leng, C., Hu, Z., Ju, H., In situ assembly of gold nanoparticles on nitrogen-doped carbon nanotubes for sensitive immunosensing of microcystin-LR. *Chem Commun* 2011a, 47, 668-670.
Zhang, J., Sasaki, K., Sutter, E., Adzic, R.R., Stabilization of Platinum Oxygen-Reduction Electrocatalysts Using Gold Clusters. *Science* 2007, 315, 220-222.
Zhang, L., Zhai, Y., Gao, N., Wen, D., Dong, S., Sensing H2O2 with layer-by-layer assembled Fe3O4-PDDA nanocomposite film. *Electrochem Commun* 2008a, 10, 1524-1526.
Zhang, S., Shao, Y., Liao, H.-g., Liu, J., Aksay, I.A., Yin, G., Lin, Y., Graphene Decorated with PtAu Alloy Nanoparticles: Facile Synthesis and Promising Application for Formic Acid Oxidation. *Chem Mater* 2011b, 23, 1079-1081.
Zhang, S., Shao, Y., Yin, G., Lin, Y., Electrostatic Self-Assembly of a Pt-around-Au Nanocomposite with High Activity towards Formic Acid Oxidation. *Angewandte Chemie International Edition* 2010a, 49, 2211-2214.
Zhang, S., Wu, W., Xiao, X., Zhou, J., Ren, F., Jiang, C., Preparation and characterization of spindle-like Fe3O4 mesoporous nanoparticles. *Nanoscale Res Lett* 2011c, 6, 89.
Zhang, W.-D., Xu, B., Jiang, L.-C., Functional hybrid materials based on carbon nanotubes and metal oxides. *Journal of Materials Chemistry* 2010b, 20, 6383-6391.
Zhang, W.D., Thong, J.T.L., Tjiu, W.C., Gan, L.M., Fabrication of vertically aligned carbon nanotubes patterns by chemical vapor deposition for field emitters. *Diamond and Related Materials* 2002, 11, 1638-1642.
Zhang, X.J., Wang, G.F., Liu, X.W., Wu, J.J., Li, M., Gu, J., Liu, H., Fang, B., Different CuO Nanostructures: Synthesis, Characterization, and Applications for Glucose Sensors. *J Phys Chem C* 2008b, 112, 16845-16849.

Zhao, C., Shao, C., Li, M., Jiao, K., Flow-injection analysis of glucose without enzyme based on electrocatalytic oxidation of glucose at a nickel electrode. *Talanta* 2007a, 71, 1769-1773.
Zhao, C.Z., Shao, C.L., Li, M.H., Hao, K., Flow-injection analysis of glucose without enzyme based on electrocatalytic oxidation of glucose at a nickel electrode. *Talanta* 2007b, 71, 1769-1773.
Zhao, H., Zhang, Y., Yuan, Z., Study on the electrochemical behavior of dopamine with poly(sulfosalicylic acid) modified glassy carbon electrode. *Anal Chim Acta* 2001, 441, 117-122.
Zhao, H.T., Ju, H.X., Multilayer membranes for glucose biosensing via layer-by-layer assembly of multiwall carbon nanotubes and glucose oxidase. *Anal Biochem* 2006, 350, 138-144.
Zhao, W., Ali, M.M., Aguirre, S.D., Brook, M.A., Li, Y., Paper-Based Bioassays Using Gold Nanoparticle Colorimetric Probes. *Analytical Chemistry* 2008, 80, 8431-8437.
Zhou, Y.G., Yang, S., Qian, Q.Y., Xia, X.H., Gold nanoparticles integrated in a nanotube array for electrochemical detection of glucose. *Electrochem Commun* 2009, 11, 216-219.
Zhu, H.L., Wang, Y., Wang, N.Y., Li, Y., Yang, J., Hydrothermal synthesis of indium hydroxide nanocubes. *Mater Lett* 2004, 58, 2631-2634.
Zhuang, Z.J., Su, X.D., Yuan, H.Y., Sun, Q., Xiao, D., Choi, M.M.F., An improved sensitivity non-enzymatic glucose sensor based on a CuO nanowire modified Cu electrode. *Analyst* 2008, 133, 126-132.